POLITECNICO
MILANO 1863

SCUOLA DI INGEGNERIA INDUSTRIALE
E DELL'INFORMAZIONE

Design and characterization of fluorinated nanoparticles for CAR-T cell labelling and ^{19}F MRI tracking in glioblastoma therapy

TESI DI LAUREA MAGISTRALE IN
MATERIALS ENGINEERING AND NANOTECHNOLOGY -
INGEGNERIA DEI MATERIALI E DELLE NANOTECNOLOGIE

Author: **Raffaella Lobello**

Student ID: 214358
Advisor: Prof. Francesca Baldelli Bombelli
Co-advisor: Cristina Chirizzi, Serena Pellegatta
Academic Year: 2025-26

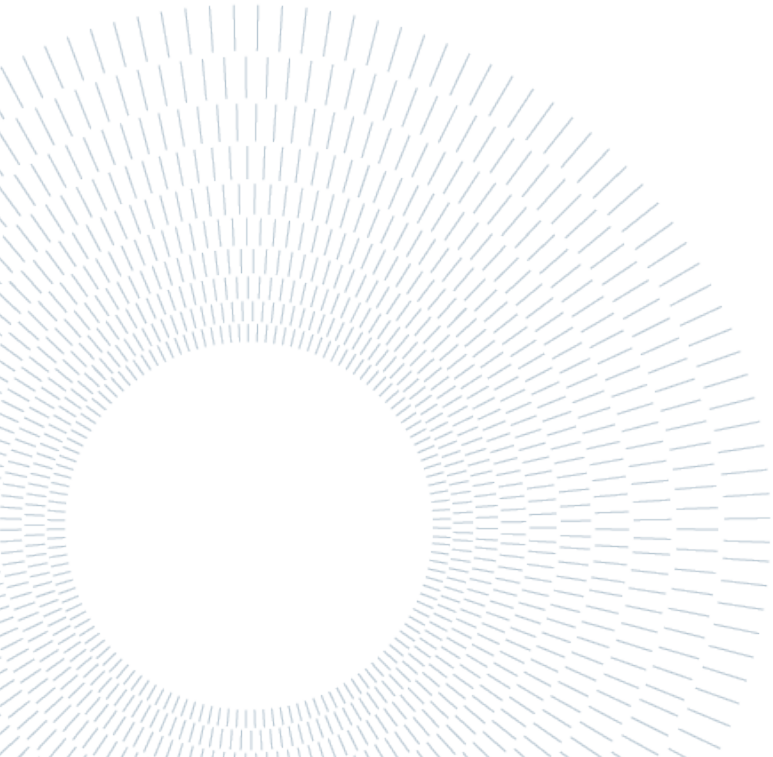

Abstract

Chimeric Antigen Receptor T-cell (CAR-T) therapy has emerged as a transformative approach in cancer immunotherapy, demonstrating remarkable efficacy in the treatment of hematological malignancies and leading to several FDA-approved therapies. However, its extension to solid tumors, particularly aggressive and immunologically complex malignancies such as glioblastoma (GB), remains a major challenge. Glioblastoma, the most common and lethal primary brain tumor in adults, is characterised by infiltrative growth, pronounced cellular heterogeneity, and a profoundly immunosuppressive tumor microenvironment, which collectively limit the efficacy of immune-based treatments. A critical barrier to the optimisation of CAR-T cell therapy for solid tumors is the inability to monitor the in vivo fate of infused therapeutic cells. Fundamental questions regarding their biodistribution, trafficking to the tumor site, persistence, and correlation with therapeutic response remain largely unanswered. This knowledge gap underscores an urgent need for non-invasive, quantitative imaging technologies capable of tracking the fate of therapeutic cells in real time.

Among available imaging modalities, fluorine-19 magnetic resonance imaging (^{19}F MRI) represents a particularly promising solution for cell tracking applications. Since the human body contains negligible amounts of endogenous fluorine, ^{19}F MRI provides background-free, "hot-spot" images that allow for direct detection and quantification of ^{19}F-labelled cells, eliminating the signal ambiguity that hampers conventional proton-based MRI. Furthermore, the ^{19}F MRI signal intensity is directly proportional to the number of fluorine atoms, enabling absolute cell quantification. Fluorinated probes characterised by magnetically equivalent ^{19}F nuclei have been developed to maximise signal sensitivity, among which PERFECTA, a recently designed fluorinated molecular probe containing 36 magnetically equivalent fluorine atoms, has shown highly promising properties for ^{19}F MRI-based cell tracking. PERFECTA can be encapsulated within nanoparticles based on the biodegradable copolymer poly(lactic-co-glycolic acid) (PLGA), widely used in biomedical applications due to its established biocompatibility and tuneable degradation kinetics.

In the present work, PERFECTA-loaded PLGA nanoparticles stabilised with sodium cholate (PERFECTA@PLGA-NaC) were developed and characterized with the aim of labelling human CAR-T cells targeting glioblastoma for potential ^{19}F MRI tracking. The NPs were prepared by emulsification solvent evaporation, and fluorescently labelled with PLGA-rhodamine B to enable their detection.

An important part of this work was dedicated to the comprehensive physicochemical characterisation of the nanoparticle formulation. Dynamic Light Scattering (DLS) analysis revealed an average hydrodynamic diameter of approximately 120 nm with a narrow size distribution (PDI < 0.2), indicating a homogeneous nanoparticle dispersion. Zeta Potential measurements confirmed a strongly negative surface charge (−43 mV), attributable to the sodium cholate stabiliser, which provides electrostatic repulsion and prevents aggregation in aqueous media. The encapsulation efficiency of the PERFECTA probe, determined by quantitative ^{19}F Nuclear Magnetic Resonance (^{19}F NMR) spectroscopy using trifluoroacetic acid as an external standard, was 41%, yielding a fluorine concentration of 1.8×10^{20} ^{19}F/mL.

The colloidal stability of the nanoparticles in biologically relevant environments was investigated by time-dependent DLS and Zeta Potential measurements in three media: unconditioned T cell culture medium, medium conditioned by CAR-T cells, and serum-free medium. In both protein-containing media, a moderate increase in hydrodynamic diameter was observed within the first hour of incubation, followed by stabilisation at later time points (6 to 24 hours), suggesting rapid adsorption of serum proteins and formation of a protein corona, with subsequent reorganisation and compaction of the adsorbed layer. Crucially, no extensive aggregation or precipitation was observed under any condition tested, confirming that the nanoparticles maintain colloidal stability throughout the labelling incubation period. The protein corona composition was analysed by SDS-PAGE gel electrophoresis, which revealed relatively stable protein profiles across time points, while Fourier Transform Infrared (FTIR) spectroscopy confirmed that the nanoparticle core structure, including the PLGA-sodium cholate interface, remained intact during protein corona formation. The combined multi-technique analysis (DLS, SDS-PAGE, and FTIR) indicated that the dynamic processes occurring during protein corona maturation primarily involve reorganisation of the adsorbed protein layer rather than chemical modification of the nanoparticle constituents.

The NP formulation was used for labelling experiments on human B7-H3-targeting CAR-T cells generated for glioblastoma immunotherapy. The labelling protocol was progressively optimised across thirteen independent experiments, evolving through three experimental formats — 24-well plates, 50 mL tubes, and T25 culture flasks — to address challenges related to cell adhesion, working volumes, and cell recovery. A central methodological challenge was the purification of labelled cells from free NPs, which was achieved through Ficoll density gradient centrifugation. While this approach successfully yielded pure samples, as confirmed by clean ^{19}F NMR spectra showing exclusively cell-associated fluorine signal, it introduced substantial cell losses with overall recovery rates of approximately 2–3%.

Despite the limited cell recovery, comprehensive characterisation of labelled CAR-T cells yielded highly encouraging results. Flow cytometry analysis demonstrated that cell viability remained consistently high following the labelling and purification

protocol (average 95.0 ± 5.9%), confirming the biocompatibility of the PERFECTA@PLGA-NaC formulation. Rhodamine B fluorescence analysis revealed remarkably efficient and homogeneous NP uptake across the cell population, with 99.1 ± 1.3% of cells showing positive fluorescence, while control cells exhibited negligible background (0.004 ± 0.009%). Quantitative ^{19}F NMR spectroscopy established an average cellular fluorine loading of 8.08 ± 5.36 × 10^{11} ^{19}F atoms per cell at standard labelling conditions (3.13 × 10^{19} ^{19}F/mL), representing a 4–8 fold improvement over previously published CAR-T cell labelling studies using perfluorocarbon-based agents. Exploratory experiments performed at an elevated nanoparticle concentration (approximately 3-fold increase) demonstrated that cellular loading could be further increased to 2.25 × 10^{13} ^{19}F/cell — a 28-fold enhancement — while maintaining high viability (97.5%), though systematic characterisation was limited by cell recovery challenges.

Finally, functional co-culture experiments with U87 glioblastoma neurospheres were performed to verify that NP-labelled CAR-T cells retained their cytotoxic activity. After 3 days of co-culture at a 1:1 effector-to-target ratio, labelled CAR-T cells achieved substantial tumour cell elimination (73% T cells, 23% tumour cells), comparable to unlabelled CAR-T controls (85% T cells, 12% tumour cells), and markedly superior to non-transduced T cells lacking the CAR construct (64% T cells, 32% tumour cells). These results demonstrate that nanoparticle labelling does not fundamentally impair the recognition, binding, and killing mechanisms essential for CAR-T cell therapeutic function, nor does it compromise antigen-driven proliferation capacity.

The results obtained in the present work demonstrate the feasibility of using PERFECTA@PLGA-NaC nanoparticles for fluorine-based labelling of CAR-T cells with high efficiency and preserved therapeutic functionality, establishing a promising platform for potential ^{19}F MRI tracking of adoptive cell therapies. However, important limitations remain, most notably the low cell recovery following Ficoll purification, which prevented the acquisition of ^{19}F MRI images in this study. Future work should prioritise improving purification efficiency through refined collection techniques or alternative separation strategies to enable recovery of cell numbers adequate for MRI-based validation. Once reliable cell recovery is achieved, phantom imaging studies will be essential to experimentally confirm the detectability predicted by the high fluorine loadings obtained. Additionally, protocol standardisation and in vivo validation in preclinical glioblastoma models will be necessary steps toward clinical translation of this cell tracking platform.

Key-words: nanoparticles; glioblastoma; CAR-T cell therapy; fluorine-19 magnetic resonance imaging.

Abstract in italiano

La terapia con cellule T dotate di recettore chimerico per l'antigene (CAR-T) ha rappresentato una svolta nell'immunoterapia oncologica, dimostrando un'efficacia straordinaria nel trattamento delle neoplasie ematologiche e portando all'approvazione di diverse terapie da parte della FDA. Tuttavia, la sua estensione ai tumori solidi, in particolare a neoplasie aggressive e immunologicamente complesse come il glioblastoma (GB), rimane una sfida considerevole. Il glioblastoma, il tumore cerebrale primario più comune e letale nell'adulto, è caratterizzato da crescita infiltrativa, marcata eterogeneità cellulare e un microambiente tumorale profondamente immunosoppressivo, che nell'insieme limitano l'efficacia dei trattamenti basati sull'immunoterapia. Un ostacolo critico all'ottimizzazione della terapia CAR-T per i tumori solidi è l'impossibilità di monitorare in vivo il destino delle cellule terapeutiche infuse. Domande fondamentali riguardanti la loro biodistribuzione, la migrazione verso il sito tumorale, la persistenza e la correlazione con la risposta terapeutica restano in larga parte senza risposta. Questa lacuna evidenzia un'urgente necessità di tecnologie di imaging non invasive e quantitative capaci di tracciare il destino delle cellule terapeutiche in tempo reale.

Tra le modalità di imaging disponibili, la risonanza magnetica al fluoro-19 (^{19}F MRI) rappresenta una soluzione particolarmente promettente per le applicazioni di tracciamento cellulare. Poiché il corpo umano contiene quantità trascurabili di fluoro endogeno, la ^{19}F MRI fornisce immagini prive di segnale di fondo (cosiddette "hot-spot"), che consentono la rilevazione diretta e la quantificazione delle cellule marcate con ^{19}F, eliminando l'ambiguità di segnale che limita la risonanza magnetica convenzionale basata su protoni. Inoltre, l'intensità del segnale ^{19}F MRI è direttamente proporzionale al numero di atomi di fluoro, permettendo una quantificazione cellulare assoluta. Sonde fluorurate caratterizzate da nuclei ^{19}F magneticamente equivalenti sono state sviluppate per massimizzare la sensibilità del segnale; tra queste, PERFECTA, una sonda molecolare fluorurata di recente concezione contenente 36 atomi di fluoro magneticamente equivalenti, ha mostrato proprietà altamente promettenti per il tracciamento cellulare tramite ^{19}F MRI. PERFECTA può essere incapsulata all'interno di nanoparticelle basate sul copolimero biodegradabile acido poli(lattico-co-glicolico) (PLGA), ampiamente utilizzato nelle applicazioni biomediche grazie alla sua comprovata biocompatibilità e alle cinetiche di degradazione modulabili.

Nel presente lavoro, nanoparticelle di PLGA caricate con PERFECTA e stabilizzate con sodio colato (PERFECTA@PLGA-NaC) sono state sviluppate e caratterizzate con l'obiettivo di marcare cellule CAR-T umane dirette contro il glioblastoma per un potenziale tracciamento tramite ^{19}F MRI. Le nanoparticelle sono state preparate mediante emulsificazione ed evaporazione del solvente e marcate fluorescentemente con PLGA-rodamina B per consentirne la rilevazione.

Una parte importante del lavoro è stata dedicata alla caratterizzazione fisico-chimica completa della formulazione nanoparticellare. L'analisi tramite Dynamic Light Scattering (DLS) ha evidenziato un diametro idrodinamico medio di circa 120 nm con una distribuzione dimensionale ristretta (PDI < 0,2), indicativa di una dispersione nanoparticellare omogenea. Le misure di Zeta Potenziale hanno confermato una carica superficiale fortemente negativa (−43 mV), attribuibile allo stabilizzante sodio colato, che garantisce repulsione elettrostatica e previene l'aggregazione in mezzo acquoso. L'efficienza di incapsulamento della sonda PERFECTA, determinata tramite spettroscopia ^{19}F NMR quantitativa utilizzando acido trifluoroacetico come standard esterno, è risultata pari al 41%, con una concentrazione di fluoro di $1,8 \times 10^{20}$ ^{19}F/mL.

La stabilità colloidale delle nanoparticelle in ambienti biologicamente rilevanti è stata studiata mediante misure DLS e di Zeta Potenziale in funzione del tempo in tre diversi mezzi: terreno di coltura per cellule T non condizionato, terreno condizionato da cellule CAR-T e terreno privo di siero. In entrambi i mezzi contenenti proteine, un moderato aumento del diametro idrodinamico è stato osservato entro la prima ora di incubazione, seguito da stabilizzazione ai tempi successivi (6 e 24 ore), suggerendo un rapido adsorbimento di proteine sieriche e la formazione di una corona proteica, con successiva riorganizzazione e compattamento dello strato adsorbito. In nessuna delle condizioni testate è stata osservata aggregazione estesa o precipitazione, confermando il mantenimento della stabilità colloidale durante l'intero periodo di incubazione. La composizione della corona proteica è stata analizzata mediante elettroforesi SDS-PAGE, che ha rivelato profili proteici relativamente stabili nel tempo, mentre la spettroscopia infrarossa a trasformata di Fourier (FTIR) ha confermato che la struttura interna delle nanoparticelle, inclusa l'interfaccia PLGA-sodio colato, si è mantenuta intatta durante la formazione della corona. L'analisi combinata multi-tecnica (DLS, SDS-PAGE e FTIR) ha indicato che i processi dinamici che avvengono durante la maturazione della corona proteica coinvolgono principalmente la riorganizzazione dello strato proteico adsorbito piuttosto che modifiche chimiche dei costituenti nanoparticellari.

La formulazione nanoparticellare è stata impiegata per esperimenti di marcatura su cellule CAR-T umane dirette contro l'antigene B7-H3, generate per l'immunoterapia del glioblastoma. Il protocollo di marcatura è stato progressivamente ottimizzato attraverso tredici esperimenti indipendenti, evolvendo in tre formati sperimentali — piastre da 24 pozzetti, tubi da 50 mL e flask T25 — per affrontare le criticità legate all'adesione cellulare, ai volumi di lavoro e al recupero cellulare. Una sfida

metodologica centrale è stata la purificazione delle cellule marcate dalle nanoparticelle libere, ottenuta mediante centrifugazione su gradiente di densità con Ficoll. Sebbene questo approccio abbia prodotto campioni puri, come confermato dagli spettri ^{19}F NMR che mostravano esclusivamente segnale di fluoro associato alle cellule, esso ha introdotto perdite cellulari sostanziali con tassi di recupero complessivi di circa il 2–3%.

Nonostante il limitato recupero cellulare, la caratterizzazione completa delle cellule CAR-T marcate ha prodotto risultati molto incoraggianti. L'analisi tramite citometria a flusso ha dimostrato che la vitalità cellulare si è mantenuta costantemente elevata dopo il protocollo di marcatura e purificazione (media 95,0 ± 5,9%), confermando la biocompatibilità della formulazione PERFECTA@PLGA-NaC. L'analisi della fluorescenza della rodamina B ha rivelato un'internalizzazione delle nanoparticelle notevolmente efficiente e omogenea nella popolazione cellulare, con il 99,1 ± 1,3% delle cellule positive alla fluorescenza, mentre le cellule di controllo hanno mostrato un fondo trascurabile (0,004 ± 0,009%). La spettroscopia ^{19}F NMR quantitativa ha stabilito un carico medio di fluoro cellulare di 8,08 ± 5,36 × 10^{11} atomi di ^{19}F per cellula alle condizioni standard di marcatura (3,13 × 10^{19} ^{19}F/mL), rappresentando un miglioramento di 4–8 volte rispetto a studi precedentemente pubblicati sulla marcatura di cellule CAR-T con agenti a base di perfluorocarburi. Esperimenti esplorativi condotti a concentrazione elevata di nanoparticelle (incremento di circa 3 volte) hanno dimostrato che il carico cellulare può essere ulteriormente aumentato fino a 2,25 × 10^{13} ^{19}F/cellula — un aumento di 28 volte — mantenendo un'elevata vitalità (97,5%), sebbene la caratterizzazione sistematica sia stata limitata dalle difficoltà di recupero cellulare.

Infine, sono stati condotti esperimenti funzionali di co-coltura con neurosfere di glioblastoma U87 per verificare che le cellule CAR-T marcate con nanoparticelle conservassero la propria attività citotossica. Dopo 3 giorni di co-coltura con rapporto effettore-bersaglio 1:1, le cellule CAR-T marcate hanno raggiunto una sostanziale eliminazione delle cellule tumorali (73% cellule T, 23% cellule tumorali), comparabile ai controlli CAR-T non marcati (85% cellule T, 12% cellule tumorali) e nettamente superiore rispetto alle cellule T non trasdotte prive del costrutto CAR (64% cellule T, 32% cellule tumorali). Questi risultati dimostrano che la marcatura con nanoparticelle non compromette fondamentalmente i meccanismi di riconoscimento, legame ed eliminazione essenziali per la funzione terapeutica delle cellule CAR-T, né la loro capacità di proliferazione antigene-dipendente.

I risultati ottenuti nel presente lavoro dimostrano la fattibilità dell'utilizzo delle nanoparticelle PERFECTA@PLGA-NaC per la marcatura a base di fluoro di cellule CAR-T con elevata efficienza e funzionalità terapeutica preservata, stabilendo una piattaforma promettente per il potenziale tracciamento delle terapie cellulari adottive tramite ^{19}F MRI. Tuttavia, permangono limitazioni importanti, in primo luogo il basso recupero cellulare dopo purificazione con Ficoll, che ha impedito l'acquisizione di

immagini ^{19}F MRI in questo studio. I lavori futuri dovranno prioritizzare il miglioramento dell'efficienza di purificazione attraverso tecniche di raccolta perfezionate o strategie di separazione alternative, per consentire il recupero di numeri cellulari adeguati alla validazione mediante MRI. Una volta ottenuto un recupero cellulare affidabile, studi di imaging su phantom saranno essenziali per confermare sperimentalmente la rilevabilità predetta dagli elevati carichi di fluoro ottenuti. Inoltre, la standardizzazione del protocollo e la validazione in vivo in modelli preclinici di glioblastoma rappresenteranno i passi necessari verso la traslazione clinica di questa piattaforma di tracciamento cellulare.

Parole chiave: nanoparticelle; glioblastoma, CAR-T terapia cellulare; risonanza magnetica al fluoro.

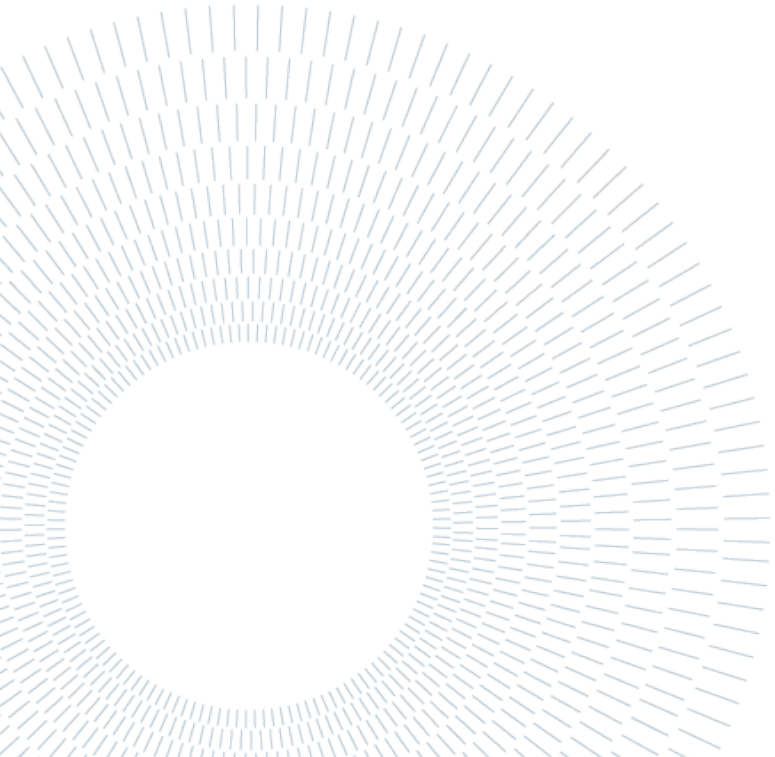

Contents

1 Introduction

Cancer remains one of the most significant global health challenges, with an estimated 19.3 million new cases and nearly 10.0 million deaths in 2020 alone [1]. Traditional therapeutic pillars—surgery, radiotherapy, and chemotherapy—have formed the cornerstone of cancer treatment for decades. While they have achieved considerable success, these modalities are often limited by non-specific toxicity, the development of drug resistance, and their inability to eradicate metastatic disease [2], [3]. In recent years, a fourth pillar of cancer therapy has emerged and revolutionized oncology: immunotherapy. This approach harnesses the patient's own immune system to recognize and eliminate malignant cells, offering the potential for durable, long-lasting responses [4].

Among the most groundbreaking immunotherapeutic strategies is Adoptive Cell Therapy (ACT), which involves the isolation, ex vivo engineering, and expansion of immune cells before re-infusing them into the patient to fight cancer [5]. Chimeric Antigen Receptor (CAR) T-cell therapy represents a paradigm shift within ACT, demonstrating unprecedented efficacy in treating hematological malignancies and leading to several FDA-approved treatments [6]. This "living drug" is engineered to express synthetic receptors that can directly recognize and target specific antigens on the surface of cancer cells, independent of the Major Histocompatibility Complex (MHC) presentation machinery [7].

Despite its remarkable success in blood cancers, the application of CAR T-cell therapy to solid tumors, particularly aggressive and immunologically complex malignancies like glioblastoma (GB), has been met with formidable challenges [8]. Glioblastoma, the most common and lethal primary brain tumor, is characterized by its infiltrative nature, cellular heterogeneity, and a profoundly immunosuppressive tumor microenvironment (TME), which collectively hinder the efficacy of immune-based treatments [9] [10].

To overcome these barriers and optimize CAR T-cell therapy for GB and other solid tumors, it is critical to understand the behavior of the infused cells in vivo. Key questions regarding their biodistribution, trafficking to the tumor site, persistence, and correlation with therapeutic response remain largely unanswered. This knowledge gap highlights an urgent unmet need for non-invasive, quantitative imaging technologies capable of tracking the fate of therapeutic cells in real-time [11].

This thesis explores the intersection of three cutting-edge fields—nanomedicine, immunotherapy, and advanced molecular imaging—to address this challenge. It focuses on the development of a novel cell tracking platform based on Fluorine-19 Magnetic Resonance Imaging (^{19}F-MRI). This modality offers a unique advantage: since the human body has a negligible amount of endogenous fluorine, ^{19}F-MRI provides background-free, "hot-spot" images that allow for the direct detection and quantification of ^{19}F-labeled cells [12].

The central hypothesis of this work is that by designing highly fluorinated, biocompatible polymeric nanoparticles, we can efficiently label CAR T-cells ex vivo without compromising their therapeutic function. These labeled cells can then be monitored non-invasively following administration in a preclinical model of glioblastoma, providing crucial insights into their in vivo behavior and therapeutic efficacy. This research aims to establish a robust imaging platform to accelerate the development and clinical translation of effective CAR T-cell therapies for solid tumors.

1.1. Nanomedicine

Nanomedicine is an interdisciplinary field that applies the principles and tools of nanotechnology—the manipulation of matter on an atomic and molecular scale, typically between 1 and 100 nanometers—to the diagnosis, treatment, and prevention of disease [13]. Over the past few decades, nanomedicine has emerged as a transformative approach in oncology, offering innovative solutions to overcome the limitations of conventional cancer therapies [14]. The primary goal of nanomedicine in cancer treatment is to enhance the therapeutic index of drugs by improving their delivery to tumor tissues while minimizing exposure to healthy organs, thereby reducing systemic toxicity [15].

Nanotechnology provides the means to engineer sophisticated drug delivery systems, often referred to as nanocarriers, that can be tailored to transport a wide range of therapeutic payloads, including small-molecule chemotherapeutics, nucleic acids, and proteins [16]. These nanocarriers vary widely in their composition and structure. Lipid-based systems such as liposomes and lipid nanoparticles were among the first nanomedicines to reach clinical approval, with Doxil—a doxorubicin-loaded liposome—receiving FDA approval in 1995. These spherical vesicles composed of lipid bilayers can encapsulate both hydrophilic and hydrophobic drugs, offering versatile delivery options. Polymer-based platforms constructed from biodegradable materials like poly(lactic-co-glycolic acid) (PLGA) offer versatile encapsulation capabilities and controlled release kinetics, as exemplified by Abraxane, an albumin-bound paclitaxel nanoparticle approved for metastatic breast cancer in 2005 [13], [17]. Inorganic nanoparticles composed of materials like silica, gold, or iron oxide serve specialized functions, with iron oxide nanoparticles finding application in products like NanoTherm for magnetic hyperthermia treatment of glioblastoma. Drug conjugate

systems, which directly link therapeutic molecules to carrier proteins or polymers, represent another major category that includes antibody-drug conjugates now widely used in targeted cancer therapy [13].

A key concept in cancer nanomedicine is targeted drug delivery, which can be achieved through passive or active mechanisms. Passive targeting has traditionally been attributed to the Enhanced Permeability and Retention (EPR) effect, whereby rapid and disorganized tumor angiogenesis creates "leaky" blood vessels with large fenestrations, and poor lymphatic drainage allows nanoparticles to extravasate from the circulation and accumulate preferentially in the tumor interstitium. However, the EPR effect has been the subject of considerable debate in recent years, with emerging evidence suggesting that its contribution to nanoparticle tumor accumulation may be more limited than previously thought, particularly in human tumors where vascular permeability is highly heterogeneous. Recent work by Chan and colleagues has proposed that nanoparticle tumor delivery may be more accurately described by an active transport mechanism rather than passive retention alone, introducing the concept of Enhanced Permeability, Transport and Retention (EPTR) or Active Transport and Retention to emphasize the role of transcellular and paracellular transport processes alongside vascular leakiness [18]. These mechanistic insights continue to evolve and inform the design of next-generation nanomedicines. Active targeting involves functionalizing the surface of nanocarriers with specific ligands such as antibodies, peptides, or aptamers that bind to receptors overexpressed on cancer cell surfaces. This strategy enhances the specificity of drug delivery and promotes cellular internalization of the nanocarrier [13].

Beyond drug delivery, nanomedicine has pioneered the development of theranostic agents [19], [20]. In their conventional application, these multifunctional nanoparticles combine therapeutic and diagnostic capabilities into a single entity, with the nanoparticles themselves serving as both the drug carrier and the imaging contrast agent [21]. This dual functionality allows for simultaneous treatment and real-time monitoring of drug distribution, target engagement, and therapeutic response within the same nanoparticle platform [20]. However, the theranostic concept can be extended beyond this conventional paradigm. In the context of cell-based therapies, nanoparticles can be employed purely as imaging agents to enable tracking of cells that themselves constitute the therapeutic intervention. This represents a conceptually distinct application where the nanoparticles do not carry therapeutic cargo but instead provide a means to visualize and monitor the biodistribution and persistence of living therapeutic cells. Previous studies have demonstrated the feasibility of labelling immune cells, including T lymphocytes, with fluorinated compounds for ^{19}F-MRI tracking [3], [22], [23]. These imaging approaches exemplify how nanomedicine tools can be adapted to support the field of cell-based cancer immunotherapy [9], [21], providing visualization capabilities that complement the therapeutic mechanism of the cells themselves rather than serving as the therapeutic agent.

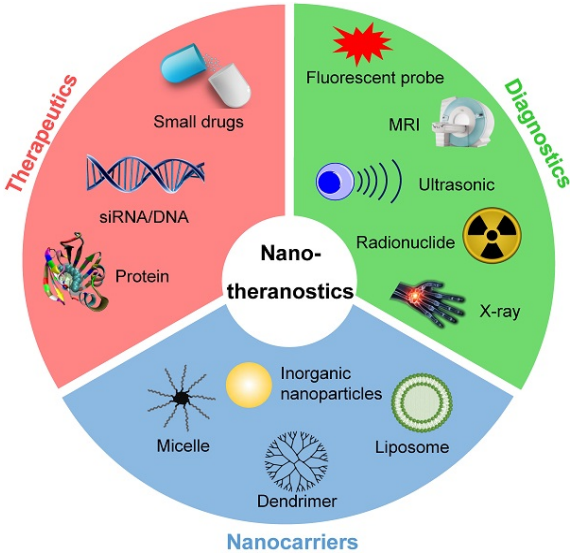

Figure 1.1 Nanotheranostics combines therapy and diagnosis in a single nanoplatform, enhancing treatment results in cancer and other diseases [19].

1.2. Glioblastoma and immunotherapy

1.2.1. Glioblastoma

Glioblastoma is the most common and most aggressive primary malignant brain tumor in adults [24]. Despite decades of research and multimodal treatment strategies, the prognosis for patients with GB remains dismal, with a median survival time of approximately 12-14 months with standard-of-care treatment, and dismal 2-year survival rates ranging from 26% to 33% [25]. Without treatment, median survival is less than three months [26].

The standard of care for newly diagnosed GB consists of maximal surgical resection of the tumor, followed by concurrent radiotherapy and chemotherapy with the alkylating agent temozolomide (TMZ) [24][26].

The standard of care for newly diagnosed GB consists of maximal surgical resection of the tumor, followed by concurrent radiotherapy and chemotherapy with the alkylating agent temozolomide [27]. However, this approach is rarely curative due to several intrinsic features of the disease that create formidable therapeutic challenges. GB is characterized by its highly infiltrative nature, where tumor cells migrate extensively into the surrounding brain parenchyma. This makes complete surgical removal virtually impossible, as ill-defined tumor borders lead to inevitable recurrence from residual microscopic disease [24]. Additionally, GB tumors are highly heterogeneous, consisting of diverse cell populations with different genetic and phenotypic characteristics. This heterogeneity contributes to therapeutic resistance, as some tumor cell clones may not respond to a given therapy [25]. Perhaps most relevant to immunotherapy approaches, GB has developed sophisticated mechanisms to evade the immune system. It creates a profoundly immunosuppressive tumor

microenvironment rich in inhibitory cells like regulatory T cells (Tregs) and myeloid-derived suppressor cells (MDSCs), and expresses checkpoint ligands such as PD-L1, which collectively dampen anti-tumor immune responses [28]. Finally, the blood-brain barrier presents an additional obstacle. While this highly selective semipermeable border is often disrupted within the core of a GB tumor, it can remain intact in infiltrative regions, limiting the delivery of systemic therapeutic agents .

The aggressive nature of GB and its resistance to conventional therapies underscore the urgent need for novel and more effective treatment strategies, making it a critical target for innovative approaches like adoptive cell therapy

1.2.2. Immune system against cancer

The immune system is a complex network of cells and molecules that has evolved to protect the host from pathogens and to eliminate damaged or abnormal cells, including cancer cells. This protective function is known as immune surveillance [29]. Both the innate and adaptive branches of the immune system are involved in recognizing and combating cancer.

The innate immune system provides the first line of defense. Its major effector cells include natural killer (NK) cells, dendritic cells (DC), macrophages, and polymorphonuclear leukocytes. These cells can directly target cancer cells. For example, NK cells can recognize and kill tumor cells that have downregulated MHC class I molecules—a common immune escape mechanism—through a balance of activating and inhibitory receptors [30]. DCs are the most potent professional antigen-presenting cells (APCs) and play a crucial role in bridging the innate and adaptive immune responses by capturing tumor antigens, processing them, and presenting them to T cells [30].

The adaptive immune system, primarily mediated by T and B lymphocytes, provides a highly specific and long-lasting anti-tumor response. Cytotoxic T lymphocytes ($CD8^+$ T cells) are central to this response. They recognize specific tumor-associated antigens (TAAs) presented as peptides on MHC class I molecules on the surface of cancer cells and directly kill these target cells [31]. $CD4^+$ helper T cells play a supporting role by producing cytokines that orchestrate the overall immune response and activate other immune cells.

The interaction between cancer and the immune system is a dynamic process termed "cancer immunoediting", which consists of three phases: elimination, equilibrium, and escape [32].

1. Elimination: In this phase, the immune system successfully recognizes and destroys developing tumor cells, effectively acting as a surveillance mechanism.

2. Equilibrium: If some cancer cells survive the elimination phase, they may enter a state of equilibrium where the immune system controls tumor growth but does not

completely eradicate it. This phase can last for many years and represents a period of immunologic sculpting of the tumor.

3. Escape: Eventually, tumor cell variants may emerge that are no longer recognized by the immune system or can suppress the immune response. These cells can then grow uncontrollably, leading to clinically apparent cancer.

Understanding these immune evasion mechanisms has paved the way for the development of modern immunotherapies designed to overcome them and re-engage the immune system's power to fight cancer.

1.2.3. Advances in immunotherapy

Building on the foundational understanding of tumor immunology, the last two decades have witnessed a surge in the development of novel immunotherapeutic strategies that aim to harness and amplify the body's immune response against cancer. One of the most significant breakthroughs has been the advent of immune checkpoint inhibitors. These are monoclonal antibodies that block inhibitory receptors on T cells, such as PD-1 or CTLA-4, or their ligands on tumor cells, thereby releasing the "brakes" on the immune system and allowing T cells to mount a more vigorous anti-tumor response [33]. Drugs such as ipilimumab (anti-CTLA-4) and nivolumab or pembrolizumab (anti-PD-1) have achieved remarkable clinical success in melanoma, non-small cell lung cancer, and other malignancies, leading to durable responses in a subset of patients.

Another major advance is Adoptive Cell Therapy (ACT), a strategy that involves the infusion of large numbers of tumor-reactive immune cells into patients. The first demonstrations of clinical efficacy came from studies using tumor-infiltrating lymphocytes (TILs) in melanoma [34], [35]. This approach achieved a significant regulatory milestone in February 2024, when Lifileucel became the first TIL-based product to receive FDA accelerated approval for advanced melanoma, representing the first cellular therapy approved for any solid tumor [36]. Building on this success, TIL therapy is now being explored for other solid tumors, including glioblastoma. Recent work has demonstrated the feasibility of isolating and expanding tumor-reactive TILs from glioblastoma surgical specimens, with enrichment for CD137-expressing T cells yielding functional polyclonal populations capable of specific anti-tumor activity both in vitro and in vivo [37].

Subsequent advances in molecular and cellular biology led to the development of engineered T-cell therapies. This involves genetically modifying T cells to enhance their ability to recognize and kill cancer cells. Two major categories have emerged: T-Cell Receptor (TCR) engineered T cells, which are modified to express a TCR with high affinity for a specific tumor antigen peptide presented by MHC molecules, allowing them to recognize intracellular tumor antigens; and Chimeric Antigen Receptor (CAR) T cells, which represent a significant evolution in ACT [7]. CAR-T cells overcome MHC

restriction by using an antibody-derived recognition domain fused to T-cell signaling machinery, enabling them to recognize surface antigens directly without the need for antigen processing and MHC presentation [38], [39]. CAR-T cell therapy has demonstrated sustained and transformative clinical efficacy in hematologic malignancies, leading to the regulatory approval of multiple CD19- and BCMA-directed products for relapsed or refractory B-cell lymphomas, acute lymphoblastic leukemia, mantle cell lymphoma, and multiple myeloma [40] .

1.3. Adoptive cell therapy

Adoptive Cell Therapy (ACT) is a form of immunotherapy where immune cells, most commonly T lymphocytes, are collected, genetically modified or selected for tumor reactivity, expanded ex vivo, and reinfused into the patient to mediate anti-tumor responses. The earliest forms of ACT involved the isolation and expansion of tumor-infiltrating lymphocytes (TILs) from resected tumors. TILs are naturally occurring T cells that have already infiltrated the tumor microenvironment and exhibit some degree of tumor recognition. When isolated, expanded in large numbers ex vivo, and reinfused into the patient, TILs have demonstrated clinical efficacy, particularly in melanoma [34], [35].

Subsequent advances in molecular and cellular biology led to the development of engineered T-cell therapies, where T cells are genetically modified to enhance their ability to recognize and kill cancer cells. This represents a significant evolution from naturally occurring TILs to purposefully designed cellular therapeutics with defined tumor specificity.

1.3.1. T Lymphocytes

T lymphocytes, or T cells, are the cornerstone of ACT. These cells are central players in the adaptive immune system, responsible for cell-mediated immunity and the recognition and elimination of infected or malignant cells. T cells develop in the thymus and express a unique T-Cell Receptor (TCR) on their surface that determines their antigen specificity.

There are two major subsets of T cells distinguished by the expression of co-receptor molecules:

CD8+ T cells (Cytotoxic T Lymphocytes, CTLs): These are the primary effector cells that directly kill target cells. They recognize antigenic peptides presented by Major Histocompatibility Complex (MHC) class I molecules, which are cell surface proteins expressed on virtually all nucleated cells. MHC class I molecules display fragments of intracellular proteins, allowing CD8+ T cells to monitor the internal state of cells and detect infections or malignant transformation. Upon recognition of their cognate antigen, CD8+ T cells release cytotoxic granules containing perforin and granzymes,

which induce apoptosis in the target cell. They also secrete inflammatory cytokines such as IFNγ and TNFα that contribute to the anti-tumor immune response.[31].

CD4+ T cells (Helper T cells): These cells orchestrate the overall immune response. They recognize antigens presented by MHC class II molecules on professional antigen-presenting cells such as dendritic cells, macrophages, and B cells. CD4+ T cells provide help to CD8+ T cells through cytokine secretion and co-stimulatory signals, enhancing their activation, proliferation, and cytotoxic function. Different subsets of CD4+ T cells (Th1, Th2, Th17, Tregs) produce distinct cytokine profiles and serve different immunological functions [38].

The specificity of a T cell is determined by its unique T-Cell Receptor (TCR). The TCR is a heterodimeric protein complex composed of alpha and beta chains (or gamma and delta chains in a minor subset), each containing variable regions that recognize specific peptide-MHC complexes. TCR diversity is generated through V(D)J recombination during T-cell development, creating a vast repertoire capable of recognizing virtually any foreign or aberrant antigen. However, natural TCRs are restricted to recognizing antigens presented by MHC molecules, which tumor cells can evade by downregulating MHC expression—a major mechanism of immune escape [39].

For ACT purposes, T cells can be isolated from peripheral blood through leukapheresis, a procedure that separates white blood cells from other blood components. These T cells can then be activated ex vivo using anti-CD3 antibodies (which engage the TCR complex) and co-stimulatory signals, expanded to large numbers, and either selected for tumor reactivity (as in TIL therapy) or genetically engineered to express tumor-targeting receptors (as in CAR-T or TCR-T therapy).

1.3.2. CAR-T cells engineering

CAR T-cell therapy involves genetically engineering a patient's T cells to express a Chimeric Antigen Receptor (CAR). A CAR is a synthetic receptor that combines the antigen-recognition domain of an antibody with the signaling machinery of a T cell, thereby conferring new antigen specificity to the T cell in an MHC-independent manner. This design overcomes one of the major limitations of natural T-cell immunity: the requirement for antigen presentation by MHC molecules, which tumors frequently downregulate as an immune evasion mechanism [7], [38]. By using an antibody-derived single-chain variable fragment (scFv) to recognize surface antigens directly, CAR-T cells can kill tumor cells independently of MHC expression, making them effective even against tumors that have lost MHC as an escape mechanism.

1.3.2.1. CAR Structure and generations

A CAR construct typically consists of four main domains:

1. Extracellular Antigen-Binding Domain: This is usually a single-chain variable fragment (scFv) derived from a monoclonal antibody, which recognizes a specific

antigen on the surface of tumor cells (e.g., CD19 on B-cell malignancies) [41]. This antibody-based recognition allows CAR T cells to bind to native surface antigens, bypassing the need for MHC presentation.

2. Hinge Region: A flexible spacer that connects the scFv to the transmembrane domain, providing structural stability and influencing the CAR's ability to engage its target.

3. Transmembrane Domain: This anchors the CAR to the T-cell membrane.

4. Intracellular Signaling Domains: These domains transmit the activation signals into the T cell upon antigen binding.

The evolution of this domain defines the different "generations" of CARs [6]:

First-Generation: Contained only the CD3ζ signaling domain from the TCR complex. These cells showed limited anti-tumor activity and poor persistence in vivo.

Second-Generation: Incorporated one co-stimulatory domain (e.g., CD28 or 4-1BB) in tandem with CD3ζ. This addition dramatically improved T-cell proliferation, cytokine secretion, and persistence, leading to the clinical breakthroughs in leukemia and lymphoma.

Third-Generation: Include two co-stimulatory domains (e.g., both CD28 and 4-1BB).

Fourth-Generation (TRUCKs): "T cells redirected for universal cytokine-mediated killing" are based on second-generation CARs and are further engineered to secrete payloads like proinflammatory cytokines (e.g., IL-12) to remodel the TME and recruit other immune cells.

Fifth-Generation: Incorporate elements like cytokine receptor domains (e.g., IL-2R beta chain) to mimic cytokine signaling and further enhance T-cell survival and proliferation.

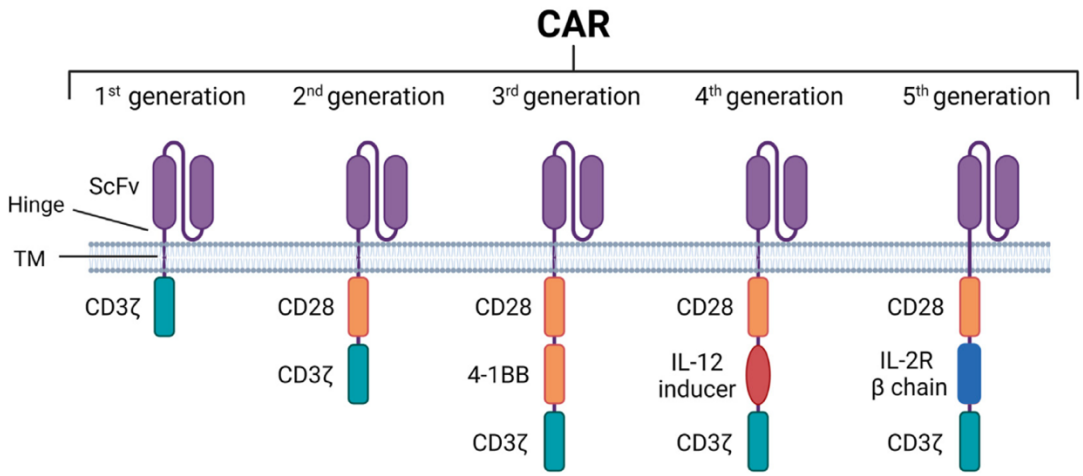

Figure 1.2 Overview of CAR generation [41]

1.3.2.2. Target antigens in glioblastoma: focus on B7-H3

The success of CAR-T cell therapy depends critically on the selection of an appropriate target antigen. The ideal target should be highly and uniformly expressed on tumor cells while having minimal or no expression on normal tissues to avoid on-target, off-tumor toxicity. Additionally, the antigen should be accessible on the cell surface and its expression should be stable rather than subject to downregulation or antigen escape.

In the specific case of GB, one of the most promising target antigens is B7-H3 (CD276), a member of the B7 family of immune checkpoint proteins. B7-H3 is a membrane-associated protein that is overexpressed in more than 70% of GB cases, as well as in several other solid tumors including neuroblastoma, ovarian cancer, pancreatic cancer, and melanoma, while showing minimal or no expression in normal tissues [42], [43]. This expression pattern makes B7-H3 an attractive target for CAR-T cell therapy, as it provides a wide therapeutic window with reduced risk of off-tumor toxicity.

The biological role of B7-H3 in cancer is complex and context-dependent. While it was initially characterized as an immune checkpoint molecule with potential co-stimulatory or co-inhibitory functions depending on the cellular context, its role in GB appears to be primarily tumor-promoting rather than immunoregulatory. B7-H3 expression in glioblastoma has been associated with increased tumor invasiveness, higher tumor grade, and poorer patient prognosis [44], [45]. The protein exists in two isoforms—a two-immunoglobulin (2Ig) form and a four-immunoglobulin (4Ig) form—with the 4Ig isoform being predominantly expressed in human glioblastomas [44]. Recent studies have demonstrated that B7-H3 serves as a reliable diagnostic biomarker for differentiating between high-grade and low-grade gliomas, with significantly higher expression observed in GB compared to lower-grade tumors [45].

In preclinical studies, B7-H3-targeted CAR-T cells have demonstrated potent anti-tumor activity against glioblastoma neurospheres and patient-derived xenografts both in vitro and in vivo [43]. These CAR-T cells showed specific cytotoxic activity against B7-H3-expressing tumor cells while sparing B7-H3-negative normal cells, achieved sustained proliferation upon antigen encounter, and demonstrated tumor control in orthotopic GB models without evidence of off-tumor toxicity [43]. Importantly, B7-H3 CAR-T cells maintained their cytotoxic function even against GB stem-like cells, which are thought to contribute to tumor recurrence and therapeutic resistance.

The work presented in this thesis utilizes CAR-T cells engineered to target B7-H3, making the development of effective tracking methods for these cells particularly relevant to advancing B7-H3-directed immunotherapy for GB.

1.3.2.3. Manufacturing and gene delivery

The conventional ex vivo manufacturing process for autologous CAR T cells is a complex, multi-step procedure [41]:

1. Leukapheresis: T cells are isolated from the patient's blood.
2. T-cell Activation and Transduction: The isolated T cells are activated in vitro using anti-CD3/anti-CD28 antibodies or magnetic beads coated with these antibodies. Activation is necessary to render T cells permissive to transduction and to initiate proliferation. The activated T cells are then genetically modified to express the CAR, most commonly achieved using viral vectors. Gamma-retroviral vectors integrate into the genome of dividing cells and have been used successfully in approved CAR-T products. Lentiviral vectors can transduce both dividing and non-dividing cells, offering greater flexibility and potentially safer integration profiles. Non-viral methods such as electroporation of CAR-encoding mRNA (providing transient CAR expression) or transposon systems (such as Sleeping Beauty or PiggyBac) are also being explored as potentially safer and more cost-effective alternatives [41].
3. Expansion: The engineered CAR-T cells are expanded in culture to achieve a therapeutic dose, typically ranging from hundreds of millions to billions of cells depending on the indication and product specification. This process requires careful monitoring of cell growth kinetics, phenotype (including CD4+/CD8+ ratios and memory/effector differentiation status), and function (including CAR expression levels and cytotoxic capacity). The expansion phase typically lasts 7-14 days and employs media supplemented with cytokines such as IL-2, IL-7, and/or IL-15 to support T-cell proliferation and maintain appropriate differentiation states.
4. Quality control and cryopreservation: The final CAR-T cell product undergoes rigorous quality control testing to ensure identity (correct CAR expression), purity (percentage of CAR+ cells and absence of contamination), potency (cytotoxic function against target cells), and safety (absence of replication-competent virus, endotoxin, and mycoplasma). Products meeting release criteria are formulated in cryopreservation medium, frozen in controlled-rate freezers, and stored in vapor-phase liquid nitrogen for transport to the treatment center.
5. Lymphodepletion: Prior to infusion, the patient often receives a conditioning regimen of chemotherapy to deplete endogenous lymphocytes. The most common regimen combines fludarabine and cyclophosphamide administered over 3-5 days. This lymphodepletion creates a favorable environment for CAR-T cell expansion by reducing competition for homeostatic cytokines (particularly IL-7 and IL-15), eliminating regulatory T cells that might suppress

CAR-T cell function, and potentially depleting immunosuppressive myeloid cells.

6. Infusion: The final CAR T-cell product is infused back into the patient.

This intricate and lengthy process is a major limitation, being time-consuming and costly, which has spurred research into alternative "off-the-shelf" allogeneic CAR T cells from healthy donors and in vivo CAR T generation strategies where T cells are engineered directly within the patient's body.

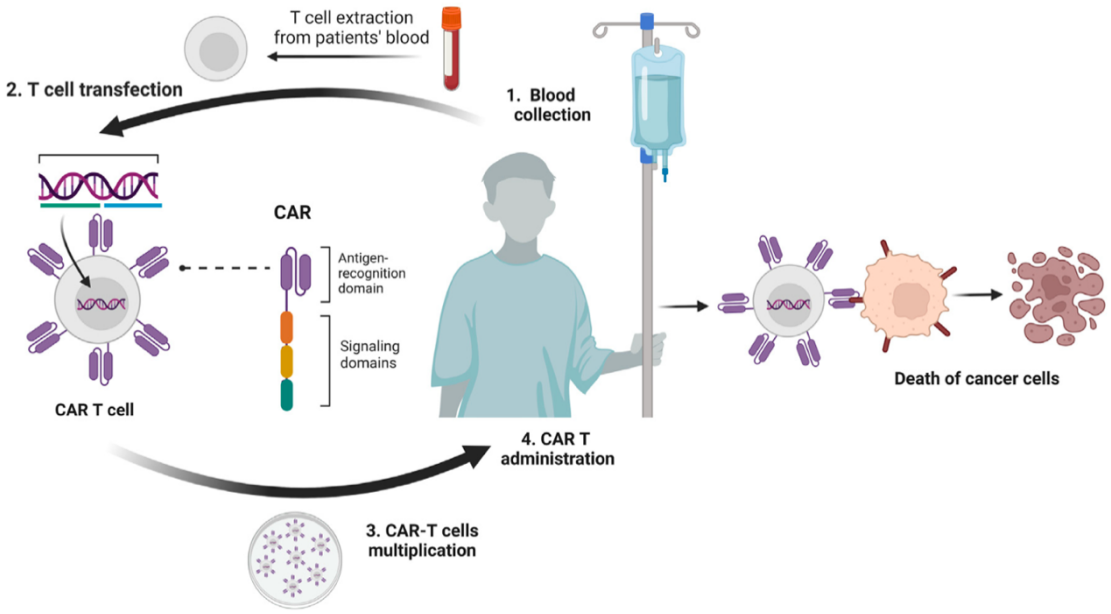

Figure 1.3 Process of ex-vivo CAR-T therapies [42].

1.3.3. Importance of monitoring CAR-T cells

The clinical success of CAR T-cell therapy has been accompanied by significant and sometimes life-threatening toxicities, such as Cytokine Release Syndrome and Immune Effector Cell-Associated Neurotoxicity Syndrome. Furthermore, the translation of this therapy to solid tumors like glioblastoma has been hampered by challenges including poor T-cell trafficking, limited persistence in the immunosuppressive TME, and antigen escape [31]. These complexities underscore the critical need for non-invasive methods able to determine efficacy and toxicity of the injected CAR-T cells, providing more comprehensive information about cell viability, fate, persistence, and treatment evaluation. This will provide an early indicator of therapeutic efficacy, supporting the advancement of personalized medicine and improving patient care.

In vivo cell tracking is essential for several key reasons:

• Assessing Biodistribution and Tumor Homing: A fundamental requirement for efficacy is that CAR T cells must traffic from the bloodstream, extravasate into the tumor tissue, and engage with cancer cells. Imaging techniques, such as Magnetic

Resonance Imaging (MRI), can confirm whether the administered cells reach their intended target and in what quantity [9].

• Predicting Therapeutic Response: Studies have begun to show a direct correlation between the magnitude and spatial distribution of T-cell infiltration into a tumor and the subsequent therapeutic outcome. Non-invasive imaging of T-cell influx could serve as an early biomarker to predict whether a patient will respond to treatment, potentially allowing for timely intervention in non-responders [46].

• Understanding Treatment Failure: In cases of relapse, imaging can help determine the cause. For instance, it can differentiate between a failure of T cells to reach or persist in the tumor versus antigen loss by the tumor cells (an immune escape mechanism).

• Improving Safety and Dosing: By visualizing the accumulation of CAR T cells in both on-target tumor sites and off-target healthy organs, researchers can better understand the mechanisms of toxicity and develop strategies to mitigate them. It could also help optimize dosing to achieve a therapeutic effect while minimizing adverse events.

• Accelerating Clinical Development: A reliable cell tracking platform can streamline the preclinical and clinical evaluation of new CAR T-cell therapies, providing rapid feedback on cell behavior and enabling a more rational design of next-generation therapies [9].

• Regulatory Requirement: As cell therapies become more widespread, regulatory agencies like the FDA are considering whether to require cell tracking data to definitively establish the anatomical fate and persistence of the therapeutic cells as part of the process for establishing treatment efficacy.

1.4. Imaging strategies for cell tracking

To address the need for monitoring adoptive cell therapies, a variety of non-invasive imaging modalities have been developed and applied in both preclinical and clinical settings. These strategies can be broadly divided into direct and indirect labeling methods [47].

Direct labeling involves ex vivo incubation of cells with an imaging agent (e.g., a radioactive tracer, a contrast agent, or a fluorescent probe) that is internalized inside the cytoplasm. The labeled cells are then infused and tracked. This method is straightforward but is limited by signal dilution upon cell division and potential signal loss due to probe efflux or cell death [47].

Indirect labeling relies on genetically engineering the therapeutic cells to express a reporter gene (e.g., an enzyme or a transporter). An imaging probe specific for the reporter protein is then administered systemically, accumulating only in the engineered cells. This approach provides a signal that is specific to viable cells and can

track cell proliferation, but it requires genetic modification, which adds complexity and regulatory hurdles [47].

1.4.1. Non-invasive imaging

Several imaging modalities are available for cell tracking, each with its own set of advantages and limitations.

Optical Imaging (OI): This category includes fluorescence imaging (FLI) and bioluminescence imaging (BLI). OI is characterized by high sensitivity, relatively low cost, and ease of use, making it a workhorse for preclinical research [9]. BLI, which relies on the luciferase-luciferin reaction, provides an excellent signal-to-background ratio. However, the applicability of OI in humans is severely limited by the poor penetration depth of light through tissue, restricting its use to superficial applications [47].

Nuclear Medicine (PET and SPECT): Positron Emission Tomography (PET) and Single-Photon Emission Computed Tomography (SPECT) are highly sensitive, quantitative techniques that are readily translatable to the clinic. Direct cell labeling can be performed with agents like ^{111}In-oxine, while indirect labeling often uses reporter genes such as Herpes Simplex Virus thymidine kinase type-1 (HSV1-tk) or the sodium-iodide symporter (NIS) [47]. PET imaging of cytotoxic T cells co-expressing a PET reporter gene has been successfully demonstrated in glioma patients [48]. The primary drawbacks are the use of ionizing radiation and relatively low spatial resolution.

Magnetic Resonance Imaging (MRI): MRI offers excellent spatial resolution without the use of ionizing radiation, providing detailed anatomical context [3], [22]. Conventional cell tracking with MRI has relied on proton (^{1}H) imaging using superparamagnetic iron oxide (SPIO) nanoparticles as a contrast agent. However, SPIOs create a negative (dark) contrast that can be difficult to distinguish from other signal voids (e.g., hemorrhages, air), and direct quantification of cell numbers is challenging [11]. These limitations have motivated the development of ^{19}F-MRI as a superior alternative for quantitative cell tracking.

1.4.2. ^{19}F Magnetic Resonance Imaging (MRI)

Fluorine-19 (^{19}F) MRI is a specialized MRI technique that detects the signal from fluorine nuclei instead of protons. It has emerged as a powerful platform for quantitative molecular imaging and cell tracking due to the unique properties of the ^{19}F isotope [12].

• Favorable NMR Properties: The ^{19}F nucleus has a spin of ½, 100% natural abundance, and a gyromagnetic ratio very close to that of ^{1}H, resulting in a high relative sensitivity of 83% compared to protons [9], [49].

• Background-Free Detection: The most significant advantage of ^{19}F-MRI is the virtual absence of endogenous fluorine in biological tissues. This means that any detected ^{19}F signal is exclusively from the exogenously administered fluorinated agent. This results in "hot-spot" images with an inherently high signal-to-background ratio, where the location and intensity of the signal directly correspond to the location and quantity of the labeled cells [50].

• Quantitative Capability: The intensity of the ^{19}F-MRI signal is directly proportional to the number of fluorine spins in a given voxel. By imaging a reference tube with a known concentration of ^{19}F alongside the subject, the number of labeled cells in a region of interest can be accurately quantified [9].

The agents used for ^{19}F-MRI are typically highly fluorinated molecules, most commonly liquid perfluorocarbons (PFCs) such as perfluoro-15-crown-5-ether (PFCE) or perfluorooctyl bromide (PFOB) [12]. These hydrophobic compounds are formulated into stable emulsions (typically 100-200 nm in diameter) for administration and cellular uptake.

The primary challenge for ^{19}F-MRI is its relatively low sensitivity compared to nuclear medicine techniques. A large number of ^{19}F atoms (~10^{10}–10^{12} spins per cell) must be loaded into each cell to generate a detectable signal in vivo [51]. This has driven extensive research into developing new fluorinated probes and delivery vehicles with higher fluorine content and improved cell labeling efficiency to overcome this sensitivity limitation [52].

1.4.3. PERFECTA: a new fluorinated molecular probe

To address the sensitivity challenge of ^{19}F-MRI, a superfluorinated molecular probe named PERFECTA was developed [53]. PERFECTA was designed specifically to maximize the ^{19}F signal from a single molecule. Its key features include:

• High and Equivalent Fluorine Content: The PERFECTA molecule contains 36 chemically and magnetically equivalent fluorine atoms. This equivalence means that all 36 fluorine nuclei resonate at the same frequency, producing a single, intense, sharp resonance peak in the ^{19}F-NMR spectrum. This concentrates the entire signal into one peak, dramatically increasing the signal-to-noise ratio (SNR) compared to PFCs which often have multiple peaks [53].

• Simple Synthesis and Formulation: PERFECTA can be synthesized in a straightforward, one-step reaction and can be formulated into stable aqueous nanoemulsions using simple methods and reagents [53].

• Excellent Biocompatibility: Initial studies demonstrated that PERFECTA formulations exhibit high cellular compatibility, with low cytotoxicity even after prolonged incubation with cells like dendritic cells (DCs) [53].

• High Cellular Uptake: A short incubation time (2 hours) was sufficient to achieve a high cellular uptake of up to 1.92×10^{13} ^{19}F atoms per DC, enabling an in vitro detection limit of less than 10,000 cells per voxel [53].

• Multiscale Imaging Potential: In addition to its excellent ^{19}F-MRI properties, PERFECTA has a characteristic C-F Raman vibrational mode that falls within a silent region of the cellular Raman spectrum. This allows it to be used as a specific fingerprint for Raman microscopy, enabling multiscale imaging from the whole-body level (^{19}F-MRI) down to the single-cell or tissue level (Raman) [52], [54].

These properties make PERFECTA a highly promising candidate for developing next-generation ^{19}F-MRI probes with enhanced sensitivity for demanding applications like tracking CAR T-cells.

1.4.4. Polymeric nanoparticles for imaging

Polymeric nanoparticles (NPs) are solid colloidal particles ranging in size from 10 to few hundreds nm, in which a therapeutic or diagnostic agent can be dissolved, entrapped, encapsulated, or attached to a polymer matrix. They have become a cornerstone of nanomedicine due to their versatility, tunability, and potential for controlled release and targeted delivery.

For imaging applications, polymeric NPs offer several advantages:

• High Payload Capacity: They can encapsulate a large amount of imaging agent, such as the PERFECTA probe, thereby maximizing the signal per particle [12].

• Surface Functionalization: Their surface can be easily modified with targeting ligands, stealthing agents like polyethylene glycol (PEG) to prolong circulation time, or other functional moieties.

• Biocompatibility and Biodegradability: Many NPs are fabricated from polymers like poly(lactic-co-glycolic acid) (PLGA), which is FDA-approved for human use, biocompatible, and biodegrades into non-toxic products [55].

In the context of this thesis, PLGA was chosen as the optimal polymer to formulate a PERFECTA-based nano-agent. Recent work has focused on optimizing the preparation of PERFECTA-loaded PLGA NPs (PERFECTA@PLGA NPs) to achieve high colloidal stability and encapsulation efficiency [55]. Furthermore, studies have shown that the surface properties of these NPs play a crucial role in their interaction with biological systems. Upon entering a biological medium like cell culture media, NPs are immediately coated with proteins, forming a "protein corona" (PC) [56]. The composition and properties of this PC are dictated by the NP's intrinsic surface characteristics (e.g., charge, hydrophobicity) and, in turn, the PC governs the NP's biological identity, including its cellular uptake mechanism. It has been demonstrated that modulating the surface of ^{19}F-PLGA NPs can influence PC formation to enhance uptake by phagocytic cells, leading to a significantly improved ^{19}F-MRI signal and

detection sensitivity [57]. This highlights the importance of rational NP design that considers the bio-nano interface to maximize cell labeling efficiency.

2 Materials and methods

The experimental work presented in this thesis was carried out at two different research facilities. Nanoparticle synthesis, physicochemical characterization, and all analytical measurements (DLS, Zeta Potential, fluorescence spectroscopy, ^{19}F-NMR, protein corona analysis, and SDS-PAGE) were performed at the Department of Chemistry, Materials, and Chemical Engineering "Giulio Natta" of Politecnico di Milano. In vitro experiments involving CAR-T cell culture, labelling, viability assays, flow cytometry analysis, and co-culture experiments with glioblastoma cells were conducted at the Division of Brain Tumour Immunotherapy, Fondazione IRCCS Istituto Neurologico Carlo Besta (Milan, Italy), led by Dr. Serena Pellegatta

2.1. Materials

2.1.1. Solvents

Ethyl acetate (EtOAc, purity ≥ 99.5%) were purchased from Sigma Aldrich (Germany). Ultrapure type-I Milli-Q water (mQw) (18.2 mΩ/cm) was obtained by a Simplicity® water purification system (MERK, Germany).

2.1.2. Materials and reagents

2.1.2.1. Nanoparticles formulation

Poly(D,L-lactide-co-glycolide) (PLGA) Resomer® 502H (lactide:glycolide 50:50, 7000-17000 Dalton, acid terminated), sodium cholate (NaC), PLGA conjugated with Rhodamine B (lactide:glycolide 50:50, 10000-30000 Da, 3.12 μg/mg dye content), poly(lactide-co-gycolide)-fluorescein (lactide:glycolide 50:50, Mn 10000-20000) were purchased from Sigma Aldrich (Germany). PERFECTA was synthesized at the SupraBioNanoLab (SBNLab) at the Politecnico di Milano according to the protocol published by Ilaria Tirotta et al. [53]

2.1.2.2. CAR-T cell culture reagents

RPMI-1640 Medium (1X) + 2.05 mM L-Glutamine, sterile filtered, was purchased from Cytiva, HyClone™ (Logan, UT, USA). Click's Medium (Eagle's MEM, Eagle's Ham's Amino Acid BME, without sodium bicarbonate, without L-glutamine) was purchased from Sigma Aldrich (UK). Fetal bovine serum (FBS, characterized, U.S. origin) was purchased from Cytiva, HyClone™ (Logan, UT, USA). Penicillin-Streptomycin (P/S, 10,000 U/mL penicillin, 10,000 μg/mL streptomycin) and L-Glutamine (200 mM) were purchased from Gibco (Thermo Fisher Scientific, Waltham, MA, USA).

T Cell Medium (TCM) was prepared as follows: 44% Click's Medium, 44% RPMI-1640 Medium, 10% FBS, 1% Penicillin-Streptomycin, and 1% L-Glutamine, using the same reagents and suppliers as listed above. For T cell expansion, TCM was supplemented with recombinant human interleukin-15 (IL-15) and interleukin-7 (IL-7). For cellular experiments, the same formulation was used without interleukin supplementation.

Trypan Blue solution (0.4%) was purchased from Sigma Aldrich (Germany) and used for cell viability assessment by exclusion assay.

2.1.2.3. Labelling reagents

The commercial labelling buffer was purchased from Miltenyi Biotec (Bergisch Gladbach, Germany). For staining in co-culture experiments, the following antibodies were used (all from Miltenyi Biotec): anti-human CD3 (FITC), anti-human B7-H3 (PE), anti-human CSPG4 (APC). The Viobility™ 405/520 Fixable Dye was also purchased from Miltenyi Biotec. Triton™ X-100 (laboratory grade, purity ≥ 99%) was purchased from Sigma Aldrich (Germany) and used at a concentration of 2.5% in PBS.

2.1.2.4. Materials for stability tests and protein corona assessment

T cell culture medium (TCM) was prepared as described above. TCM conditioned for 6 h (at 37 °C, 5% CO_2, in contact with CAR-T cells) was collected and stored for stability and protein corona experiments.

Sucrose ($C_{12}H_{22}O_{11}$, 342.30 g/mol) was purchased from Carlo Erba Reagents (Italy).

For SDS-PAGE electrophoresis, the following reagents were used: β-mercaptoethanol, sodium dodecyl sulphate (SDS) and Trizma® Base were purchased from Merck. 2× Laemmli Sample Buffer, 40% Acrylamide/Bis (37.5:1) solution, 10× Tris/Glycine/SDS Buffer and Precision Plus Protein™ All Blue Standards were purchased from Bio-Rad® Laboratories. Acetic acid (CH_3COOH, 99–100% purity), N,N,N′,N′-tetramethylenediamine (TEMED) and ammonium persulfate (APS, for molecular biology, for electrophoresis, ≥98%) were purchased from Sigma-Aldrich. Coomassie Brilliant Blue G-250 ($C_{47}H_{48}N_3O_7S_2$–Na) was purchased from Serva. Ammonium sulfate ($(NH_4)_2SO_4$, pure) was purchased from Carlo Erba Reagents (Italy).

2.2. Nanoparticle formulation

PERFECTA@PLGA-NaC nanoparticles are formulated by the emulsification solvent evaporation method optimized by Cristina Chirizzi et al. [57]

1. The first step is the preparation of the organic and aqueous phases in separate vials. 20 mg of PERFECTA are firstly dissolved in 1.5 mL of ethyl acetate and heated up to 65° using a thermoblock. It is then added to a solution of 20 mg of PLGA dissolved in 1.5 mL of ethyl acetate.

2. 24 mg of Sodium Cholate (NaC) are dissolved in 4 mL of Milli-Q water (mQw). The aqueous phase is transferred, together with a small magnet, into a suitable rounded–bottomed flask, which is partially submerged in a crystallizer filled with water. This crystallizer is put onto a magnetic stirring - heating plate to keep the solution under magnetic stirring and at a temperature of 30°C.

3. The organic solution is rapidly mixed pipetting it up and down and added dropwise to the aqueous solution by means of a Pasteur pipette.

4. The two solutions are sonicated through a tip sonicator (Sonic Vibracell, tip diameter about 0.2 cm) at 60W for 25 seconds. The whole solution is kept under magnetic stirring at 400 rpm for 3 hours at room temperature.

5. Then, the flask is transferred to a Rotavapor to remove the excess of organic phase (by evaporation under vacuum). While the flask is put under rotation at 300 rpm and it's partially submerged in a water bath at 30 °C, its initial pressure of 250 mbar is lowered by 10 mbar step until 70 mbar pressure at which it is left for 20 minutes. It's important that the final pressure is reached gradually to avoid the formation of bubbles, which could break the NPs due to a sudden increase of the volume inside the solution.

6. After ethyl acetate evaporation, the solution is transferred into a 15 mL Falcon tube. NPs are isolated and purified by centrifugation at 10733 g for 40 minutes at 4°C.

7. The final product is resuspended in mQw.

By following this protocol, a "standard" NPs formulation is obtained: NPs are "blank" and empty. By adding specific reagents, it is possible to obtain more complex formulations. In the case of Rhodamine-functionalized NPs, 2% of the whole PLGA mass is replaced with PLGA-Rhodamine B.

2.3. Nanoparticles characterization

Once prepared, NPs used for in vitro experiments were extensively characterized to assess their physicochemical properties and suitability for biological applications. Size and size distribution (expressed as Polydispersity Index, PdI) were determined by Dynamic Light Scattering (DLS), while fluorescence spectroscopy was employed to evaluate the emission properties of fluorescently labelled formulations. Zeta Potential measurements were carried out to investigate colloidal stability. The encapsulation efficiency of the fluorinated probe PERFECTA was quantified by ^{19}F Nuclear Magnetic Resonance (^{19}F-NMR) spectroscopy. Each analysis was performed using appropriately diluted samples, following the specific requirements of the corresponding instrumentation, as detailed in the following paragraphs.

2.3.1. Dynamic Light Scattering (DLS)

Dynamic Light Scattering (DLS), also known as Photon Correlation Spectroscopy (PCS) or Quasi-Elastic Light Scattering (QELS), is a widely used technique for determining the hydrodynamic diameter and size distribution of colloidal particles in suspension [58]. It is based on the analysis of the temporal fluctuations in the intensity of scattered light that arise from the Brownian motion of particles in a fluid. Since the translational diffusion of the particles depends on their size, viscosity of the medium, and temperature, DLS provides an indirect but accurate measurement of particle size and polydispersity in the nanometer range.

When a coherent laser beam of wavelength λ is directed onto a dispersion of nanoparticles, each particle scatters the incident light in all directions. The interference of light scattered by different particles undergoing random motion leads to temporal variations in the detected intensity at a fixed angle θ. These fluctuations are statistically analysed through the intensity autocorrelation function $g^{(2)}(\tau)$, defined as

$$g^{(2)}(\tau) = \frac{\langle I(t)\, I(t+\tau)\rangle}{\langle I(t)\rangle^2}$$

where $I(t)$is the scattered light intensity at time t, and $\tau$is the delay time. The angular brackets denote a time average. According to the Siegert relation, for a system of identical and non-interacting spherical particles, the intensity autocorrelation function is related to the field autocorrelation function $g^{(1)}(\tau)$by

$$g^{(2)}(\tau) = 1 + \beta \mid g^{(1)}(\tau) \mid^2$$

where β is an instrumental coherence factor dependent on the optical alignment and detection geometry. For monodisperse particles undergoing pure Brownian motion, $g^{(1)}(\tau)$ decays exponentially according to

$$g^{(1)}(\tau) = \exp(-\Gamma\tau)$$

where Γ is the decay rate. This decay rate is directly proportional to the translational diffusion coefficient $D$of the particles and depends on the scattering vector q, expressed as

$$\Gamma = Dq^2 \text{with} q = \frac{4\pi n}{\lambda}\sin\left(\frac{\theta}{2}\right)$$

where n is the refractive index of the solvent and θ the scattering angle. The diffusion coefficient D is then related to the hydrodynamic radius $R_H$of the particles by the Stokes–Einstein equation:

$$D = \frac{k_B T}{6\pi\eta R_H}$$

where $k_B$is the Boltzmann constant, $T$the absolute temperature, and $\eta$the viscosity of the solvent. The hydrodynamic radius obtained by this relation corresponds to the radius of a hard sphere diffusing at the same rate as the particle under investigation and thus includes the particle core, the adsorbed stabiliser molecules, and the solvation layer.

For polydisperse systems, the field autocorrelation function is no longer a single exponential but a sum (or integral) of exponential decays. In this case, the apparent diffusion coefficient is determined through the cumulant analysis, where the logarithm of $g^{(1)}(\tau)$is expanded in a power series around τ = 0. The second cumulant provides an estimate of the polydispersity index (PDI), which reflects the width of the size distribution and is calculated as

$$\mathrm{PDI} = \frac{\mu_2}{\Gamma^2}$$

where $\mu_2$is the second-order moment of the decay rate distribution. According to the ISO 22412 standard, a PDI below 0.1 corresponds to highly monodisperse samples, values between 0.1 and 0.25 indicate moderate polydispersity, and values above 0.3 are associated with broad or multimodal distributions.

Prior to measurement, nanoparticle dispersions were diluted appropriately to avoid inter-particle interactions and multiple scattering effects. For the determination of the hydrodynamic diameter and polydispersity index, samples were diluted 1:100 (v/v) in Milli-Q water, ensuring an optimal count rate within the linear detection range of the instrument. For measurements in biological media, a 1:6 (v/v) dilution was used to reproduce the experimental conditions applied during cell-labelling assays. The solutions were placed in disposable low-volume polystyrene cuvettes, previously rinsed three times with filtered Milli-Q water to eliminate any dust or residues. Each measurement consisted of three consecutive runs of 5 s each, and the reported values represent the average of at least three independent acquisitions.

The raw intensity correlation data were analysed using the cumulant and non-negative least squares (NNLS) fitting algorithms provided by the instrument

software. The cumulant analysis yielded the average hydrodynamic diameter and the PDI, while the NNLS fit provided the intensity-weighted particle size distribution. Because DLS intensity is proportional to the sixth power of the particle diameter, the measured distributions are biased toward larger particles; therefore, apparent mean diameters tend to be slightly higher than those obtained by number-weighted methods. Nevertheless, DLS provides an accurate estimation of the colloidal behaviour and aggregation state of the nanoparticles in solution.

The use of DLS for nanoparticle characterisation presents several advantages. It is rapid, non-destructive, and requires minimal sample preparation, allowing in situ monitoring of stability and aggregation phenomena over time. The technique is particularly suited for nanoparticles dispersed in aqueous media with diameters ranging from 1 nm to approximately 1 μm. However, the reliability of DLS measurements can be affected by factors such as dust contamination, sample turbidity, or excessive polydispersity. To mitigate these issues, all samples and solvents were filtered through 0.22 μm pore membranes immediately before analysis.

2.3.1.1. Settings

In this work, multi-angle DLS analyses were performed using an ALV Compact Goniometer system equipped with an ALV-5000/EPP Correlator, an optical fiber detector, and an ALV/GCS-3 Compact Goniometer. The light source was a He–Ne laser (λ = 633 nm, 22 mW output power). The temperature during measurements was controlled with a Huber Mini chiller and maintained at 25°C.

NP formulations were diluted 1:100 v/v in mQ w to prevent multiple scattering while preserving colloidal integrity, and a total sample volume of 1 mL was analysed in glass cuvettes. Measurements were acquired at four scattering angles (70°, 90°, 110°, and 130°), and for each sample, three consecutive runs of 10 seconds were recorded. Data were processed using the ALV-Correlator software with the CONTIN algorithm, allowing the determination of the hydrodynamic diameter and PdI from the intensity autocorrelation function.

For stability tests, the hydrodynamic diameter and PDI of PERFECTA@PLGA–NaC nanoparticles were monitored at multiple time points (0, 1, 6, and 24 hours) during incubation in different media (unconditioned TCM, conditioned TCM, and TCM without FBS) at 37 °C. Additional measurements up to 72 hours were carried out to verify the long-term stability of the dispersions. The evolution of particle size and PDI over time was used to assess the formation of the protein corona and the influence of serum components on nanoparticle aggregation.

2.3.2. Fluorescence spectroscopy

Fluorescence spectroscopy is an optical analytical technique used to characterise materials based on their ability to absorb light at a given wavelength and subsequently re-emit part of that energy as fluorescence at a longer wavelength. The method provides valuable information on the photophysical and chemical properties of fluorescent compounds and is extensively applied to the study of nanoparticles, biomolecules, and complex systems where fluorophores are incorporated as intrinsic or extrinsic probes.

The phenomenon of fluorescence is a form of photoluminescence that occurs when a molecule absorbs photons of sufficient energy to promote an electron from its ground singlet state S_0 to an excited singlet state S_1 or higher. The excited molecule undergoes vibrational relaxation and internal conversion, dissipating part of the absorbed energy non-radiatively before returning to the ground state by emitting a photon. The energy of this emitted photon corresponds to a longer wavelength compared to the absorbed one, a characteristic shift known as the Stokes shift. The efficiency of this process is described by the fluorescence quantum yield Φ_f, defined as the ratio between the number of photons emitted and the number of photons absorbed:

$$\Phi_f = \frac{N_{\text{emitted}}}{N_{\text{absorbed}}}$$

The intensity of fluorescence emission I_f can be expressed as

$$I_f = k\,\Phi_f\,I_0\,(1 - 10^{-\varepsilon c l})$$

where k is a proportionality constant related to the geometry of the optical setup, I_0 is the incident light intensity, ε is the molar absorptivity, c is the concentration of the fluorophore, and l is the optical path length. For low concentrations, where $\varepsilon c l \ll 1$, this relationship becomes approximately linear, which is a key assumption for quantitative fluorescence analysis.

Fluorescence spectroscopy is typically performed by exciting the sample with a monochromatic beam of ultraviolet or visible light and detecting the emitted radiation at right angles to the excitation beam to minimise the contribution of scattered light. The resulting fluorescence spectrum represents the emitted light intensity as a function of wavelength, providing information on the emission maxima, intensity, and spectral shape of the fluorophore. When both the excitation and emission spectra are recorded, the full excitation–emission matrix (EEM) can be

constructed, allowing detailed investigation of overlapping signals and environmental effects on fluorescence.

In the context of NP characterisation, fluorescence spectroscopy is particularly useful for confirming the successful incorporation of fluorescent dyes or labels, evaluating their photostability, and quantifying fluorescence intensity as an indirect measure of probe loading. In this work, the technique was employed to assess the optical properties of fluorescent PLGA-based nanoparticles containing Rhodamine B (RhodB). The presence of the fluorophore allows direct visualisation of the NPs in suspension and facilitates subsequent detection by flow cytometry during cellular uptake experiments.

The recorded fluorescence spectra were analysed in terms of emission maxima and integrated intensity. The maximum fluorescence intensity, expressed in arbitrary fluorescence units (a.u.), was used to compare the emission efficiency of different nanoparticle batches. Since fluorescence emission is linearly proportional to the number of emitting species under low absorbance conditions, this intensity provides a direct measure of fluorophore content and uniformity of dye distribution within the nanoparticles. Variations in intensity between samples can therefore reflect differences in fluorophore encapsulation efficiency, aggregation state, or potential quenching phenomena due to local interactions within the polymeric matrix.

In addition to evaluating dye incorporation, fluorescence spectroscopy also provides insight into the microenvironment surrounding the fluorophore. Shifts in the emission wavelength, changes in spectral shape, or variations in fluorescence lifetime can indicate polarity effects, hydrogen bonding, or interactions between the fluorophore and polymer chains. Although lifetime measurements were not performed in this work, steady-state fluorescence spectroscopy remains a highly sensitive and informative method for detecting such effects.

Fluorescence quenching, an important phenomenon in fluorescence analysis, refers to the reduction in emission intensity caused by processes such as collisional quenching, energy transfer, or the formation of non-fluorescent complexes. The Stern–Volmer relationship describes the quantitative dependence of quenching on quencher concentration [Q]:

$$\frac{I_0}{I} = 1 + K_{SV}[Q]$$

where I_0 and I are the fluorescence intensities in the absence and presence of the quencher, respectively, and K_{SV} is the Stern–Volmer constant. Although this relation was not directly applied here, it provides the theoretical basis for interpreting

fluorescence intensity changes observed upon nanoparticle–protein interactions or aggregation events.

Overall, fluorescence spectroscopy provides a rapid, non-invasive, and highly sensitive approach for characterising fluorescent nanoparticles. The combination of excitation–emission spectra, signal intensity analysis, and controlled experimental conditions allows quantitative assessment of fluorophore incorporation and stability. In this work, fluorescence spectroscopy complemented the physico-chemical and NMR characterisation techniques by confirming the successful integration of fluorescent dyes within the PLGA–NaC matrix and by establishing a baseline for subsequent fluorescence-based detection of nanoparticles in biological assays.

2.3.2.1. Settings

For these analyses, a Jasco FP-8500 Fluorescence Spectrometer (Eason, Maryland, USA) was used. The instrument operates with a xenon (Xe) lamp as the light source and allows measurements in the 200–850 nm wavelength range for both excitation and emission spectra. Samples were placed in quartz cuvettes equipped with PTFE covers to avoid contamination and minimize photobleaching during measurements.

The measurement parameters were optimized according to the specific fluorophore employed in the nanoparticle formulation. For Rhodamine-B (RhodB)-containing samples, which exhibit an excitation peak at λ_{ex} = 546.0 nm, the emission spectrum was recorded over the 556 – 750 nm range. Both excitation and emission slit bandwidths were set at 2.5 nm, with a low sensitivity setting to reduce background noise. The data acquisition interval was set at 1 nm, and a response time of 1 second was used for each measurement point to ensure accurate signal capture.

This analysis enabled the verification of the fluorescent properties of the NPs, ensuring that the dye was successfully encapsulated and retained its optical activity after formulation.

2.3.3. ^{19}F Nuclear Magnetic Resonance (^{19}F-NMR)

Nuclear Magnetic Resonance (NMR) spectroscopy is a powerful analytical technique used to study the structure, dynamics, and quantitative composition of chemical and biological systems. In this work, ^{19}F NMR spectroscopy was employed to determine the fluorine content of the NPs and to evaluate their chemical integrity and stability in aqueous suspension.

The use of fluorine as an NMR-active nucleus offers several distinct advantages. The ^{19}F isotope possesses a nuclear spin of ½ and 100% natural abundance, resulting in a sensitivity approximately 83% that of ^{1}H and a wide chemical shift range exceeding 400 ppm. Moreover, since fluorine is virtually absent in biological tissues and media,

^{19}F NMR spectra are free from background interference, allowing selective detection of fluorinated species even at low concentrations. These properties make ^{19}F NMR particularly suitable for the study of fluorinated probes such as perfluorocarbons and for the quantitative tracking of fluorinated nanoparticles.

The physical basis of NMR relies on the interaction between nuclear magnetic moments and an external magnetic field B_0. When subjected to this field, magnetic nuclei precess around its direction at the Larmor frequency, defined as

$$\omega_0 = \gamma B_0$$

where $\omega_0$is the angular frequency and $\gamma$is the gyromagnetic ratio specific to the nucleus. For ^{19}F, $\gamma = 40.05$ MHz/T, which is close to the gyromagnetic ratio of ^{1}H (42.58 MHz/T) and enables simultaneous or dual-probe measurements. The signal intensity in NMR is proportional to the number of resonant nuclei and to their equilibrium magnetisation, which depends on the magnetic field strength and temperature according to

$$M_0 = \frac{N\gamma^2\hbar^2 B_0}{4k_B T}$$

where N is the number of spins, $\hbar$ the reduced Planck constant, $k_B$the Boltzmann constant, and T the absolute temperature. This relationship highlights how higher field strengths and lower temperatures improve the sensitivity of the measurement. The technique allows for a direct correlation between the integrated area of the fluorine resonance peak and the number of ^{19}F nuclei in the sample. The relationship between signal intensity and fluorine content is described as

$$I = kN_{19F}$$

where I is the integrated signal intensity, k is a proportionality constant determined through calibration, and N_{19F} represents the total number of fluorine nuclei in the sample.

2.3.3.1. Settings

For these analyses, 400 µL of the pure formulation was added into a coaxial NMR tube with an external reference placed inside. Each acquisition was performed with 256 averages, 24500 points per scan, centred at –73.5 ppm, and a spectral width of 10 ppm. The standard reference was prepared by dissolving trifluoroacetic acid (TFA) at

a concentration of 1.87×10^{19} ^{19}F/mL in deuterium oxide (D_2O), and 100 µL of this solution was used as the external standard. The TFA resonance, observed at –75.5 ppm, was used as an internal control for quantitative integration. All NMR spectra were recorded on a Bruker Avance III HD 400 spectrometer (Bruker BioSpin, Rheinstetten, Germany) equipped with a Bruker Automatic Sample Changer (SampleXpress). The NMR probe was maintained at 305 K throughout the experiment. All spectra were automatically phased and baseline-corrected for accurate quantitative analysis using MestReNova software.

The integration of the NP signal relative to the TFA standard allowed the calculation of the total fluorine concentration per millilitre of formulation. This parameter was subsequently used to define the fluorine concentration applied in cellular experiments, ensuring a fixed fluorine-to-volume ratio across all assays. Maintaining a constant fluorine concentration per millilitre (F/mL) is essential for reproducibility and comparability between experiments, as it ensures that each condition receives the same total fluorine dose independently of nanoparticle batch or size distribution.

Determining the fluorine content of the formulation is particularly important for evaluating the labelling potential of the nanoparticles, since non-phagocytic cells such as CAR-T lymphocytes have limited cytoplasmic volume and can internalise only a small number of particles. Accurate quantification of the fluorine signal thus enables precise control of the administered nanoparticle dose, ensuring efficient labelling while avoiding excessive exposure that might compromise cell viability or function.

2.3.4. Zeta Potential

Zeta Potential (ZP), also known as electrokinetic potential, is a key parameter for evaluating the surface charge of nanoparticles (NPs) and predicting their colloidal stability. When a particle is suspended in a liquid medium, it typically acquires a surface charge that leads to the formation of an electrical double layer (EDL) around it. This EDL consists of a Stern layer, made of tightly bound counter-ions, and a diffuse layer, which extends further into the solution and contains more loosely associated ions. The boundary between the moving particle and the surrounding liquid is known as the slipping (or shear) plane, and the electric potential at this interface is referred to as the zeta potential.

Unlike surface charge, ZP cannot be measured directly. It is calculated indirectly by determining the electrophoretic mobility of particles under an applied electric field. This mobility (μ_e) is defined as:

$$\mu_e = \frac{v}{E}$$

where v is the particle velocity and E is the electric field strength. ZP is then calculated using Henry's equation:

$$\mu_e = \frac{2\epsilon_r \epsilon_0 \zeta f(Ka)}{3\eta}$$

where ε_r and ε_0 are the relative and vacuum permittivity, respectively, η is the viscosity of the medium, and $f(Ka)$ is the Henry's function, which depends on the ionic strength of the medium.

Zeta potential is typically measured using Electrophoretic Light Scattering (ELS), where the motion of particles during electrophoresis causes a Doppler shift in scattered light, from which particle velocity can be derived.

Zeta potential values provide a useful indicator of nanoparticle colloidal stability. According to widely accepted criteria, formulations with ZP values greater than ±30 mV are considered highly stable, while those within ±10 mV are highly unstable. Although ZP is not the sole determinant of stability—since van der Waals forces and other interactions also play a role—it remains a fundamental parameter in the evaluation of nanoparticle dispersions.

2.3.4.1. Settings

In this work, ZP measurements were carried out using a Zetasizer Nano ZS (Malvern Instruments, UK), equipped with a 633 nm He–Ne laser, at a constant temperature of 25°C. Measurements were performed using folded capillary cells, which incorporate two gold-plated beryllium/copper electrodes to apply the electric field. Prior to measurement, the cells were carefully washed with mQw, and filled with the sample ensuring full immersion of the electrodes and absence of air bubbles. NPs were diluted 1:5 v/v in mQw, and each measurement was performed in triplicate to ensure reproducibility.

2.4. Nanoparticles experimental analysis

Once formulated, NPs must be rigorously evaluated to verify their suitability for biological applications. Colloidal stability, surface interactions, and chemical integrity are crucial properties that determine how NPs will behave in biological environments. These parameters not only affect the reliability of in vitro experiments, but also influence downstream aspects such as cellular uptake, biodistribution, and MRI detectability.

NP aggregation is driven by complex interactions with ions, proteins, and other components present in cell culture media, leading to unpredictable colloidal behaviour if not properly stabilized [15].

2.4.1. Stability tests

Stability tests were performed to evaluate NPs stability inside physiological media and the possible formation of a protein corona.

To simulate the environment in which NPs would be used for CAR-T cell labelling, stability tests were conducted in T Cell Medium (TCM), the same medium used for CAR-T cell incubation and manipulation.

Component	Volume percentage (%)
Click's Medium	44
RPMI-1640	44
Fetal Bovine Serum (FBS)	10
Penicillin-Streptomycin	1
L-Glutamine	1

Table 2.1 Composition of T Cell Medium.

To assess the impact of cell exposure and serum content on nanoparticle stability, three different biological conditions were evaluated:

- TCM unconditioned,
- TCM conditioned by incubation with CAR T cells for 6 hours,
- TCM without FBS.

After resuspending the NPs pellet in 1 mL of mQw, a 1:6 dilution was performed by adding the formulation to the selected culture medium in glass cuvettes for DLS. Samples were then incubated in a climate chamber set at biological conditions (37°C, 95% relative humidity) to mimic the conditions used for in vitro assays. Five different incubation timepoints were selected: T0, 1 hour, 6 hours, 24 hours. Each timepoint was processed in a separate tube to avoid perturbing the suspension during storage.

Measurements were acquired at a scattering angle of 90°, with three consecutive runs of 5 seconds each. The primary outcome of these analyses was the evaluation of size

distribution profiles and autocorrelation functions, which serve as indicators of aggregation phenomena or colloidal destabilization over time.

This protocol allowed the assessment of NP stability under cell-compatible conditions, highlighting the influence of protein content and ionic strength on colloidal integrity during incubation.

2.4.2 Protein Corona Analysis and SDS-PAGE

Upon contact with biological fluids, NPs are rapidly coated by biomolecules—primarily proteins—forming the so-called protein corona (PC). This dynamic interface alters the NPs' biological identity, affecting their colloidal behaviour, cellular interactions, and in vivo distribution. The formation of the corona is particularly relevant in serum-containing media, where the high abundance of albumin, immunoglobulins, and other proteins facilitates surface adsorption. To study the formation and composition of the PC, NPs were incubated in different biological media reflecting the experimental conditions used in cell labelling assays:

- TCM unconditioned,
- TCM conditioned by incubation with CAR T cells for 6 hours,
- Milli-Q water, used as control.

In all cases, NPs were diluted 1:6 v/v in the selected medium (600 µL total volume) to reproduce the same conditions applied during in vitro labelling. Each condition was prepared in low-binding Eppendorf tubes to minimize protein loss due to nonspecific adsorption. Incubations were carried out at 37°C and 95% humidity for defined timepoints: T0, 1 hour, 6 hours, 24 hours. After incubation, the NP–protein complexes were separated from unbound proteins through density gradient centrifugation, using a 0.7 M sucrose cushion, adapting the protocol reported by Dominic *Docter et al* [59].

Samples were carefully layered onto the cushion and centrifuged at 10733 g for 30 minutes at 4°C. This step allowed selective sedimentation of nanoparticle–protein complexes through the sucrose barrier, while leaving free proteins in the supernatant.

Following centrifugation, the NP–protein pellets were subjected to three washing cycles with mQw to remove loosely bound proteins (soft corona) and finally resuspended in 500 µL of mQw. The last supernatants and the purified NP–protein pellets were analyzed by DLS (at 90°) to verify the successful removal of unbound proteins and confirm the integrity of the purified complexes. The pellet was finally dried with an Eppendorf Concentrator 5301™system (connected with a KNF LABOPORT®vacuum pump), in which the samples were put under rotation under vacuum for 3 hours at 60°C to remove any aqueous solvent, and stored in a freezer at -20°C.

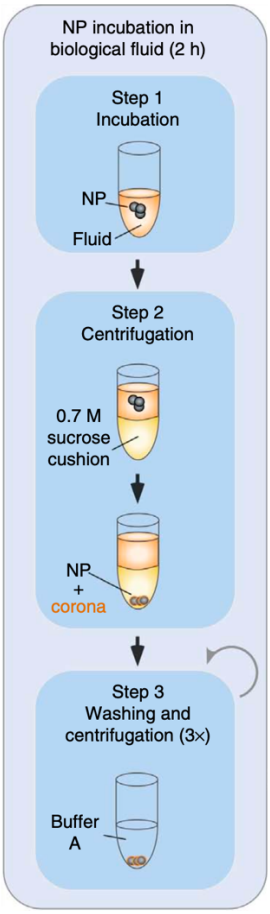

Figure 2.1 Schematic representation of the procedure adopted to isolate proteins from nanoparticles [59].

2.4.1.1. 2.4.2.1 SDS-PAGE electrophoresis

To analyse the composition of the protein corona formed around the NPs, the adsorbed proteins were extracted and characterized using SDS-PAGE (Sodium Dodecyl Sulphate – Polyacrylamide Gel Electrophoresis). This technique enables the separation of denatured proteins based on their molecular weight, allowing comparison of corona profiles across different experimental conditions.

The samples were then loaded onto pre-cast polyacrylamide gels, alongside a protein molecular weight marker for reference.

Figure 2.2 Molecular weight marker in SDS-PAGE experiments.

The SDS-PAGE protocol involves the preparation of a gel composed by two different gels: a 12% running gel and a 4% stacking gel.

	Running gel (12%)	**Stacking gel (4%)**
40% Acrilamide	1.5 mL	200 µL
Buffer 4x	1.25 mL	500 µL
mQw	2.24 mL	1.29 mL
Temed	8 µL	4 µL
APS	10 µL	8 µL

Table 2.2 Composition of running and stacking gels.

The following steps were followed:

1. Two Bio-Rad Mini-PROTEAN ® glass screens were placed in a plastic support so that they can be used as a mould for the 1 mm gel to be prepared.
2. The running gel solution was prepared and poured inside the mould without forming bubbles, then it was left to polymerize for about 30 minutes.
3. Then, the stacking gel solution was prepared and poured on the top of running gel. After the space above the running gel was filled, a 1 mm comb with 10 pockets was put on the top to grant the formation of the wells destined to the samples. The stacking gel was left to polymerize for about 10 minutes.

4. Once the gel was ready, the comb was removed. The mould was removed from the support and positioned into the Bio-Rad Mini-PROTEAN tetra electrophoretic cell. The cell is filled with a buffer obtained by diluting 1:10 v/v a 10x Tris/Glycine/SDS buffer.
5. NP–protein pellets obtained with the process described in the previous paragraph were resuspended in Laemmli buffer + 5% of β-mercaptoethanol and heated at 99 °C for 5 minutes to ensure complete denaturation and desorption of proteins.
6. The first pocket (starting from left) was loaded with 4 μL of a marker solution to provide a reference which allows a correct interpretation of the results. The other pockets were loaded with 20 μL of each sample.

Figure 2.3 SDS-PAGE electrophoretic cell with power supply.

Once the set was prepared, the electrophoresis was performed in three steps with increasing voltage:

1. 50 V for 20 minutes,
2. 100 V for 40 minutes,
3. 150 V (or 200 V to accelerate the process) for 1 hour.

At the end of the run the gels were carefully separated from the moulds. The gels were stained with a Coomassie Brilliant blue solution and destained with a solution of 7% acetic acid in water (both by stirring overnight on a shaker).

Reagents	Quantity
Ammonium sulphate	170 g
Methanol	340 mL
Phosphoric acid	30 mL
Blue Coomassie	1 g
Water	630 mL

Table 2.3 Composition of 1 L of Coomassie blue solution.

Finally, the SDS–PAGE gels were photographed and stored in a 2% acetic acid solution at 4°C.

2.4.3 Fourier Transform Infrared Spectroscopy

Fourier Transform Infrared (FTIR) spectroscopy was performed to investigate the chemical structure of nanoparticle components and to assess potential interactions between the nanoparticle surface and the adsorbed protein corona. FTIR is based on the interaction between infrared radiation and matter, where absorption occurs when the frequency of the incident radiation matches the natural vibrational frequency of a molecular bond that involves a change in dipole moment. The resulting spectrum represents the molecular fingerprint of the sample, allowing identification of characteristic vibrational modes such as stretching and bending of specific functional groups.

Compared to dispersive infrared spectroscopy, the Fourier Transform approach enables simultaneous collection of all wavelengths, improving signal-to-noise ratio and spectral resolution. In the present study, an Attenuated Total Reflectance (ATR) configuration was used. ATR-FTIR relies on the generation of an evanescent wave at the interface between an internal reflection crystal and the sample. The penetration depth of the evanescent field is typically in the micrometer range, making the technique particularly suitable for direct analysis of solid powders without extensive sample preparation.

Spectra were acquired using a Thermo Scientific Nicolet iS50 FTIR spectrometer equipped with an ATR accessory and controlled via OMNIC software. Measurements were performed in % transmittance mode with a spectral resolution of 2 cm^{-1} and a data spacing of 0.241 cm^{-1}. For each sample, 64 scans were collected, while 32 scans were used for background acquisition. Background spectra were recorded before each

sample under identical instrumental conditions. ATR correction and automatic atmospheric suppression were applied during acquisition. Interferograms were saved for each measurement and processed using OMNIC software.

2.4.1.2. Settings

All samples were analyzed in dry form. A small amount of each sample was directly deposited onto the ATR crystal to ensure adequate contact with the measurement surface. Prior to each acquisition, the crystal was carefully cleaned to avoid cross-contamination between samples.

For each measurement, a background spectrum (32 scans) was first recorded, followed by collection of the sample spectrum (64 scans) under identical instrumental settings. All measurements were performed under ambient laboratory conditions. The acquired spectra were visually inspected and exported for subsequent comparative analysis.

2.5 *In vitro* tests

2.5.2 CAR-T culture

Human CAR-T cells were generated and cultured at the Division of Brain Tumour Immunotherapy, Fondazione IRCCS Istituto Neurologico Carlo Besta (Milan, Italy), led by Dr. Serena Pellegatta. Cells were derived from peripheral blood mononuclear cells (PBMCs) isolated from healthy donor blood and subsequently transfected to express the chimeric antigen receptor (CAR) targeting B7-H3 antigen, as previously described [43].

For labelling experiments, CAR-T cells were used either freshly cultured or thawed from cryopreservation, with no significant differences observed between the two conditions in terms of viability or labelling efficiency. All experiments were performed within 7–12 days post-transfection to ensure stable CAR expression and optimal proliferative capacity.

Before labelling, cells were counted using a Trypan Blue assay and adjusted to the desired concentration in fresh T Cell Medium (without IL).

2.5.2.1 Labelling protocol with NPs

NPs labelling was performed under sterile conditions using fluorescent PERFECTA@PLGA-NaC nanoparticles. Cells were incubated with NPs at a final concentration of 3.13×10^{19} ^{19}F/mL for 6 hours at 37 °C, 5% CO_2.

Labelling experiments were initially carried out in 24-well plates (3.5×10^5 cells/well), then adapted to 50 mL Falcon® tubes (1.5×10^6 cells/tube) and finally to T25 flasks (3.3×10^6 cells/flask). In all experiments the fluorine concentration per mL of incubation medium was maintained constant at 3.13×10^{19}, while the total number of cells and ^{19}F-

to-cell ratio were adjusted as reported in Table 3. The change in format was implemented to improve cell recovery in order to have an adequate number of cells for post-labelling analysis.

Equipment	N° of cells	Final volume	^{19}F-NPs concentration of incubation (^{19}F/cell)
24-well plate	3.5×10^5	1 mL	8.9×10^{13}
50 mL tube	1.5×10^6	1 mL	2.1×10^{13}
T25 Flask	3.3×10^6	5 mL	4.7×10^{13}

Table 2.4 Summary of labelling settings.

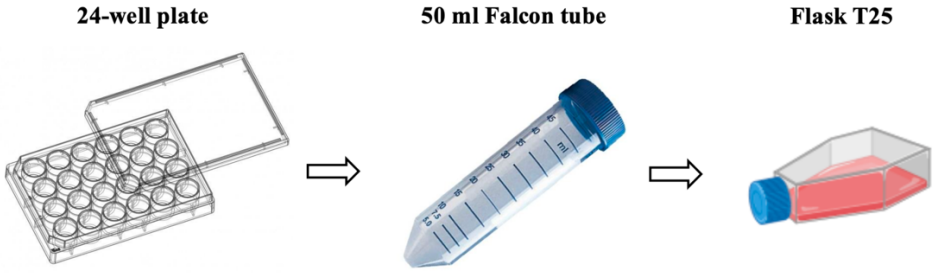

Figure 2.4 Evolution of culture formats.

Control samples (CTRL) were prepared following the same procedure, replacing NPs with an equivalent volume of Milli-Q water.

2.5.2.2 Purification of labelled CAR-T cells

After incubation, labelled cells were collected and purified to remove free NPs using a Ficoll-Paque™ density gradient centrifugation method.

The cell suspension was layered over Ficoll at a cells:Ficoll volume ratio of 3:2 and centrifuged at 2300 rpm for 20 min without brake at room temperature.

The interphase containing viable CAR-T cells was carefully collected and transferred to a new tube.

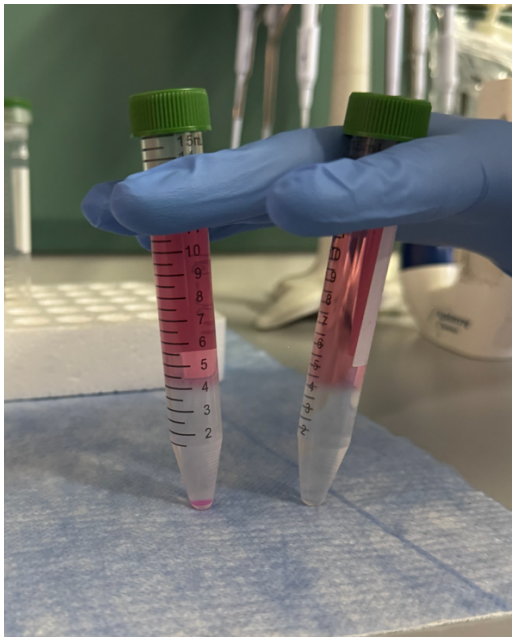

Figure 2.5 Formation of the cell layer at the Ficoll-medium interface after the first centrifugation. Left: labelled cells, showing a distinct interphase. Right: control cells, showing a clear interface.

The supernatant was further centrifuged at 1500 rpm for 5 min with brake to recover any remaining cells. Pellets from both centrifugations were combined, washed once in PBS, and finally resuspended in the appropriate medium depending on the subsequent analysis (e.g., TCM for co-culture, PBS for flow cytometry or lysis buffer for ^{19}F-NMR).

2.5.3 Cytotoxicity assay

The cytotoxic activity of labelled CAR-T cells against glioblastoma cells was evaluated through co-culture experiments with U87 neurospheres as target cells. U87 neurospheres were derived from adherent U87-MG glioblastoma cells and maintained in DMEM/F12 – GlutaMAX™ supplemented with 10% fetal bovine serum (FBS), 1% non-essential amino acids (NEAA), 1% penicillin-streptomycin, and 0.4% fungizone. Cells were cultured in low-attachment flasks at 37 °C, 5% CO_2, and high humidity to promote spheroid formation, and were passaged every 5–7 days by mechanical dissociation to maintain optimal size and viability.

On the day of the experiment, neurospheres were dissociated to single cells, counted, and seeded in 24-well plates in T cell culture medium (TCM) at a density of 1×10^5 cells/well in 1 mL. In parallel, CAR-T cells—either labelled with ^{19}F-loaded nanoparticles and unlabelled controls—were prepared according to the purification protocol described in Section 2.5.1.

Non-transduced T cells were used as negative control. The transduction efficiency was considered to calculate the number of CAR-T cells to be seeded with U87 cells in order to maintain a 1:1 effector-to-target ratio in all experimental conditions.

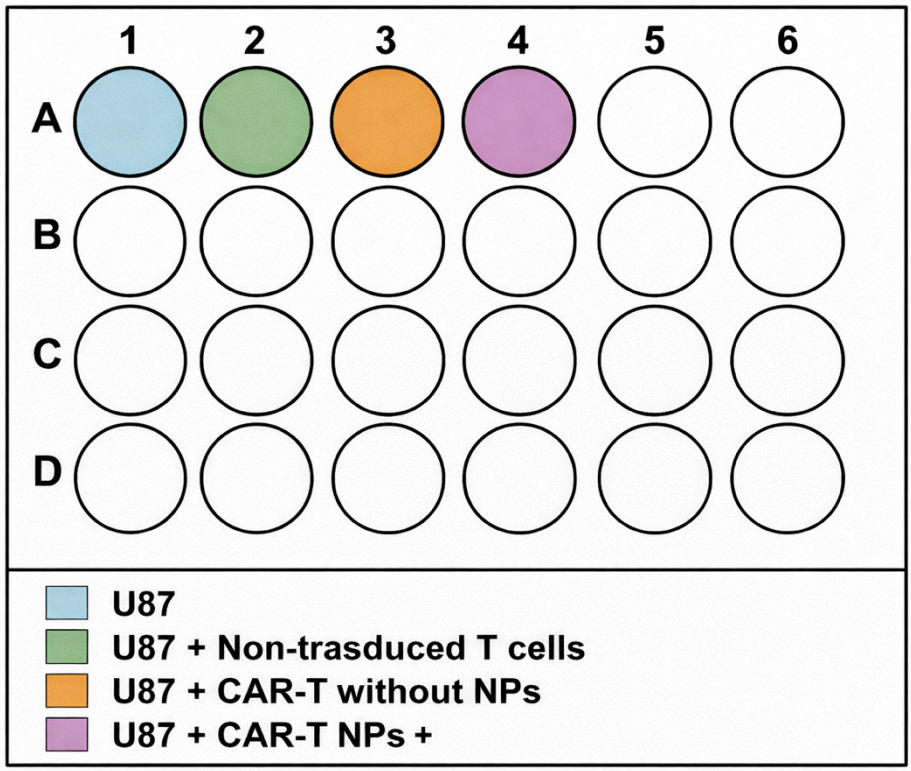

Figure 2.6 Experimental layout of the 24-well plate used for the cytotoxicity assay.

Co-cultures were maintained for 5 days at 37 °C, 5% CO_2, and monitored daily by optical microscopy to assess neurosphere morphology and evidence of target cell killing. At the end of the incubation period, cells were harvested and analysed by flow cytometry to evaluate both cytotoxicity and remaining fluorescence signal from the labelled CAR-T cells.

2.5.4 Flow Cytometry

Flow cytometry is a quantitative, high-throughput analytical technique used to measure the physical and chemical characteristics of individual cells or particles suspended in a fluid stream. It allows the simultaneous evaluation of multiple parameters at the single-cell level, including size, granularity, fluorescence intensity, and viability. In this work, flow cytometry was employed to analyse the labelling efficiency, viability, and fluorescence persistence of CAR-T cells incubated with

fluorescently labelled nanoparticles, as well as to assess cytotoxic activity in co-culture experiments.

The principle of flow cytometry is based on the passage of cells through a narrow flow chamber, where they intersect one or more laser beams. Each cell scatters light and, if fluorescent, emits photons that are collected by photodetectors through specific optical filters. The amount and direction of scattered light provide information on cell size and internal complexity, while the fluorescence intensity is proportional to the quantity of fluorophore present within or bound to the cell. The resulting signals are converted into electrical impulses, amplified, and processed to generate multiparametric datasets.

Forward scatter (FSC) correlates with the cell's cross-sectional area and is commonly used as a proxy for cell size, whereas side scatter (SSC) depends on the refractive index and internal complexity, allowing discrimination between cell subpopulations and debris. Fluorescent channels enable the detection of fluorophore-labelled molecules or particles, providing both qualitative and quantitative data on cellular uptake, surface marker expression, or viability.

For nanoparticle-based studies, flow cytometry is particularly valuable for quantifying cellular uptake of fluorescent nanoparticles, distinguishing between internalised and surface-bound particles, and evaluating possible cytotoxic effects. In the present work, Rhodamine B served as fluorescent marker incorporated into the NPs to monitor their association with CAR-T cells. The technique was used at two main stages: after the Ficoll purification step to assess cell labelling and viability, and after co-culture experiments to evaluate nanoparticle fluorescence persistence and target cell killing efficiency.

Before acquisition, cells were resuspended in phosphate-buffered saline (PBS) and stained as needed with viability dyes or specific antibodies. The exclusion of non-viable cells was performed using Viobility™ 488/520 Fixable Dye (Miltenyi Biotec), which covalently binds to cellular amines and distinguishes live from dead cells based on differential membrane integrity.

Data collection was performed in logarithmic scale for fluorescence channels and linear scale for scatter parameters. Single-stained and unstained controls were systematically used for compensation and gating calibration. The gating strategy followed a sequential approach: initial discrimination of debris and doublets by FSC/SSC profiles, exclusion of dead cells through viability staining, and identification of nanoparticle-labelled CAR-T cells based on Rhodamine B fluorescence intensity. For co-culture experiments, additional gates were applied to separate target cells (U87) from effector cells (CAR-T) based on side scatter and fluorescence profiles.

Post-acquisition analyses focused on two main outcomes. The first was the evaluation of labelling efficiency, defined as the percentage of viable CAR-T cells positive for NP fluorescence after the incubation period and Ficoll purification. This parameter reflects the fraction of cells that internalised or retained the nanoparticles. The second outcome was the assessment of cell viability, measured as the proportion of cells negative for the Viobility dye. In co-culture experiments, flow cytometry was used to quantify the extent of target cell killing and to determine whether labelled CAR-T cells maintained detectable fluorescence after interaction with tumour cells, thus confirming nanoparticle stability and persistence in a biologically active environment.

Flow cytometry provides several advantages in this context. It enables rapid acquisition of thousands of single-cell events, offers high reproducibility, and allows direct comparison between multiple samples. Moreover, its multiparametric capability makes it ideal for correlating nanoparticle fluorescence with other cellular markers, such as activation or exhaustion signals, in future investigations.

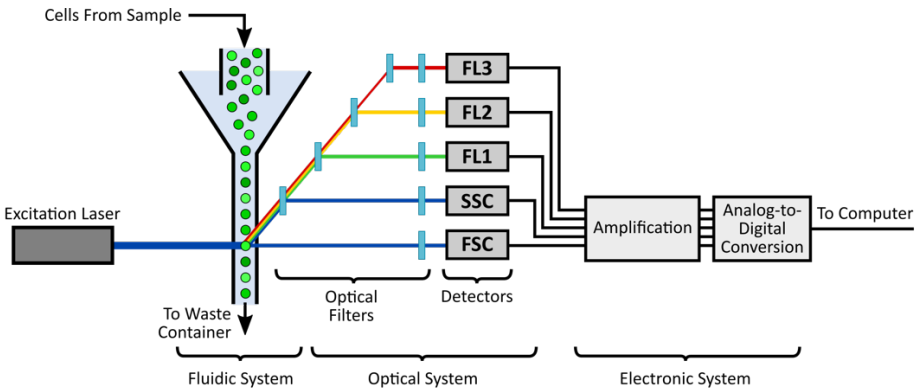

Figure 2.7 Schematic of a common flow cytometer, illustrating the fluidic, optical and electronic systems [60], [61].

In this work, analysis was performed on MACSQuant® Analyzer (Miltenyi Biotec, Germany) with the following laser configuration: 488 nm laser and 585/42 filter (detecting rhodamine B), 488 nm laser and 530/30 filter (detecting FITC and Alexa Fluor 488) and 488 nm laser and LP670 filter (detecting 7-AAD). Post-processing analyses were performed using FlowLogic V7.1 Software. Gating strategies included sequential exclusion of debris and doublets, viability-based discrimination, and identification of labelled CAR-T cells based on NP-derived fluorescence. Post-Ficoll analysis focused on labelling efficiency and viability of CAR-T cells, while post-coculture analysis assessed target cell killing and persistence of NP fluorescence in CAR-T cells.

2.5.4.1 Staining of labelled CAR-t cells after Ficoll purification

Labelled CAR-T cells obtained after Ficoll purification (Section 2.5.1) were stained for viability using the Viobility™ 488/520 Fixable Dye (Miltenyi, Biotec) following the

manufacturer's protocol with minor modifications. Briefly 5×10^4 cells per sample were resuspended in 100 µL of PBS without performing the initial wash step described in the standard procedure. 1 µL of Viobility™ dye was added per sample and the suspension was mixed gently and incubated 15 minutes at room temperature in the dark. After incubation, the samples were centrifuged at 1500 rpm for 5 minutes. The supernatant was removed, and cells were resuspended in 200 µL of buffer for flow cytometry acquisition.

Fluorescence from NP labelling was acquired directly without additional staining.

2.5.4.2 Staining of cells after co-culture

At the end of the co-culture period (Section 2.5.2), cells from each well were harvested for Flow Cytometry analysis. Each well was first washed with PBS to remove residual medium, then incubated with trypsin to detach cells. The resulting cell suspension was collected and centrifuged at 1500 rpm for 5 minutes.

The supernatant was aspirated, and the pellet was resuspended in 100 µL of PBS. 1 µL of Viobility™ 488/520 Fixable Dye was added per sample, followed by incubation for 15 minutes at room temperature in the dark.

After incubation, cells were centrifuged again at 1500 rpm for 5 minutes. The supernatant was aspirated, and the pellet was resuspended in 25 µL of antibody mix prepared with 200 µL of staining buffer, 2 µL each of anti-B7H3 and anti-CD3 antibodies, and 4 µL of anti-CSPG4. Cells were incubated with the antibody mix for 5 minutes at room temperature in the dark.

Finally, the sample volume was adjusted to 200 µL with staining buffer before acquisition by flow cytometry.

2.5.5 ^{19}F-NMR

The ^{19}F NMR acquisition method was previously described in Section 2.3.3. Briefly, after the Ficoll purification procedure (Section 2.5.1), ^{19}F-labelled CAR-T cells were resuspended in PBS. A lysis buffer was then added to reach a final volume of 400 µL with a concentration of 2.5% Triton X-100. Sample was transferred into coaxial NMR tubes, together with an external reference as previously described.

Number of ^{19}F atoms per cell was determined with the same equation as above and divided by the number of cells in each NMR tube. In this way it was possible to determine the nanoparticle uptake by the CAR-T cells.

^{19}F quantification by NMR provides an indirect estimate of the potential detectability of labelled cells by ^{19}F-MRI.

3 Results and discussion

3.1 Nanoparticles formulation and characterization

In this work, nanoparticles were formulated according to the emulsification solvent evaporation method, following the optimized protocol reported by Chirizzi et al [55]. In particular, the synthesis was designed to reproduce the formulation of PERFECTA-loaded PLGA nanoparticles stabilized with sodium cholate (NaC), which had previously demonstrated excellent colloidal stability, efficient encapsulation of the fluorinated probe, and suitability for ^{19}F-MRI detection.

Obtained NPs were characterized by different techniques, used for in vitro CAR-T cells labelling and labelled cells were analysed by ^{19}F NMR and Flow Cytometry.

3.1.1 PERFECTA@PLGA-NaC NPs preparation protocol

The method relies on the dissolution of both PLGA and PERFECTA in ethyl acetate, followed by emulsification in an aqueous solution containing NaC and solvent evaporation to obtain a stable colloidal dispersion. The complete description of the experimental procedure is reported in section 2.2. The main formulation parameters used for the synthesis of the NPs are summarized in Table 3.1.

Organic solvent	**Ethyl Acetate**
Temperature during stirring	25°C
PLGA content	20 mg
PERFECTA content	20 mg
NaC content	0.5% w/v NaC/aqueous phase
Tip sonication	40% amplitude, 25 seconds
Centrifuge	10733 g, 40 minutes, 4°C

Table 3.1 Summary of formulation parameters.

Ethyl acetate (EtOAc) was selected as the organic solvent after a preliminary solubility screening aimed at identifying a solvent capable of efficiently dissolving both PLGA and PERFECTA [55]. The complete dissolution of the solid probe PERFECTA in non-fluorinated organic solvents represented a critical step, as an incomplete solubilization directly compromises nanoparticle homogeneity, colloidal stability, and encapsulation efficiency. Several organic solvents commonly employed for PLGA nanoparticle preparation were investigated, including acetone, dichloromethane, tetrahydrofuran, and hexafluoroisopropanol; however, only ethyl acetate enabled the simultaneous

dissolution of both PERFECTA and PLGA while maintaining suitable conditions for standard O/W emulsification procedures [55].

Importantly, EtOAc allowed the production of monodisperse nanoparticles (PDI < 0.25) characterized by the highest PERFECTA encapsulation efficiency among the tested solvents, reaching values up to 61% of the initial fluorine content as quantified by ^{19}F NMR. In contrast, alternative solvents either resulted in poor PERFECTA solubility. On this basis, ethyl acetate was selected as the organic phase in the present work, as it represents the optimal compromise between fluorinated probe solubility, nanoparticle colloidal stability, and encapsulation efficiency, which are essential requirements for achieving high fluorine loading and reliable ^{19}F-based detection.

Organic solvent	**PERFECTA solubility**	**PERFECTA solubility**	**PDI**	**PERFECTA encapsulation efficiency (%)**
Ethyl Acetate (EtOAc)	+ +	+ +	0.1 ± 0.04	up to 61
Acetone	+	+ +	0.13 ± 0.03	0.13
Dichloromethane (DCM)	-	+ +	-	-
Chloroform/Solkane (1:5 v/v)	+ +	-	> 0.4	-
Hexafluoroisopropanol (HFIP)	+ +	+ +	> 0.4	-
Tetrahydrofuran (THF)	-	+ +	-	-

Table 3.2 PERFECTA solubility in different organic solvents and NP properties [55].

The encapsulation of PERFECTA within the PLGA matrix was optimized to maximize the fluorine payload while preserving nanoparticle integrity. PERFECTA is a small, symmetric molecule bearing 36 magnetically equivalent fluorine atoms, which give rise to a single sharp resonance in ^{19}F NMR and make it particularly suitable for quantitative imaging applications. Process parameters such as the polymer-to-probe ratio, solvent volume, and emulsification energy were carefully balanced to ensure homogeneous distribution of the fluorinated probe within the polymeric core and to obtain nanoparticles with uniform morphology and narrow size distribution.

Sodium cholate (NaC) was selected as the stabilizing agent based on its well-established ability to enhance cellular internalization of PLGA nanoparticles compared to conventional steric stabilizers such as poly(vinyl alcohol) (PVA).Previous studies conducted by the research group demonstrated that, despite comparable physicochemical properties, PVA-stabilized PLGA nanoparticles are

internalized to a significantly lower extent than nanoparticles stabilized with ionic surfactants. In contrast, NaC- and chitosan-stabilized formulations showed markedly higher cellular uptake and improved labelling efficiency.

Further evidence supporting the choice of sodium cholate derives from earlier experimental work within the same research framework. In particular, the thesis work of Martina Paraggio, focused on neuronal stem cells, demonstrated that NaC-stabilized PLGA nanoparticles were considerably more effective for cellular labelling compared to alternative stabilizers. These findings highlighted the central role of nanoparticle surface chemistry in governing nanoparticle–cell interactions and ultimately determining labelling efficiency.

On the basis of this consolidated experimental background, the present study adopts the PLGA–NaC formulation as a validated and reproducible platform, extending its application to CAR-T cells. This approach leverages formulation strategies already optimized by the research group, enabling direct comparison with previously published data and ensuring consistency across different biological models.

Overall, the combination of ethyl acetate as the organic solvent, PLGA as the polymeric matrix, and sodium cholate as the stabilizing agent resulted in a robust and reproducible nanoparticle formulation, specifically optimized for high fluorine loading, efficient cellular internalization, and compatibility with subsequent biological assays and ^{19}F-based detection techniques.

3.1.2 Physical chemical characterization of NPs

The colloidal stability of PERFECTA@PLGA–NaC nanoparticles was first evaluated in Milli-Q water (mQw) to determine their hydrodynamic size and surface charge. NPs were diluted 1:100 (v/v) in mQw for the measurement of the hydrodynamic diameter and polydispersity index (PdI) by Dynamic Light Scattering (DLS).

For the determination of the electrokinetic Zeta Potential and conductivity, a higher particle concentration was required; therefore, samples were diluted 1:5 (v/v) in mQw, reaching a final volume of 800 μL.

As shown in figure 3.1, DLS analysis showed an average hydrodynamic diameter of approximately 120 nm with a narrow size distribution (PDI < 0.2), indicating a homogeneous nanoparticle dispersion. The analyses were conducted at four different detection angles (70°, 90°, 110° and 130°).

The Zeta Potential value of – 43 mV confirmed the negative surface charge provided by the sodium cholate stabilizer, which contributes to electrostatic repulsion between particles and prevents aggregation in aqueous media.

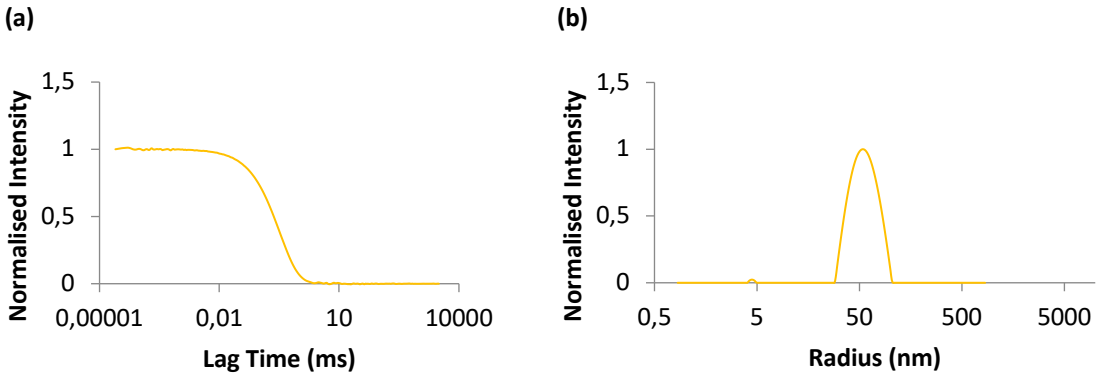

Figure 3.1 DLS (a) autocorrelation functions and (b) unweighted size distribution of NPs diluted in mQw water measured at 90°.

Hydrodinamic diameter [nm] (SD)	PdI (SD)	Z-Potential [mV] (SD)	Conductivity (mS/cm)
118 (9)	0.19 (0.03)	-43 (4.0)	0.046

Table 3.3 DLS characterization, Z-Potential, conductivity.

The colloidal stability of the NPs was also investigated in physiological conditions and in the presence of proteins. To assess NP stability in biological environments, time-dependent DLS and Zeta-Potential measurements were performed in three different media:

- T Cell Medium unconditioned (standard T cell culture medium as described in Section 2.1.2.1.),
- TCM conditioned by incubation with CAR T cells for 6 hours
- TCM without FBS.

Samples were diluted 1:6 (v/v) in the selected media and incubated at 37 °C to reproduce the same dilution used during in vitro experiments. DLS measurements were performed at the end of each time point (T0, 1, 6, and 24 hours) to monitor possible variations in hydrodynamic diameter and polydispersity index (PdI).

For the evaluation of surface charge and conductivity, an additional purification step was required to remove unbound proteins and medium components.

For each time point, the NP suspensions were processed according to the sucrose cushion isolation method described in Section 2.4.2, enabling the recovery of nanoparticle–protein complexes. After the third centrifugation step, the isolated pellets were resuspended and diluted 1:5 (v/v) in Milli-Q water (final volume 800 µL)

before performing Zeta Potential measurements. This procedure ensured that the electrokinetic properties reflected only the NPs with their adsorbed protein corona, avoiding artefacts due to residual proteins in the supernatant.

The results are presented in Figures 3.2–3.4 and Table 3.4-3.5. In each graph, the dotted line corresponds to the reference measurement performed in mQw, reported for comparison to highlight the effect of the different biological media on NP stability.

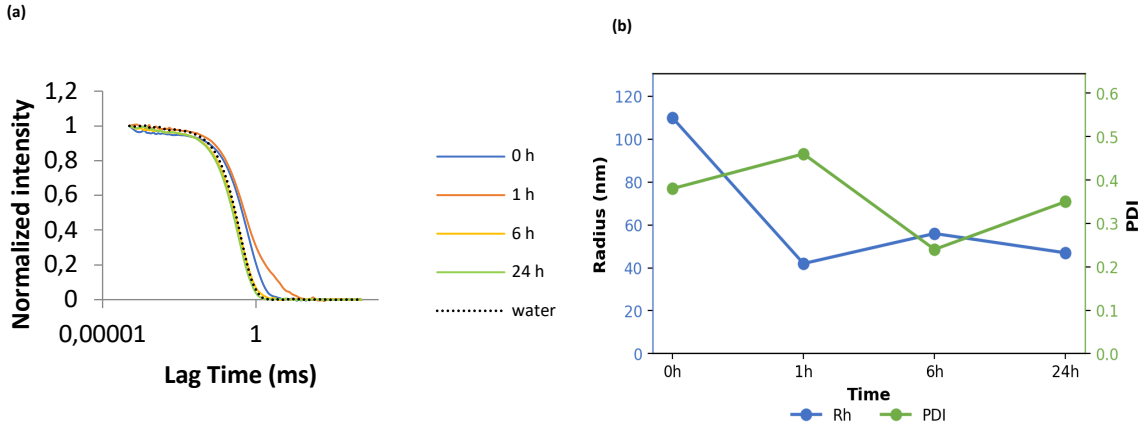

Figure 3.2 DLS stability analysis NPs in cell-conditioned medium over 24 hours. (a) Autocorrelation functions at t_0, 1 h, 6 h, and 24 h. (b) Hydrodynamic radius (Rh, blue) and polydispersity index (PDI, green) as a function of incubation time. Measurements were performed at 90° at a 1:6 (v/v) dilution.

Sample	Z-Potential (mV)	SD (mV)	Conductivity (mS/cm)
water	- 43	4	0.046
t = 0	-32	3	0.045
t = 1h	-29	3	0.048
t = 6 h	-26	3	0.044
t = 24 h	-27	3	0.048

Table 3.4 Z-Potential values, standard deviation and conductivity of NPs in cell-conditioned medium for 6 hours measured at 90°.

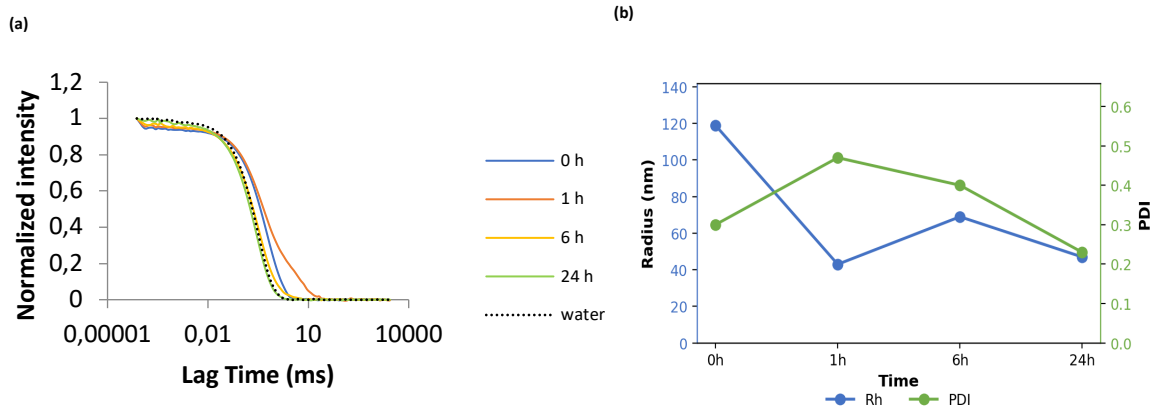

Figure 3.3 DLS stability analysis NPs in unconditioned medium over 24 hours. (a) Autocorrelation functions at t_0, 1 h, 6 h, and 24 h. (b) Hydrodynamic radius (Rh, blue) and polydispersity index (PDI, green) as a function of incubation time. Measurements were performed at 90° at a 1:6 (v/v) dilution.

Sample	Z-Potential (mV)	SD (mV)	Conductivity (mS/cm)
water	-43	4	0.048
t = 0	-29	3	0.047
t = 1h	-9	1	0.043
t = 6 h	-27	3	0.046
t = 24 h	-28	3	0.047

Table 3.5 Z-Potential values, standard deviation and conductivity of NPs in unconditioned medium.

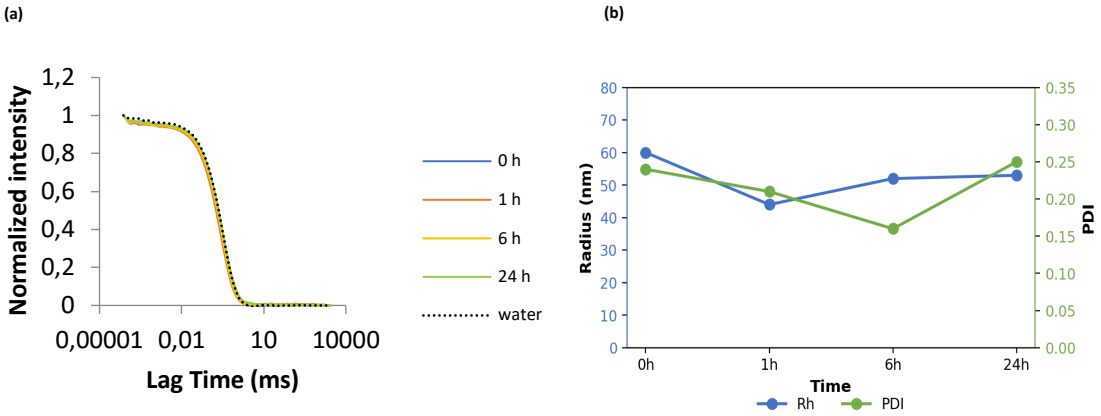

Figure 3.4 DLS stability analysis NPs in medium without FBS over 24 hours. (a) Autocorrelation functions at t_0, 1 h, 6 h, and 24 h. (b) Hydrodynamic radius (Rh, blue) and polydispersity index (PDI, green) as a function of incubation time. Measurements were performed at 90° at a 1:6 (v/v) dilution

In both unconditioned and cell-conditioned media (Figures 3.2 and 3.3), a decrease in hydrodynamic radius was observed within the first hour of incubation, likely attributable to the interaction with serum proteins and the formation of a protein corona, which may lead to a more compact colloidal structure. At later time points (6 to 24 hours), the size remained relatively stable, suggesting equilibrium in the protein corona organization.

In contrast, for NPs incubated in TCM without FBS (Figure 3.1), no significant time-dependent variations in hydrodynamic radius were observed, with both size and PDI values remaining comparable across all time points, confirming the intrinsic colloidal stability of the formulation in serum-free conditions.

Zeta-Potential measurements revealed interesting temporal dynamics that differed between Tables 3.3 and 3.4. In both conditioned and unconditioned TCM, a reduction in the absolute value of surface potential was observed compared to the reference measured in mQw (–43 mV), consistent with partial neutralization of surface charge caused by the adsorption of serum proteins and ions from the biological media. However, an apparent discrepancy emerges when comparing the two tables: in Table 3.4 (unconditioned TCM), the zeta potential at t=1h reaches approximately –9 mV, representing substantial charge neutralization, before increasing again in absolute value at later timepoints. This temporal pattern mirrors the behavior observed in the DLS measurements, where particle size initially increases and then decreases, suggesting coordinated evolution of both structural and electrokinetic properties during protein corona formation and reorganization. The initial reduction in zeta potential magnitude at t=1h likely reflects rapid adsorption of a loosely organized protein layer that substantially neutralizes surface charge, while the subsequent recovery toward more negative values may indicate rearrangement into a more compact and structured corona that partially re-exposes the underlying negatively charged nanoparticle surface.

To further confirm these observations, extended kinetic studies were performed up to 72 hours in both conditioned and unconditioned TCM (Figures 3.5–3.6). In both

conditions, the hydrodynamic radius showed an initial decrease during the first hours of incubation, consistent with the formation and reorganization of the protein corona. From 24 hours onward, both size and PDI values stabilized, with the hydrodynamic radius reaching a plateau around 50–60 nm and PDI values decreasing below 0.25, indicating the achievement of a stable colloidal state. These results suggest that, despite initial dynamic interactions with the biological environment, PLGA-NaC nanoparticles maintain their colloidal integrity over extended incubation periods.

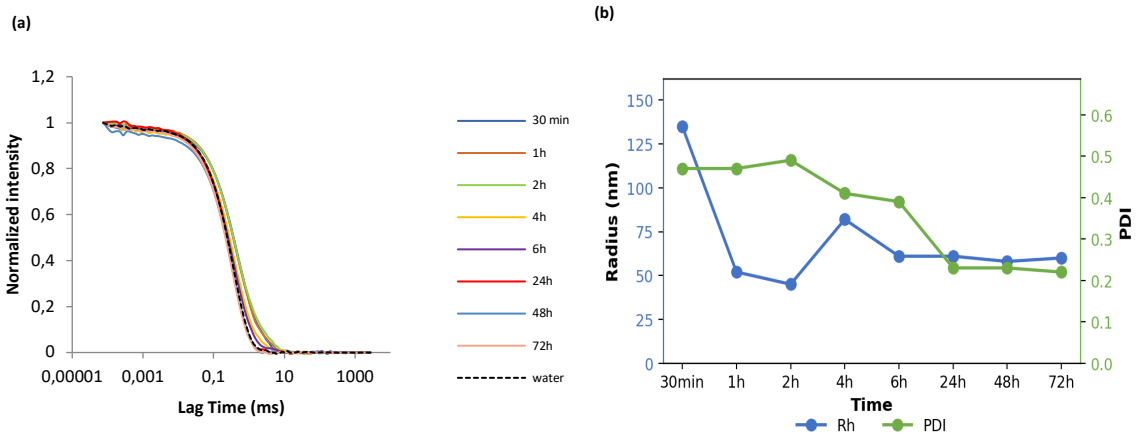

Figure 3.5 DLS stability analysis NPs incell-conditioned medium over 72 hours. (a) Autocorrelation functions at t_0, 1 h, 6 h, and 24 h. (b) Hydrodynamic radius (Rh, blue) and polydispersity index (PDI, green) as a function of incubation time. Measurements were performed at 90° at a 1:6 (v/v) dilution.

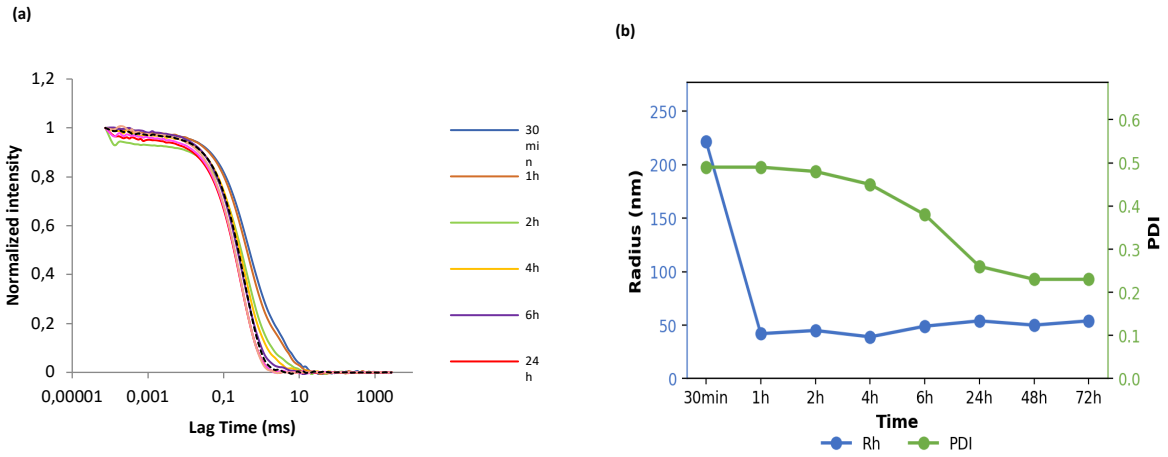

Figure 3.6 DLS stability analysis NPs in unconditioned medium over 72 hours. (a) Autocorrelation functions at t_0, 1 h, 6 h, and 24 h. (b) Hydrodynamic radius (Rh, blue) and polydispersity index (PDI, green) as a function of incubation time. Measurements were performed at 90° at a 1:6 (v/v) dilution.

Although a protein corona forms and evolves over time, as evidenced by changes in hydrodynamic diameter, PdI, and zeta potential, in no case was extensive aggregation and/or precipitation observed. Therefore, the NPs remain colloidally stable in culture medium despite the formation of the protein corona. This colloidal stability is essential for maintaining nanoparticle dispersion during the 6-hour labelling incubation with

CAR-T cells and ensures reproducible cellular exposure to individual nanoparticles rather than large aggregates.

These physicochemical characterization results were subsequently compared with protein corona composition analysis by SDS-PAGE and structural characterization by FTIR spectroscopy to explore possible correlations between colloidal stability parameters and the identity of adsorbed proteins in the different media, as discussed in Section 3.1.4.

3.1.3 Protein corona analysis and SDS-PAGE

To gain deeper insight into the behaviour of NPs in in vitro studies, a comprehensive analysis was performed to understand the formation and kinetic evolution of the protein corona. This process initiates as soon as NPs encounter a protein-rich biological environment, where proteins spontaneously adsorb onto the NP surfaces. The resulting corona consists of two distinct components: the hard corona, composed of proteins that are tightly bound and exchange slowly, and the soft corona, which includes proteins that are dynamically bound and frequently exchanged with the surrounding medium. The distinction between hard and soft coronas is critical, as these layers define the biological identity of NPs and shape their interaction with cells and biological systems

In this study, the kinetics of protein corona formation were investigated by incubating NPs with the cellular environment at distinct time points: immediate contact (T0), 1 hour, 6 hours, and 24 hours. This time-resolved approach is informative for characterizing not only the initial adsorption events, but also the evolution and stabilization of the corona over time. It is well established that the composition and structural properties of the corona can change significantly during the initial hours of exposure, as proteins with higher affinity gradually displace those with lower affinity in a dynamic exchange process. Early time points, such as 1 hour, often capture the formation of a transient corona, while extended incubation allows observation of the more stable corona layer, which is generally established after several hours of continuous interaction

Incubation experiments were performed using two different media conditions: standard T cell culture medium (TCM) and TCM previously conditioned by exposure to CAR-T cells for 6 hours. This experimental design enabled a comparative assessment between protein corona formed in a pristine cell culture environment and in presence of cellular secretome components released by CAR-T cells during active culture. The inclusion of conditioned TCM is particularly relevant, as secreted cytokines, growth factors, and extracellular vesicles can alter both composition and kinetic profile of proteins adsorbing onto the nanoparticle surface, with downstream effects on biological identity and nanoparticle–cell interactions

After incubation, nanoparticle–protein complexes were isolated using the sucrose cushion centrifugation method described in Section 2.4.2, enabling the recovery of the hard corona fraction. Subsequently, the isolated nanoparticle–protein complexes were analysed by SDS-PAGE to characterise the protein composition of the corona.

The results obtained from these analyses were compared with those of the stability tests reported in Section 3.1.2 to explore possible correlations between colloidal stability and protein adsorption in the different media.

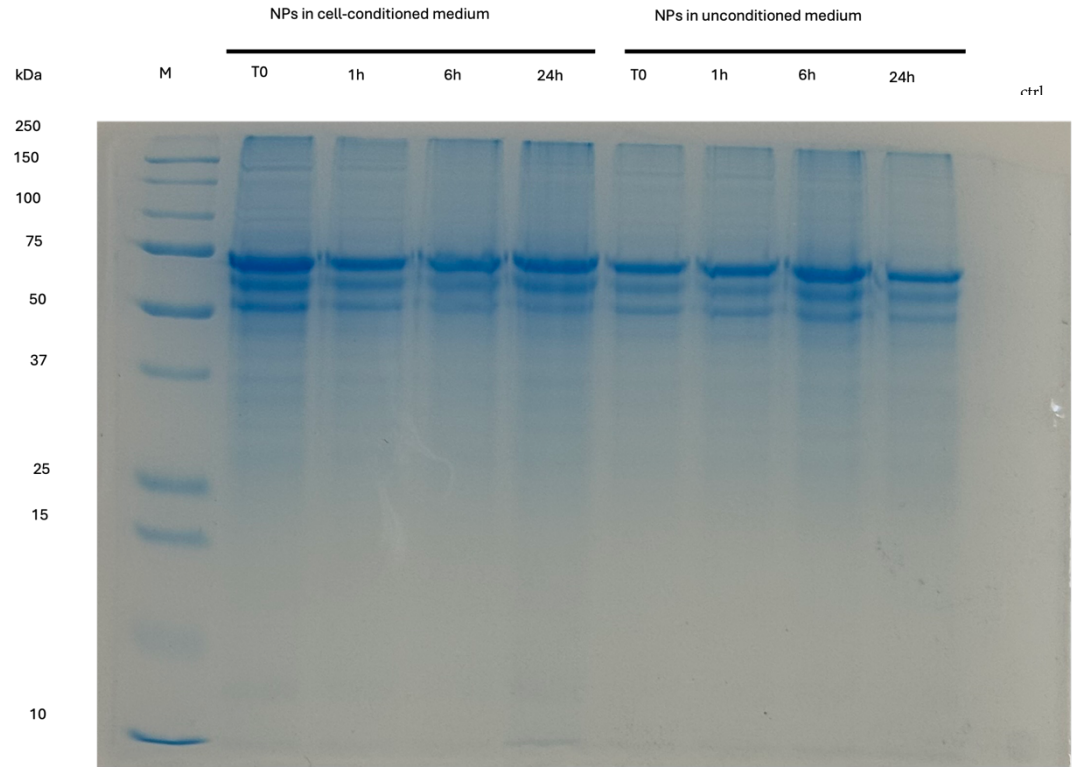

Figure 3.7 1D SDS-PAGE gel obtained from the hard corona of PLGA-NaC NPs for increasing incubation times (T0 to 24 hours) in cell-conditioned and unconditioned culture medium. Marker proteins column (M) was used to establish the length of protein bands.

As can be seen in the figure, visual inspection of the SDS–PAGE gel reveals some differences between the nanoparticles incubated in TCM and those incubated in TCM conditioned by CAR T cells. In both conditions, several well-defined bands are visible, mainly between 75 and 37 kDa, consistent with the molecular weights of several serum proteins, but to have protein identity would be necessary to run MS analysis. The presence of these bands indicates that, even after incubation, proteins remain strongly adsorbed on the nanoparticle surface, forming a protein corona.

In the sample incubated in conditioned TCM, the bands appear slightly more intense, particularly in the 75–37 kDa region, suggesting that additional proteins secreted by the cells contribute to a denser corona. Moreover, at 24 hours, new bands appear at

lower molecular weights, indicating the adsorption of smaller proteins or protein fragments, possibly resulting from degradation or from cellular secretions present in the conditioned medium.

The overall comparison between the two conditions confirms that exposure to a biologically active medium promotes the enrichment and diversification of the protein corona.

While SDS-PAGE provided information on the identity and relative abundance of proteins adsorbed onto the nanoparticle surface, this technique does not reveal whether protein binding induces chemical modifications or conformational changes in the nanoparticle surface components themselves. To address this question, Fourier Transform Infrared (FTIR) spectroscopy was employed as a complementary analytical technique."

3.1.4 Fourier Transform Infrared Spectroscopy Analysis

To complement the protein corona characterization obtained through SDS-PAGE analysis, Fourier Transform Infrared (FTIR) spectroscopy was employed to investigate potential chemical interactions between the nanoparticle surface components and the adsorbed protein layer. FTIR provides information about the vibrational modes of molecular bonds, enabling detection of conformational changes or chemical modifications that may occur during protein corona formation.

FTIR spectra were acquired for pure components (sodium cholate stabilizer and medium), the complete nanoparticle formulation, and nanoparticle-protein complexes isolated after incubation in both cell-conditioned and unconditioned culture media at different timepoints (1 hour and 24 hours). The analysis focused particularly on the characteristic absorption bands of sodium cholate, as this amphiphilic molecule forms the nanoparticle surface and represents the primary interface for protein interactions.

Pure sodium cholate exhibited a sharp, well-defined absorption band at 1549 cm^{-1}, corresponding to the C=O carboxyl group stretching vibration characteristic of the bile salt structure. However, when sodium cholate was incorporated into the PLGA nanoparticle formulation, this peak underwent a notable shift and broadening, appearing at 1652 cm^{-1} in the PERFECTA@PLGA-NaC nanoparticles. This spectral change reflects the altered chemical environment of the sodium cholate molecules when associated with the PLGA polymer matrix, likely indicating hydrogen bonding interactions or conformational rearrangements at the polymer-stabilizer interface.

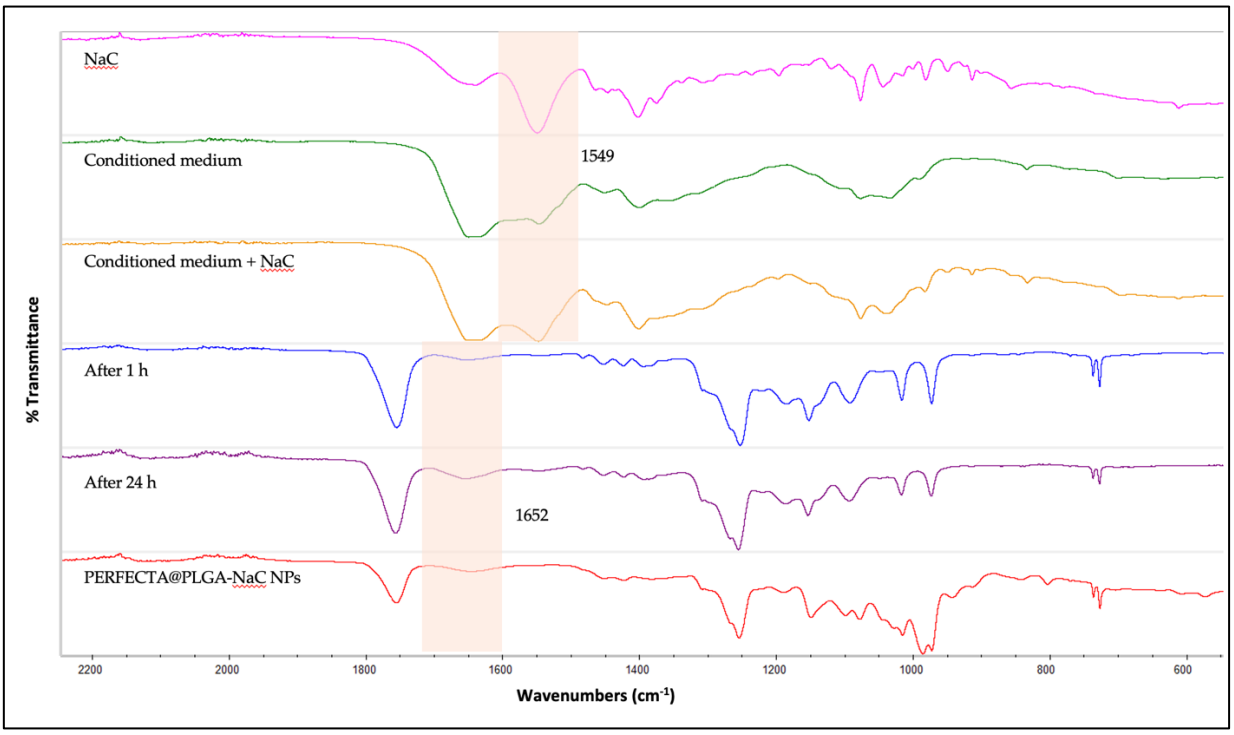

Figure 3.8 FTIR spectra showing the characteristic C=O stretching region. Pure sodium cholate displays a sharp peak at 1549 cm⁻¹, while sodium cholate incorporated into PLGA nanoparticles shows a broadened peak at 1652 cm⁻¹. Nanoparticle complexes isolated after 1 hour and 24 hours of incubation in cell-conditioned medium maintain the characteristic 1652 cm⁻¹ peak, indicating structural stability of the nanoparticle core despite PC formation.

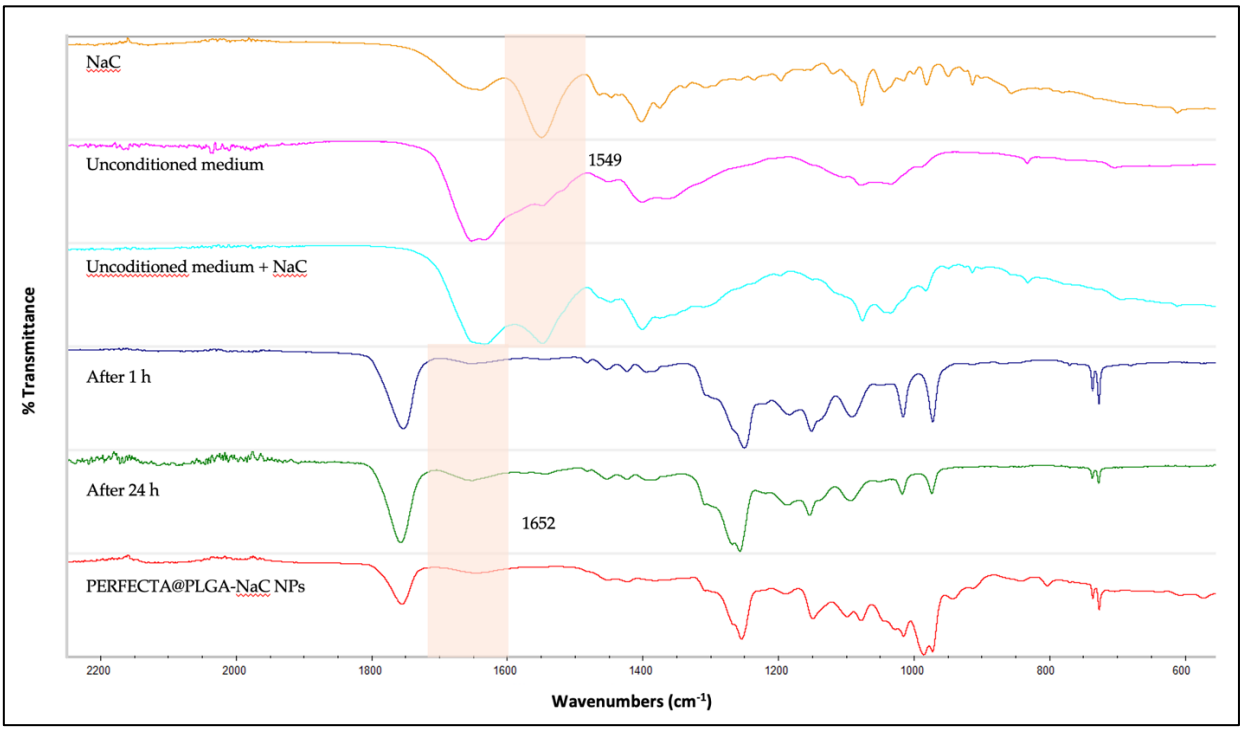

Figure 3.9 FTIR spectra showing the characteristic C=O stretching region. Pure sodium cholate displays a sharp peak at 1549 cm⁻¹, while sodium cholate incorporated into PLGA nanoparticles shows a broadened peak at 1652 cm⁻¹. Nanoparticle

complexes isolated after 1 hour and 24 hours of incubation in unconditioned medium maintain the characteristic 1652 cm^{-1} peak, indicating structural stability of the nanoparticle core despite PC formation.

As shown in figures 3.6 and 3.7, following incubation of nanoparticles in both cell-conditioned and unconditioned culture media, FTIR analysis of the isolated nanoparticle-protein complexes revealed that the characteristic absorption band at 1652 cm^{-1} remained essentially unchanged at both the 1-hour and 24-hour timepoints. The peak position showed no significant shift, indicating that the core nanoparticle structure, including the PLGA-sodium cholate interface, remained stable throughout the protein corona formation and evolution process. Protein corona signals - the amide I (~1600–1700 cm^{-1}) and amide II (~1500–1600 cm^{-1}) bands – are not visible, maybe due to sensitivity limitations. Variations in the spectra of the pristine NPs and PC NPs are instead observed in the fingerprint region around 1000 cm-1, but they are difficult to attribute.

The preservation of the sodium cholate spectral signature at both timepoints suggests that protein adsorption onto the nanoparticle surface occurs through relatively weak interactions that do not fundamentally disrupt the underlying nanoparticle architecture or induce major conformational changes in the surface-stabilizing molecules.

Comparison between samples incubated in cell-conditioned medium (containing secreted cellular factors and conditioned proteins) and unconditioned medium (containing only serum proteins from the culture medium formulation) showed no significant differences in the FTIR spectra of the nanoparticle-protein complexes. This suggests that the physical structure and chemical interactions governing protein corona formation are primarily determined by the intrinsic nanoparticle surface properties and the abundant serum proteins present in both media, rather than by the relatively dilute cellular secretome components in the conditioned medium.

The combined analysis of DLS, SDS-PAGE, and FTIR data provides a comprehensive picture of protein corona dynamics. While DLS measurements indicated temporal evolution in nanoparticle size and surface properties during protein corona formation, particularly the reorganization observed between early (1 hour) and later (24 hours) timepoints discussed in Section 3.1.2, and SDS-PAGE revealed relatively stable protein composition across timepoints, FTIR demonstrated that the nanoparticle core structure remained intact while showing subtle changes in surface accessibility reflected in peak area variations. This multitechnique characterization suggests that the dynamic processes occurring during protein corona maturation involve primarily reorganization and compaction of the adsorbed protein layer rather than chemical modification of the nanoparticle constituents or wholesale exchange of protein species.

These FTIR results provide important complementary information to the protein composition analysis obtained through SDS-PAGE. While electrophoresis revealed which proteins were present in the corona and how their relative abundances evolved over time, FTIR confirmed that these adsorption processes did not induce chemical changes in the nanoparticle surface components, though the protein layer development did influence the infrared spectral characteristics in ways consistent with progressive corona maturation. This stability is particularly relevant for the cell labelling application, as it indicates that the nanoparticles maintain their designed structure and surface chemistry throughout the incubation period in biological media, ensuring reproducible interactions with cells regardless of the specific protein corona composition that forms under different experimental conditions.

3.1.5 ^{19}F NMR results and quantification

The fluorine content of the nanoparticle formulation was evaluated by ^{19}F Nuclear Magnetic Resonance (NMR) spectroscopy to confirm the successful encapsulation of the fluorinated probe PERFECTA within PLGA nanoparticles and to quantify the amount of fluorine per sample. This analytical technique provides a direct and specific detection of fluorinated compounds, allowing both qualitative and quantitative assessment of the encapsulated material.

^{19}F NMR spectra were acquired in the conditions described in Section 2.3.3. Briefly, ^{19}F NMR spectra were collected using trifluoroacetic acid (TFA) as the external standard for quantification, due to its well-defined chemical shift and single sharp signal. The ^{19}F resonance of PERFECTA appeared as a single, narrow peak at −72.5 ppm, corresponding to the 36 magnetically equivalent fluorine atoms of the molecule. In Figure 12 ^{19}F-NMR spectra for a PLGA-NaC formulations is reported: it is possible to observe the characteristic peak of PERFECTA and a second peak, at -76.5 ppm, related to TFA.

For the quantification of ^{19}F concentration the following equation was used:

$$N_F^{19\mathrm{F}} = \frac{I_f}{I_{std}} N_F^{19\mathrm{F}}$$

Where I_f and I_{std} are the integral values of the peak related to PERFECTA and to the standard (TFA), respectively, while N_{std}^{19F} and N_f^{19F} are the total number of ^{19}F atoms in PERFECTA and in the standard, respectively. The solution of the standard had a total number of fluorine atoms equal to 1.7×10^{19} ^{19}F.

Substituting the experimental values in the equation it is possible to determine the number of fluorine atoms in the 0.4 mL used for the analysis, from that value the initial concentration of the stock formulation is calculated.

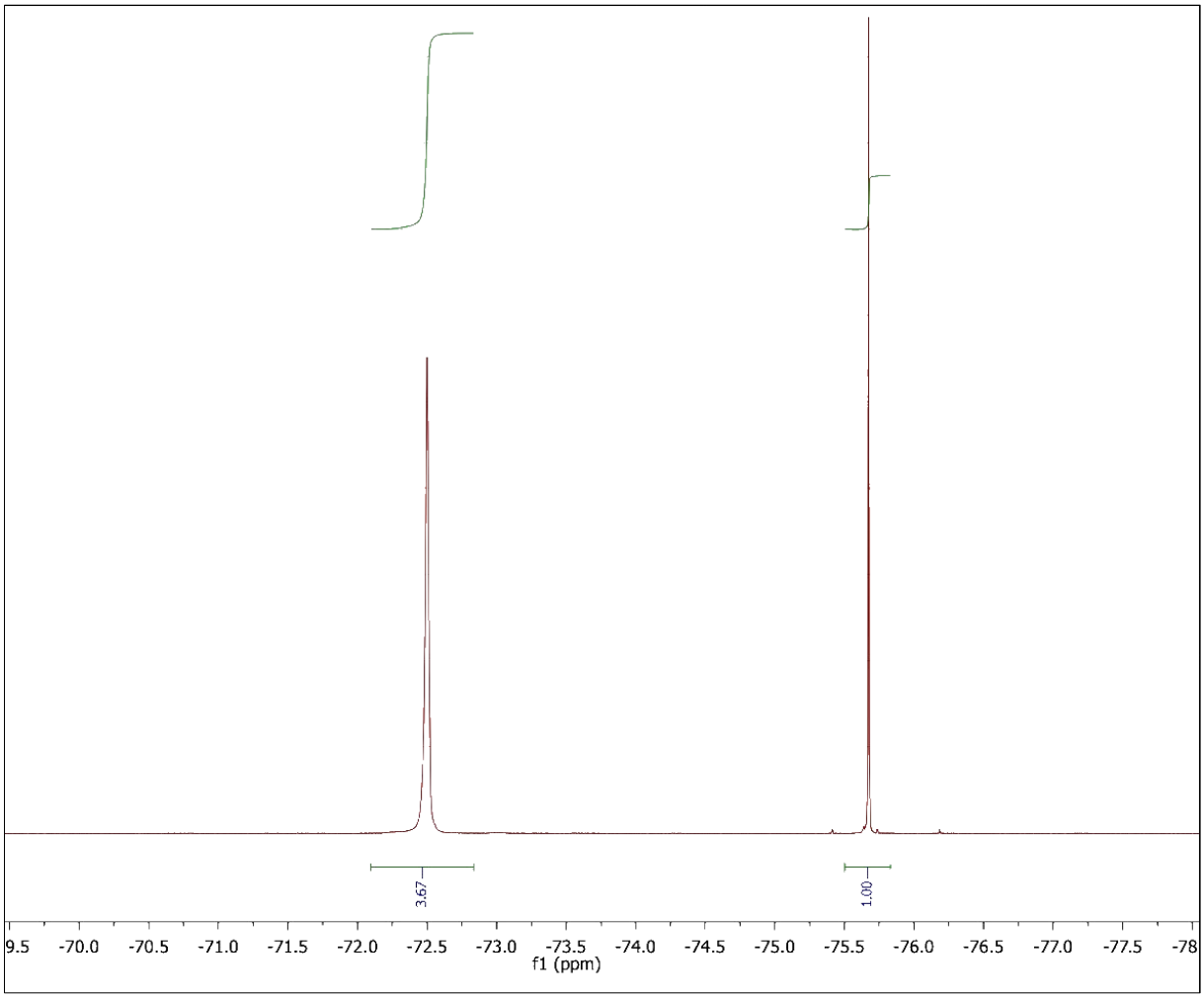

Figure 3.10 ^{19}F NMR spectrum of the NPs. PERFECTA peak (-72.4 ppm) and TFA peak (-75.5 ppm) are visible, with relative integral values used for fluorine atoms quantification.

So, according to the equation previously provided, it is possible to calculate the number of total fluorine atoms in the measured samples ($N_F{}^{19F}$), the concentration of fluorine atoms in the stocks (^{19}F/ml) and the encapsulation (%). PERFECTA encapsulation efficiency was determined by using the following equation:

$$\%\ encapsulation\ = \frac{Quantified\ 19F}{Theoretical\ 19F}\ \text{x}\ 100$$

All data are reported in Table 3.5. The determination of the fluorine concentration of the NPs represented a key parameter for all subsequent cellular experiments. This value allowed the calculation of the NP volume required for each labelling condition, ensuring consistency among different experimental setups.

By maintaining a fixed fluorine concentration per millilitre (F/mL) across all incubations, it is possible to standardize the exposure conditions and make the results obtained from different experiments directly comparable.

Theorical ^{19}F atoms (^{19}F/ml)	**Quantified ^{19}F atoms(^{19}F/ml)**	**SD**	**Encapsulation (%)**
$4.3x10^{20}$	$1.8x10^{20}$	0.2	41%

Table 3.6 Fluorine content and deviation standard measured through ^{19}F NMR of the formulation. Theorical ^{19}F atoms are the number of fluorine atoms added at the beginning of the formulation procedure and equivalent to 20 mg of PERFECTA.

3.2 *In vitro* experiments with CAR-T cells

A series of in vitro experiments were performed to evaluate the interaction between fluorinated NPs and CAR-T cells, investigating their labelling efficiency, cellular viability, and functional behaviour in co-culture systems.

The in vitro labelling experiments were performed using human B7-H3–targeting CAR-T cells, generated as described in Section 2.5.2. For labelling experiments, CAR-T cells were used 7–14 days after transfection, corresponding to a phase of sustained CAR surface expression and maintained antitumor effector function. Both freshly prepared and thawed CAR T cells were employed, and no significant differences in viability or labelling performance were observed between two conditions.

For all labelling experiments, NPs were routinely characterized in terms of size, surface charge and fluorine content as described in Sections 3.1.1 and 3.1.2, prior to cellular labelling. Fluorescently labelled PERFECTA@PLGA-NaC NPs containing 2% w/w PLGA-rhodamine B were used to enable their detection and quantification by flow cytometry. In each experiment, a portion of CAR-T cells was maintained unlabelled as controls (CTRL), to which the corresponding vehicle (Milli-Q water) was added instead of NP formulation.

Overall, thirteen independent experiments were carried out, progressively optimizing the experimental setup to ensure reproducibility, maximize cell recovery, and obtain sufficient labelled cells for comprehensive downstream analyses including flow cytometry, ^{19}F NMR/MRI, and co-culture experiments.

3.2.1 CAR-T cell labelling with PERFECTA loaded NPs

The labelling procedure was adapted from an optimized protocol originally developed for human neural progenitor cells (hNPC, GIBCO), maintaining a constant fluorine concentration of 3.13×10^{19} ^{19}F/mL in the incubation medium. This standardized approach ensured reproducible NP exposure and allowed for direct comparison across

different experimental setups. Additionally, three experiments were carried out using higher fluorine concentrations to evaluate whether an increased NP dose could improve cellular uptake efficiency or potentially compromise viability.

The thirteen labelling experiments were performed in three main phases, each employing a different culture format: one preliminary experiment in 24-well plates, six experiments in 50 mL tubes (including two optimization experiments performed without nanoparticles), and six experiments in T25 culture flasks, which represented the final optimized setup. CAR-T cells were incubated with NPs for 6 hours under standard culture conditions (37 °C, 5% CO_2, humidified atmosphere) following the protocol detailed in Section 2.5.1.

3.2.1.1 Evolution of experimental setup

The first experiment, conducted in 24-well plates, served as a preliminary assessment of NP uptake and initial definition of labelling parameters. Cells were seeded at a density of 3.5×10^5 cells per well in 1 mL of medium, allowing for rapid screening of labelling conditions. However, this format revealed a significant limitation: CAR-T cells showed a tendency to partially adhere to the plastic surface of the wells, resulting in substantial cell loss during sample collection after the labelling period. This adhesion-related loss, combined with the inherently small working volume and low initial cell number, made the 24-well plate format unsuitable for experiments requiring adequate cell yields for comprehensive downstream analyses.

The second phase was carried out using 50 mL tubes, which allowed a higher total number of cells per replicate and improved mixing homogeneity during incubation with nanoparticles. Two preliminary experiments were performed without nanoparticles to evaluate the optimal time point after CAR gene transfection of T cells for conducting the labelling, assessing whether CAR T cells at different post-transfection days showed differences in recovery and viability.

Days post-transfection	Starting n° of cells	n° of cells recovered	Recovery (%)
7	3×10^6 1.5×10^6 cells/tube (pool of 2 replicates)	793.2 k cells	26.4
10	3×10^6 1.5×10^6 cells/tube (pool of 2 replicates)	913 k cells	30.4

Table 3.7 Evaluation of cell recovery at different timepoints post-transfection. CAR-T cells were processed through the complete protocol (without NP incubation).

Based on these results, the optimal window for labelling was identified as 7-10 days post-transfection. Once this window was established, two additional labelling experiments were performed in 50 mL tubes under the standard fluorine concentration (3.13×10^{19} ^{19}F/mL), confirming the reproducibility of the protocol. However, despite improved performance compared to 24-well plates, this setup still presented limitations in overall cell yield, particularly when larger quantities of labelled cells were required.

The final phase employed T25 culture flasks, which provided a more suitable environment for large-scale labelling. The larger culture surface and greater medium volume ensured more homogeneous exposure of cells to nanoparticles and facilitated the recovery of sufficient labelled cells for subsequent flow cytometry, ^{19}F NMR/MRI, and functional co-culture analyses. Across this series of experiments, both freshly prepared and thawed CAR T cells were used, showing comparable viability and uptake performance. Additionally, three experiments were conducted at higher fluorine concentrations to evaluate whether increased nanoparticle doses could improve cellular uptake efficiency.

These considerations led to the adoption of T25 culture flasks as the final experimental configuration. This choice was driven by both technical requirements and biological considerations. Most importantly, T25 flasks represent the standard culture format routinely used for CAR-T cell expansion, making this setup inherently more biocompatible than either 24-well plates or conical tubes. By maintaining cells in their habitual culture environment throughout the labelling process, procedural stress was minimized and cells remained in optimal physiological condition.

Beyond biocompatibility, the T25 format offered substantial practical advantages. The larger culture surface and expanded medium volume (5 mL) accommodated 3.3 × 10^6^ cells, ensuring robust cell yields even after accounting for Ficoll-induced losses. This higher capacity enabled confident allocation of labelled cells across all planned analytical endpoints.

Six experiments were ultimately performed using T25 flasks, incorporating both freshly cultured and cryopreserved CAR-T cells. Importantly, no significant differences emerged between these two cell sources in terms of viability, labelling efficiency, or post-Ficoll recovery, confirming protocol robustness across different cell preparation methods. Three experiments employed the standard fluorine concentration (3.13×10^{19} ^{19}F/mL) to establish baseline performance, while the remaining three tested higher concentrations to determine whether increased nanoparticle doses could further enhance uptake without compromising cell health.

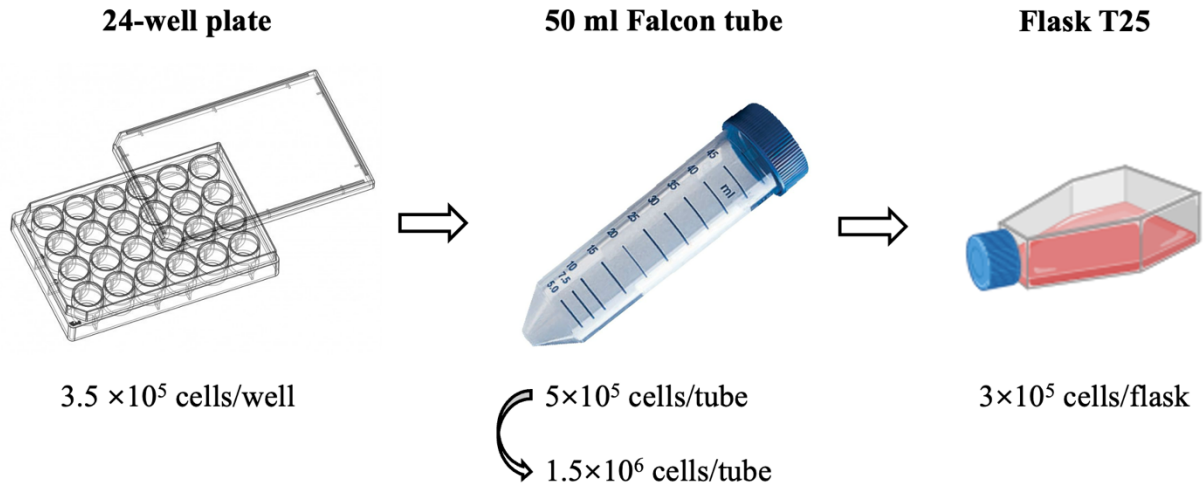

Figure 3.11 Evolution of experimental setup.

3.2.1.2 Ficoll purification and challenges in cell recovery

A critical step in the labelling protocol was the complete removal of free, non-internalized nanoparticles from the cell suspension following the 6-hour incubation period. This purification step proved essential for ensuring the accuracy and reliability of all subsequent analyses.

Traditional cell purification methods rely on repeated centrifugation and washing cycles to remove unbound material. However, this approach proved inadequate for CAR-T cell labelling with PERFECTA@PLGA-NaC nanoparticles. During centrifugation, both labelled cells and free NPs pellet together at the bottom of the tube

due to their similar sedimentation behaviours. Resuspending and washing the pellet cannot effectively separate internalized nanoparticles from those that are simply trapped within the cell pellet or loosely adhered to cell membranes. Consequently, conventional washing results in contaminated samples containing both labelled cells and free NPs, leading to aspecific signals that compromise the quantitative accuracy of ^{19}F NMR and MRI measurements.

This contamination issue is particularly problematic for cell tracking applications. Free nanoparticles co-administered with labelled cells could circulate independently in the bloodstream and accumulate in off-target organs, generating misleading biodistribution signals that would be incorrectly attributed to migrating CAR-T cells. Moreover, overestimation of cellular fluorine content due to free NP contamination would lead to erroneous predictions of imaging detectability and misinterpretation of cell numbers in target tissues.

To overcome this fundamental limitation, we implemented a purification strategy based on Ficoll density gradient centrifugation, a technique widely employed for the isolation of T lymphocytes from whole blood samples. This method exploits density differences between viable cells, dead cells, and nanoparticles to achieve effective separation.

During centrifugation on the Ficoll gradient, the sample stratifies into distinct phases: viable CAR-T cells, having intermediate density, accumulate at the interface between the culture medium and the Ficoll solution, forming a visible ring-like layer. Free nanoparticles, being denser than the Ficoll solution, sediment through the gradient and pellet at the bottom of the tube. Dead cells and cellular debris, also denser than viable lymphocytes, similarly pellet at the bottom. This spatial separation enables selective recovery of the cell-containing interface while leaving behind both free NPs and non-viable cellular material.

The complete Ficoll purification protocol is described in Section 2.5.1.2. Importantly, the same protocol was applied consistently across all thirteen labelling experiments without modifications, ensuring standardized purification conditions and enabling direct comparisons of cell recovery and labelling efficiency across different experimental setups.

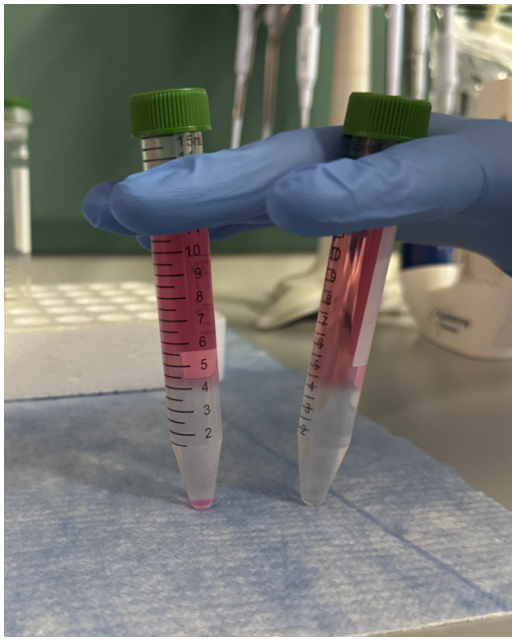

Figure 3.12 Formation of the cell layer at the Ficoll-medium interface after the first centrifugation. Left: labelled cells, showing a distinct interphase. Right: control cells, showing a clear interface.

While Ficoll purification successfully addressed the contamination problem by free NPs, it introduced a significant experimental challenge that became a critical phase in our optimization efforts: achieving adequate cell recovery. The interface layer containing viable labelled cells must be carefully collected without disturbing the gradient or contaminating the sample with either the upper medium phase (which may contain residual free NPs) or the lower Ficoll layer. This collection step proved technically demanding and required considerable practice to perform consistently.

Despite these technical challenges, we maintained the established protocol throughout all experiments to ensure consistency. The two-step centrifugation approach described in Section 2.5.1.2—combining cells recovered from both the primary Ficoll separation and a second centrifugation of the supernatant—helped improve overall recovery, though substantial losses remained a limiting factor.

To systematically characterize the impact of Ficoll purification on cell yields and to identify the specific procedural step responsible for cell losses, Trypan Blue exclusion assays were incorporated at multiple stages in the later experimental series:

1. Pre-Ficoll: Immediately following the 6-hour incubation with nanoparticles
2. Post-Ficoll: After density gradient separation and collection of the interface layer
3. Final: After washing in PBS and resuspension in the appropriate medium

This systematic counting approach enabled precise quantification of cell losses at each stage and revealed a critical finding: the major reduction in cell number

occurred specifically during the Ficoll purification step, while the preceding incubation and handling procedures had minimal impact on cell recovery.

Setup	Experiments (n)	Initial cells ($\times 10^6$)	Post-incubation ($\times 10^6$)	Post-Ficoll ($\times 10^5$)	Post-washing ($\times 10^5$)	Overall recovery (%) **
50 mL tube	1	3	2.3	8	1.4	6.1
T25 flask	5 (4 successful)	5.93 ± 2.57	4.60 ± 2.76	6.8 ± 6.6*	14.4 ± 23.7*	2.8 ± 2.7*

**High standard deviation due to one complete experimental failure (recovery = 0%)*

***Overall recovery = (Post-wash/ Initial) × 100*

Table 3.8 Cell recovery at different stages of the labelling protocol. Data are presented as mean ± standard deviation for T25 flask (n=5). For 50 mL tube format, systematic cell counting was performed only in the final experiment (n=1).

The data reveal substantial variability in recovery rates across T25 flask experiments, with an average overall recovery of 2.84 ± 2.72%. This high standard deviation reflects the technical challenges inherent to the Ficoll collection procedure.

For the 50 mL tube format, systematic cell counting was implemented only in the final experiment, which yielded an overall recovery of 6.1%. While this single datapoint precludes statistical comparison with the T25 format, it suggests that recovery rates were generally low across both experimental configurations, confirming that Ficoll-induced cell losses represented a consistent limitation of the purification strategy rather than a format-specific issue.

Despite these substantial recovery challenges, Ficoll density gradient purification remained indispensable to the labelling protocol. The trade-off between purity and recovery was therefore carefully managed: the substantial cell losses during Ficoll purification, though limiting, were accepted as a necessary cost to ensure the integrity and reliability of the labelling approach.

This strategic decision to prioritize sample purity directly influenced the experimental design trajectory. The transition to T25 culture flasks with higher initial cell numbers (5.93 ± 2.57 × 10^6^ cells) was essential to ensure that, even after accounting for the typical ~3% overall recovery, sufficient viable labelled cells (averaging 1.44 ± 2.37 × 10^5^ cells) remained for allocation across multiple analytical endpoints: flow cytometry (minimum 50,000 cells), ^{19}F NMR spectroscopy, and functional co-culture experiments.

However, the limited cell yields ultimately prevented acquisition of ^{19}F MRI images, as the recovered cell numbers fell below the typical detection threshold required for visualization. This limitation represents a critical area for future protocol optimization: improving Ficoll collection efficiency or exploring alternative purification strategies could enable recovery of cell numbers adequate for MRI-based validation, which would provide direct confirmation of the imaging potential demonstrated in previous studies using similar PLGA-based formulations [57].

Furthermore, flow cytometry analysis presented in the following section demonstrated that cells recovered from the Ficoll procedure maintained high viability and functional integrity, confirming that the purification step, despite its impact on cell yield, did not compromise the quality of the recovered labelled cell population.

3.2.2 Viability and cellular uptake

Following the 6-hour incubation with PERFECTA@PLGA-NaC nanoparticles and subsequent Ficoll purification, labelled CAR-T cells were comprehensively characterized to assess the impact of the labelling procedure on cell viability and to quantify nanoparticle internalization efficiency. This characterization phase was essential to validate the biocompatibility of the labelling protocol and to determine the cellular fluorine loading achieved—a critical parameter for predicting detectability in ^{19}F MRI-based cell tracking applications.

As discussed in Section 3.2.1.2, the limited cell yields resulting from Ficoll purification necessitated careful allocation of the recovered labelled cells across multiple analytical techniques. A standardized distribution strategy was implemented to maximize the information obtained from each labelling experiment while ensuring that all critical parameters could be assessed. Following Ficoll purification and final resuspension, recovered CAR-T cells were systematically allocated as follows: 50,000 cells for flow cytometry analysis (dual assessment of cell viability using Viobility Fixable Dye and quantification of nanoparticle internalization via rhodamine B fluorescence intensity, as described in Section 2.5.3), with remaining cells distributed between ^{19}F NMR spectroscopy for quantitative determination of cellular fluorine content and functional co-culture assays for evaluation of cytotoxic activity against U87 glioblastoma cells (Section 3.2.3).

In parallel with labelled samples, CTRL cells that had been incubated with an equivalent volume of Milli-Q water instead of the NP formulation were processed identically through the complete protocol, including Ficoll purification. These control samples were analysed alongside labelled cells to distinguish NP-specific effects from those attributable to general handling procedures or the purification process itself. This standardized allocation ensured that each experiment, despite the inherent cell recovery limitations, yielded comprehensive data on labelling efficiency, cell health, and functional preservation.

Flow cytometry provided rapid, quantitative assessment of two critical parameters following the labelling and purification protocol: cell viability and the efficiency of nanoparticle internalization within the CAR-T cell population. Analysis of Viobility Fixable Dye staining demonstrated that the labelling procedure did not induce significant cytotoxic effects in the majority of experiments. Across all labelling experiments with standard fluorine concentration (3.13×10^{19} ^{19}F/mL), labelled CAR-T cells exhibited an average viability of 95.0 ± 5.9%. This relatively high viability, though showing some variability across experiments, confirmed that the 6-hour exposure to PERFECTA@PLGA-NaC nanoparticles followed by Ficoll density gradient purification did not fundamentally compromise cell integrity in successfully recovered populations.

The observed variability in viability across experiments likely reflects differences in the initial health status of the CAR-T cell batches, variations in the post-transfection timepoint at which labelling was performed, and potential differences in cell handling during the Ficoll collection procedure.

Control cells processed through the identical protocol without nanoparticles showed comparable or higher viability in most experiments (average 88.5 ± 16.9%), confirming that the handling procedures and Ficoll purification did not inherently compromise cell health. The consistently high viability among labelled cells across all experiments validated the biocompatibility of the PERFECTA@PLGA-NaC nanoparticle formulation at the concentrations tested.

Rhodamine B fluorescence analysis revealed highly efficient and reproducible nanoparticle uptake across the CAR-T cell population. While control cells incubated with Milli-Q water displayed negligible background fluorescence, labelled cell populations exhibited strong positive signals indicative of successful nanoparticle internalization. Quantitative analysis demonstrated that an average of 99.1 ± 1.3% of cells (n=5) showed positive rhodamine B fluorescence, indicating nearly complete uptake of fluorescent nanoparticles across the population. This exceptionally high percentage of positive cells with minimal variability confirmed that the labelling protocol achieved remarkably homogeneous distribution of nanoparticles throughout the cell population rather than generating a mixed population of heavily labelled and unlabelled cells.

At the standard concentration, labelled cells showed rhodamine fluorescence averaging 39.2-fold higher than unlabelled controls across experiments; notably, despite substantial variability (SD ± 23.8) across batches and culture conditions, uptake remained consistently high.

Importantly, control cells incubated with Milli-Q water instead of nanoparticle formulation showed negligible rhodamine fluorescence (average 0.004 ± 0.009% positive cells), confirming that the fluorescence signal detected in labelled samples originated specifically from internalized PLGA-rhodamine B nanoparticles rather than

from cellular autofluorescence or non-specific background. This near-zero background in control samples validated the specificity of the rhodamine-based uptake quantification and demonstrated that the labelling protocol achieved true nanoparticle internalization rather than surface adhesion or artefactual signal.

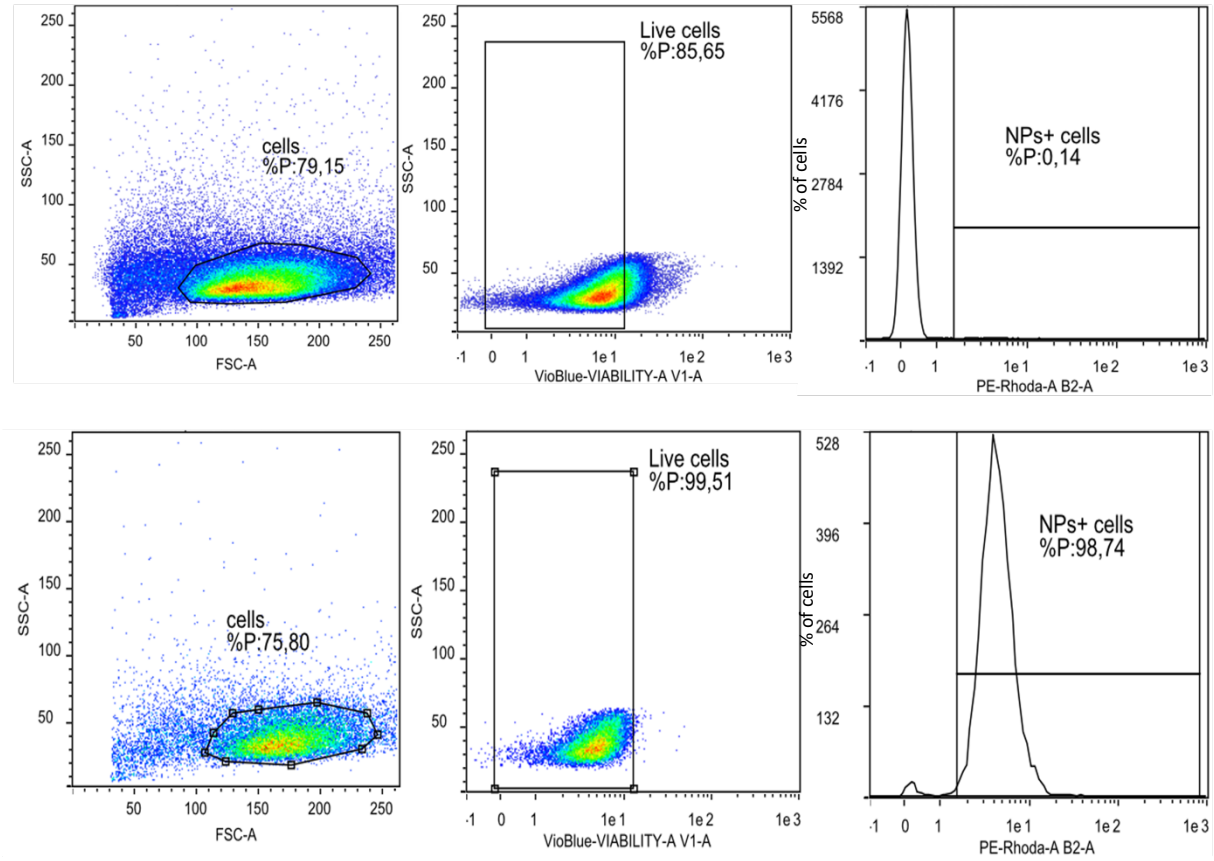

Figure 3.13 Representative flow cytometry analysis of CAR-T cell viability and nanoparticle uptake. Top panels: Unlabelled control cells incubated with Milli-Q water showing high viability (85.65%) and negligible rhodamine background (0.14% positive). Bottom panels: CAR-T cells labelled with PERFECTA@PLGA-NaC nanoparticles (standard concentration) showing maintained viability (99.51%) and efficient nanoparticle uptake (98.74% rhodamine-positive). The rightward shift in rhodamine fluorescence confirms successful nanoparticle internalization without compromising cell viability.

The combination of high viability and nearly complete nanoparticle uptake across the cell population confirmed that the optimized labelling protocol successfully achieved its dual objectives: efficient cellular loading with fluorinated nanoparticles while preserving cell health and integrity.

While flow cytometry confirmed efficient nanoparticle uptake via rhodamine fluorescence, ^{19}F Nuclear Magnetic Resonance spectroscopy provided direct, quantitative measurement of the fluorine content internalized by labelled cells—the parameter that ultimately determines detectability and quantification accuracy in ^{19}F MRI-based cell tracking applications. Following Ficoll purification, labelled CAR-T cells were collected, counted, and lysed with 2.5% Triton X-100 in PBS as described in

Section 2.5.4. Cell lysis was performed to homogenize the sample and facilitate reliable NMR acquisition during the initial calibration steps of the measurement, avoiding potential issues arising from sample heterogeneity or cellular compartmentalization of the fluorinated probe. The lysate was then analyzed by ^{19}F NMR using trifluoroacetic acid (TFA) as an external standard for quantitative calibration.

^{19}F NMR spectra of labelled cell lysates consistently showed a distinct resonance peak at −72.4 ppm, corresponding to the 36 magnetically equivalent fluorine atoms of the PERFECTA molecule encapsulated within the internalized nanoparticles. The presence of this characteristic peak, without detectable signals at other chemical shifts, confirmed successful nanoparticle internalization. Importantly, the absence of aspecific or anomalous signals validated the effectiveness of the Ficoll purification strategy in eliminating contaminating free nanoparticles from the samples, ensuring that the measured fluorine signal originated exclusively from cell-internalized PERFECTA@PLGA-NaC nanoparticles. Figure 3.Y shows a representative ^19^F NMR spectrum from labelled CAR-T cell lysate.

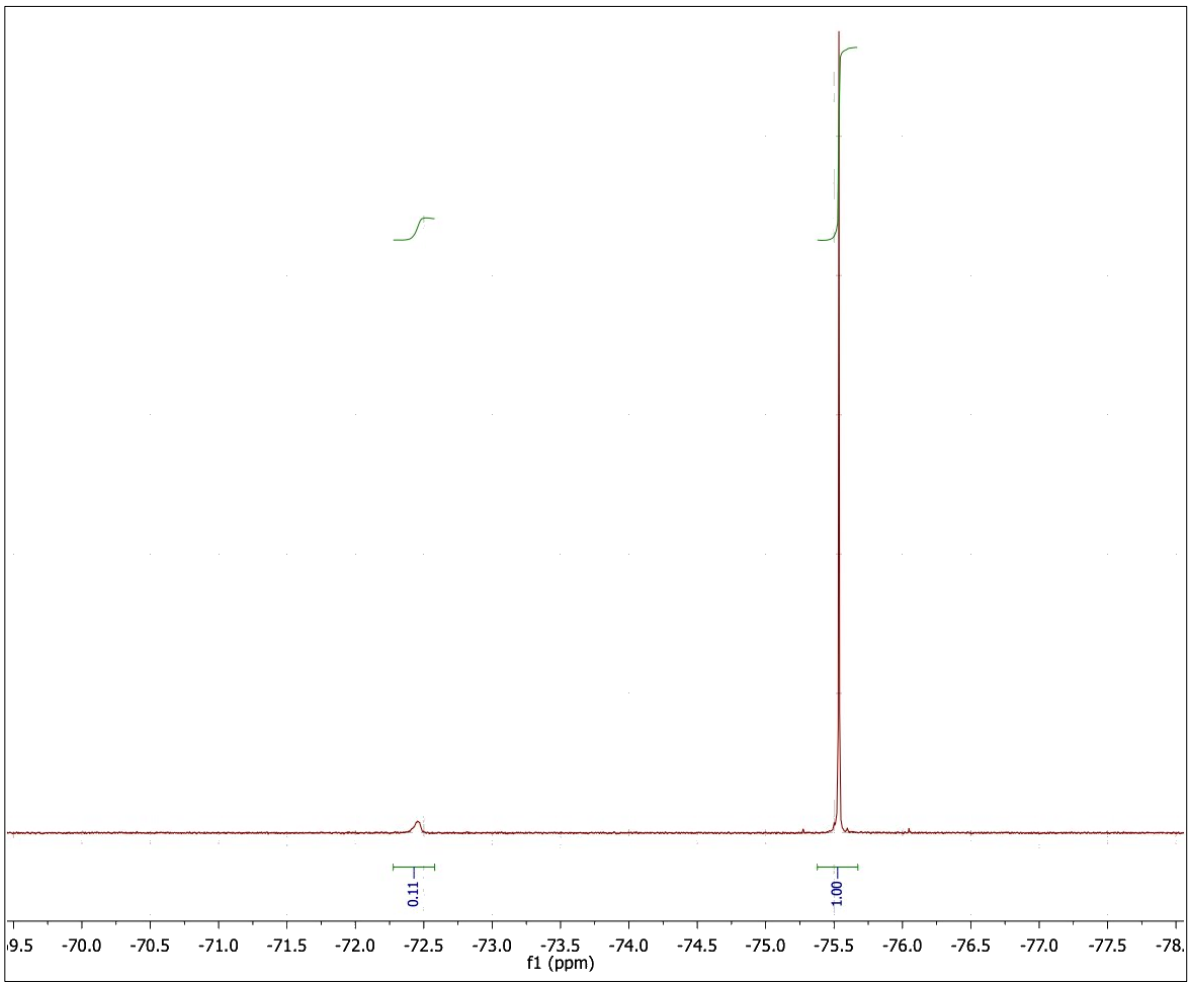

Figure 3.14 Representative 19F NMR spectrum of labelled CAR-T cell lysate. The PERFECTA resonance at −72.4 ppm and the TFA reference peak at −75.5 ppm are visible, with integral values used for quantitative fluorine determination. The single sharp PERFECTA peak and absence of additional signals confirm clean samples free of free nanoparticle contamination.

Quantification of the ^{19}F signal integral, normalized to the TFA external standard, enabled calculation of the total fluorine content per sample. By dividing this value by the number of cells in the analyzed sample (determined by Trypan Blue counting prior to lysis), the average number of ^{19}F atoms internalized per cell was determined for each experiment. ^{19}F NMR analysis was successfully performed on five experiments conducted at standard fluorine concentration (3.13 × 10^19^ ^19^F/mL) where sufficient cell recovery enabled allocation of adequate cell numbers for spectroscopic measurement. Tables 3.W and 3.W-bis present comprehensive uptake and viability data from these experiments, including comparison with control cells.

Experiment	Setup	Cells analysed	^{19}F/cell (×10^{11})	Uptake (%)	Fold Change	Viability (%)	Rhoda+ (%)
1	50 mL	537k	2.83	0.45	32.25	99.96	99.98
2	50 mL	523k	3.21	1.53	17.28	99.93	96.76
3	50 mL	672k	7.93	3.81	24.52	97.15	98.97
4	T25	557k	16.5	3.51	47.1	88.16	99.88
5	T25	953K	9.91	2.11	74.8	89.56	99.71
Mean ± SD			**8.08 ± 5.36**	**2.28 ± 1.38**	**39.2 ± 23.8**	**95.0 ± 5.9**	**99.1 ± 1.3**

Table 3.9 Quantitative ^{19}F uptake analysis for CAR-T cells labelled at standard fluorine concentration (3.13 × 10^19^ ^19^F/mL). Cells analyzed indicates the number of labelled cells used for NMR measurement. % Uptake represents the percentage of administered fluorine that was internalized by cells. Fold Change represents the ratio of rhodamine fluorescence intensity in labelled cells compared to unlabelled control cells. Data from n=5 independent experiments with complete characterization.

Experiment	Setup	Viability (%)	Rhoda+ (%)
1	50 mL	99.91	0.02
2	50 mL	99.67	0
3	50 mL	96.22	0
4	T25	88.6	0
5	T25	58.24*	0
Mean ± SD		**88.5 ± 16.9**	**0.004 ± 0.009**

**Unexpectedly low viability in experiment 5, likely due to batch-specific factors unrelated to handling procedures*

Table 3.10 Viability and rhodamine fluorescence analysis for control CAR-T cells processed identically to labelled cells but incubated with Milli-Q water instead of nanoparticle formulation. The near-zero rhodamine background confirms signal specificity in labelled samples.

The cellular fluorine loading achieved with standard labelling conditions averaged 8.08 ± 5.36 × 10^{11} ^{19}F atoms per cell across the five characterized experiments. The

observed variability, reflected in the relatively high standard deviation, likely stems from differences in CAR-T cell batches, variations in the post-transfection timepoint at which labelling was performed, and inherent biological heterogeneity in cellular uptake capacity. Despite this variability, all experiments achieved fluorine loadings in the range of 2.8–16.5 × 10^{11} ^{19}F/cell, representing substantial cellular labelling suitable for imaging applications.

The cellular fluorine loading achieved in this work represents a significant advancement compared to previously published CAR-T cell labelling studies using ^{19}F-based contrast agents. To place our results in context, Chapelin et al. [23] reported fluorine loadings of 0.5–2.0 × 10^{11} ^{19}F/cell using perfluorocarbon nanoemulsions for T cell labelling in preclinical models, Dubois et al. [48] achieved approximately 1.5 × 10^{11} ^{19}F/cell using similar perfluorinated formulations for immune cell tracking. Our PERFECTA@PLGA-NaC nanoparticle system thus delivers approximately 4-8 fold higher fluorine content per cell compared to these established protocols. This substantial increase in labelling efficiency is particularly relevant for translational applications, as it directly improves the detectability threshold and sensitivity of ^{19}F MRI-based cell tracking.

The high cellular fluorine loading achieved in this study has important implications for the feasibility of ^{19}F MRI-based tracking of labelled CAR-T cells. Higher fluorine content per cell enables detection of lower cell numbers at target sites, as typical ^{19}F MRI detection limits reported in the literature range from approximately 10^4^ to 10^5^ cells per voxel, depending on field strength, coil sensitivity, and acquisition parameters. Our labelling efficiency suggests that detection thresholds at the lower end of this range should be achievable. Additionally, cell division progressively dilutes the cellular fluorine content over time as labelled cells proliferate. Higher initial fluorine loading delays the point at which signal intensity falls below the detection limit, enabling longer-term monitoring of CAR-T cell persistence and proliferation dynamics. Finally, greater fluorine content per cell translates to stronger MRI signals, enhancing spatial resolution and enabling more precise anatomical localization of labelled cell populations within complex tissue microenvironments such as the tumor mass and surrounding brain parenchyma.

This increase in labelling efficiency compared to previously published studies is particularly important as it allows us to predict good detectability in future ^19^F MRI tracking studies, as demonstrated by Chirizzi et al. using similar PLGA-based formulations in preclinical models. The fluorine loadings achieved in the present work meet or exceed the thresholds established in prior literature for successful in vivo cell tracking applications.

To explore whether cellular fluorine loading could be further increased beyond the levels achieved with standard labelling conditions, three additional experiments were performed using an elevated fluorine concentration in the incubation medium. The

nanoparticle dose was increased approximately 3-fold, from the standard 3.13×10^{19} ^{19}F/mL to 9.39×10^{19} ^{19}F/mL, while maintaining the same 6-hour incubation period and Ficoll purification protocol.

Among the three experiments conducted at elevated fluorine concentration, one experiment yielded sufficient cell recovery to enable ^{19}F NMR quantification, providing direct comparison with standard labelling conditions. Two experiments recovered insufficient cells post-Ficoll for NMR analysis but were characterized by flow cytometry for viability and rhodamine uptake. Figure 3.12 presents representative flow cytometry data from one high-concentration labelling experiment, demonstrating maintained viability and efficient nanoparticle uptake at the elevated dose.

Flow cytometry analysis revealed that the percentage of rhodamine-positive cells remained near-complete at high concentration (99.9%), comparable to standard labelling conditions (99.1%). Figure 3.13 illustrates this progressive rightward shift in the fluorescence histogram as nanoparticle concentration increases from unlabelled controls through standard to high-concentration labelling.

Table 3.11 summarizes the comparison between standard and high-concentration labelling protocols.

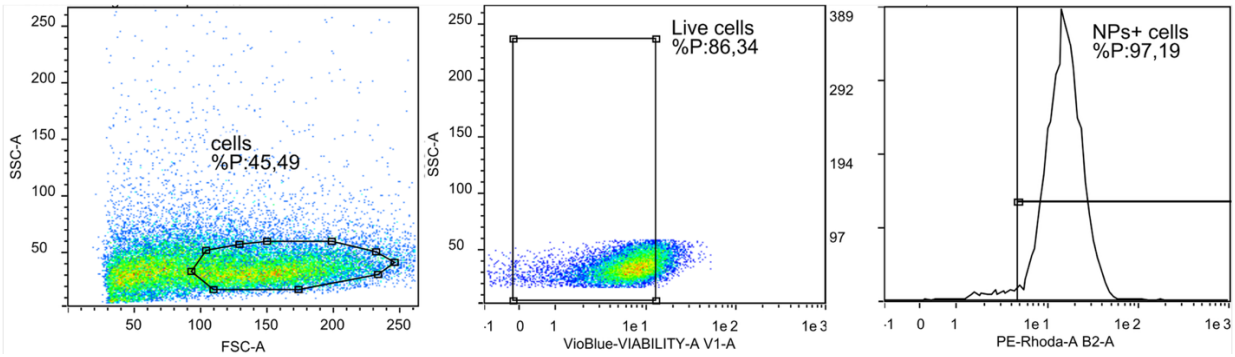

Figure 3.15 Representative flow cytometry analysis of CAR-T cell viability and nanoparticle uptake at high NPs concentration. CAR-T cells labelled with 3-fold higher fluorine concentration show maintained high viability (86.34%) and near-complete nanoparticle uptake (97.19% rhodamine-positive), demonstrating tolerance to elevated nanoparticle doses without significant cytotoxicity.

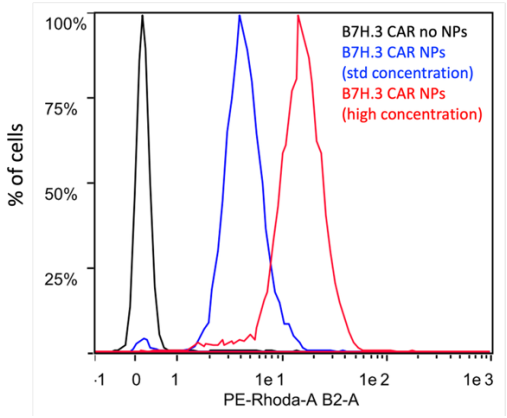

Figure 3.16 Overlay of rhodamine fluorescence histograms showing progressive rightward shift in fluorescence intensity with increasing nanoparticle concentration.

Parameter	**STD** (3.13 × 10^{19} ^{19}F/mL)	**HIGH** (9.39 × 10^{19} ^{19}F/mL)
Experiments with NMR (n)	5	1
^{19}F/cell (× 10^{11})	8.08 ± 5.36	225
Uptake (%)	2.28 ± 1.38	36
Fold Change	39.2 ± 23.8	78.5 ± 26.3*
Viability (%)	95.0 ± 5.9	97.5 ± 3.2*
Rhoda+ (%)	99.1 ± 1.3	99.9 ± 0.02*

**Mean ± SD from 2 experiments with flow cytometry data for HIGH concentration*

Table 3.3.11 Comparison of labelling efficiency and cell viability between standard and elevated fluorine concentrations. The high-concentration condition utilized approximately 3-fold higher nanoparticle dose (9.39 vs 3.13 × 10^{19} ^{19}F/mL) during the 6-hour incubation period.

The single experiment with complete ^{19}F NMR characterization at high concentration demonstrated a dramatic increase in cellular fluorine loading, reaching 2.25 × 10^{13} ^{19}F/cell. This represents an approximately 28-fold increase compared to the average loading achieved with standard concentration, substantially exceeding the 3-fold increase in nanoparticle dose.

Notably, the percentage of administered fluorine that was internalized by cells also increased markedly at high concentration (36% vs 2.3% average for standard

conditions), indicating improved uptake efficiency. The mean fluorescence intensity approximately doubled (78.5 vs 39.2 arbitrary units), consistent with higher nanoparticle loading per cell, while the percentage of rhodamine-positive cells remained near-complete at 99.9%. Crucially, cell viability remained high at the elevated nanoparticle dose (97.5% average across two experiments), demonstrating that CAR-T cells tolerated the increased NP concentration without significant cytotoxic effects during the 6-hour incubation period. This biocompatibility at higher doses suggests that the PERFECTA@PLGA-NaC formulation maintains a favourable safety profile even when cellular loading is substantially increased.

The primary limitation of the high-concentration experiments was insufficient cell recovery following Ficoll purification in two out of three trials, which prevented systematic ^{19}F NMR characterization and statistical comparison with standard conditions. The reasons for reduced recovery in these specific experiments remain unclear but may reflect technical challenges in collecting the cell interface layer from gradients containing higher concentrations of free nanoparticles, or biological factors affecting cell behavior during purification.

The comprehensive characterization of labelled CAR-T cells through flow cytometry and ^{19}F NMR spectroscopy established several key findings: high cell viability (average 95% in experiments with complete characterization) following the labelling and Ficoll purification protocol, confirming biocompatibility of the PERFECTA@PLGA-NaC nanoparticle system; efficient and homogeneous nanoparticle internalization across the cell population, with an average of 88.5% rhodamine-positive cells; near-zero background signal in control cells (0.004% rhodamine-positive), validating signal specificity; substantial cellular fluorine loading averaging $8.08 \pm 5.36 \times 10^{11}$ ^{19}F atoms per cell at standard labelling conditions, representing 4-8 fold higher efficiency compared to previously published T cell labelling protocols; clean samples free of contaminating free nanoparticles, as validated by single sharp ^{19}F NMR peaks; and potential for dramatically increased loading at higher nanoparticle concentrations (achieving 2.25×10^{13} ^{19}F/cell, approximately 28-fold increase) while maintaining high viability, though systematic characterization was limited by cell recovery challenges.

These results validate the biocompatibility and efficiency of the optimized PERFECTA@PLGA-NaC labelling protocol and establish cellular fluorine loadings that predict excellent detectability in ^{19}F MRI-based cell tracking applications. The consistently high fluorine content achieved positions this labelling strategy favourably among current state-of-the-art approaches for therapeutic cell tracking. Having confirmed preservation of cell viability and successful nanoparticle internalization with quantified fluorine loading, it remained essential to verify that the labelling procedure did not compromise the therapeutic functionality of CAR-T cells. This critical aspect was evaluated through functional co-culture experiments with U87 glioblastoma cells, as described in Section 3.2.3.

3.2.3 Coculture assay

Having established that the labelling protocol achieved high cellular fluorine loading while preserving cell viability, the final critical validation step was to assess whether labelled CAR-T cells retained their cytotoxic functionality against cancer cells. The therapeutic efficacy of CAR-T cells depends fundamentally on their ability to recognize, bind to, and eliminate tumor cells expressing the target antigens. Any impairment of this cytotoxic capacity resulting from nanoparticle internalization would render the labelling approach unsuitable for clinical translation, regardless of imaging performance. To evaluate this essential functional parameter, co-culture experiments were performed with U87 glioblastoma neurospheres as target cells.

The experimental procedure followed the protocol described in Section 2.5.2. The co-culture experiments were carried out in 24-well plates, where U87 neurospheres were previously seeded in T cell medium. After the Ficoll purification step, labelled CAR T cells were then added to the wells at a 1:1 effector-to-target ratio with respect to U87 cells, maintaining a total volume of 2 mL per well.

Non-transduced T cells (without the CAR construct) and unlabelled CAR-T cells are used as controls to assess CAR performance, interaction specificity, and the potential effects of NP labelling on cell function.

Cells were co-cultured for a timing ranging from 3 to 5 days under standard incubation conditions (37°C, 5% CO_2), during which morphological changes and interactions between CAR T cells and tumour cells were monitored by optical microscopy. Particular attention was paid to the integrity of neurospheres, the appearance of cellular debris, and the presence of cell clusters, which could indicate cytotoxic activity or altered adhesion properties.

At the end of the co-culture period, all cells were collected for flow cytometry analysis to evaluate the persistence of Rhodamine B fluorescence, the viability of CAR-T cells, and the presence of remaining cancer cells in the co-culture. This step also allowed the evaluation of potential fluorescence signal transfer to proliferating CAR-T cells, as well as a extracellular release of NPs.

Microscopic observations suggested that labelled CAR T cells maintained their morphology and ability to interact with glioblastoma cells throughout the co-culture period.

Flow cytometric analysis of co-culture samples revealed that nanoparticle-labelled CAR-T cells retained cytotoxic functionality comparable to unlabelled controls. Figure 3.14 presents a comprehensive comparison of tumor cell elimination capacity across different conditions. Both unlabelled and labelled CAR-T cells demonstrated effective

cytotoxic activity against U87 glioblastoma cells, with labelled cells achieving tumor cell reduction comparable to the baseline antitumor function observed in unlabelled CAR-T cells.

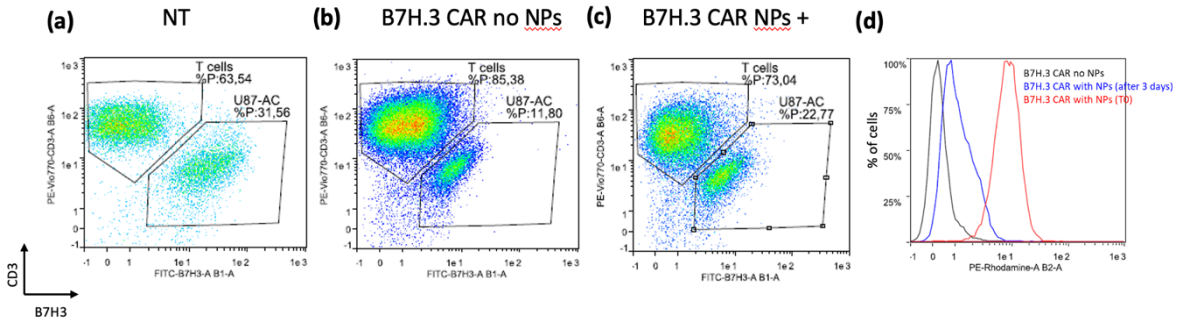

Figure 3.17 Flow cytometry analysis of CAR-T cell cytotoxicity against U87 glioblastoma cells after 3 days of co-culture at 1:1 effector-to-target ratio. (a) Non-transduced T cells co-cultured with U87 cells. (b) B7H3 CAR-T cells without nanoparticles co-cultured with U87 cells, demonstrating effective CAR-mediated tumor cell elimination. (c) Nanoparticle-labelled B7H3 CAR-T cells co-cultured with U87 cells, showing preserved cytotoxic functionality comparable to unlabelled CAR-T cells. (d) Rhodamine fluorescence overlay comparing unlabelled CAR-T cells (black, rhodamine-negative), labelled CAR-T cells at T0 (red, high rhodamine intensity), and labelled CAR-T cells after 3 days of co-culture (blue, reduced intensity).

Quantitative analysis of the cellular composition after 3 days of co-culture confirmed this preserved functionality. As a baseline reference, non-transduced T cells co-cultured with U87 glioblastoma cells (Figure 3.14, panel a) showed 63.54% T cells and 31.56% positive tumor cells, indicating that T cells lacking the CAR construct have minimal cytotoxic activity against the tumor cells and allow substantial tumor cell persistence. In contrast, co-cultures with unlabelled CAR-T cells (panel b) showed a dramatic shift in population composition, with the viable cell population consisting of 85.38% T cells while tumor cells were reduced to only 11.80%. This marked depletion of tumor cells compared to the non-transduced control confirms the potent CAR-mediated cytotoxicity when T cells express the B7-H3-targeting chimeric antigen receptor.

Critically, co-cultures with nanoparticle-labelled CAR-T cells (panel c) demonstrated comparable antitumor efficacy, with T cells comprising 73.04% of the population and tumor cells accounting for 22.77%. While the tumor cell percentage in the labelled CAR-T condition was slightly higher than in the unlabelled CAR-T condition, both showed substantial tumor cell reduction compared to the non-transduced baseline. Starting from an initial 1:1 effector-to-target ratio (theoretically 50% T cells and 50% tumor cells at the beginning of co-culture), both unlabelled and labelled CAR-T conditions showed substantial enrichment of the T cell population and marked depletion of tumor cells, demonstrating that the nanoparticle labelling procedure did not fundamentally compromise the cytotoxic machinery of CAR-T cells.

The comparison across all three conditions (panels a, b, and c) provides clear evidence that labelled CAR-T cells retain the CAR-mediated cytotoxic functionality that distinguishes them from non-engineered T cells. While non-transduced T cells showed minimal impact on tumor cell survival, both unlabelled and labelled CAR-T cells achieved substantial tumor cell elimination, with labelled cells performing comparably to unlabelled controls despite the internalized nanoparticle burden.

Importantly, T cell viability remained high throughout the co-culture period in all conditions, confirming that labelled CAR-T cells not only maintained killing capacity but also survived the cytotoxic interactions without significant cell death. The predominance of T cells in the final CAR-T populations (73-85%) compared to the initial 50% starting proportion indicated net CAR-T cell persistence and potential proliferation in response to antigen engagement, consistent with the expected behavior of functional therapeutic T cells encountering their cognate tumor antigens. This expansion of the T cell population while simultaneously reducing the tumor cell population demonstrates that labelled CAR-T cells retain both their cytotoxic effector functions and their capacity for antigen-driven proliferation.

An interesting observation during the co-culture experiments was the progressive reduction in rhodamine fluorescence intensity in labelled CAR-T cells over the 3-day culture period. Figure 3.14, panel d shows an overlay of rhodamine fluorescence histograms comparing unlabelled CAR-T cells, labelled CAR-T cells at the start of co-culture at T0, and labelled CAR-T cells after 3 days of co-culture. The leftward shift from the initial T0 distribution to the day 3 distribution indicates progressive dilution of the rhodamine signal over the course of the co-culture period. This fluorescence dilution likely reflects CAR-T cell proliferation during co-culture: as labelled cells divide in response to antigen stimulation, the internalized nanoparticles are distributed between daughter cells with each cell division, progressively reducing the fluorescence intensity per cell while the overall population expands. This interpretation is consistent with the observed predominance of T cells in the final co-culture population, which exceeds the initial 50% starting proportion and indicates net CAR-T cell expansion.

While this fluorescence dilution is expected and consistent with cell proliferation—a desirable feature indicating functional CAR-T cell activation and expansion in response to tumor antigen—it raises a theoretical concern about whether nanoparticles might be released from cells over time through mechanisms other than dilution by division. To definitively distinguish between fluorescence dilution due to cell proliferation and potential nanoparticle release or exocytosis, future experiments are planned in which labelled CAR-T cells will be cultured in the absence of tumor cells for equivalent time periods, while also monitoring the proliferation. Such studies will be important for predicting ^{19}F MRI signal decay kinetics in vivo and for interpreting longitudinal imaging data in the context of CAR-T cell proliferation dynamics.

The preservation of cytotoxic functionality in nanoparticle-labelled CAR-T cells represents a critical validation of the labelling approach. These results demonstrate that PERFECTA@PLGA-NaC nanoparticles, despite achieving high intracellular fluorine loading, do not interfere with the complex sequence of events required for CAR-T cell-mediated tumor killing: antigen recognition, immune synapse formation, cytotoxic granule release, and target cell lysis. This functional preservation, combined with the high viability, efficient labelling, and superior fluorine loading documented in Section 3.2.2, establishes the PERFECTA@PLGA-NaC system as a promising platform for ^{19}F MRI-based tracking of therapeutic CAR-T cells without compromising their therapeutic potential.

4. Conclusions and further perspectives

This thesis work focused on the development and characterization of a fluorinated nanoparticle-based labelling system for CAR-T cell tracking using ^{19}F MRI, addressing a critical need in cancer immunotherapy: the ability to non-invasively monitor the biodistribution and persistence of therapeutic cells in patients, particularly in the challenging context of glioblastoma treatment.

The PERFECTA@PLGA-NaC nanoparticle formulation successfully achieved the fundamental requirements for an effective cell labelling platform. Nanoparticles demonstrated excellent physicochemical properties, with hydrodynamic diameters of 150-180 nm, polydispersity indices below 0.2, and stable zeta potentials confirming colloidal stability in culture medium. Fluorine encapsulation efficiency remained consistently high, with approximately 40% of the PERFECTA probe successfully incorporated into the PLGA matrix. Analysis of protein corona formation revealed rapid adsorption of serum proteins upon contact with biological medium, with DLS measurements suggesting ongoing structural reorganization over 24 hours. Interestingly, while DLS detected these temporal changes in nanoparticle size and surface properties, SDS-PAGE analysis showed relatively stable protein composition across timepoints, suggesting that the reorganization may involve conformational changes or exchange of minor protein components rather than wholesale replacement of the major corona constituents. This discrepancy highlights the complexity of protein corona dynamics and indicates that further studies employing advanced proteomic techniques would be valuable for fully characterizing these processes.

Optimization of the CAR-T cell labelling protocol evolved through three phases—24-well plates, 50 mL tubes, and T25 flasks—progressively addressing challenges of cell adhesion, working volumes, and biocompatibility. The final T25 format proved optimal by maintaining cells in their standard culture environment while providing sufficient cell yields for comprehensive characterization. A central challenge was implementing Ficoll density gradient purification to remove free nanoparticles. While this approach successfully achieved complete purification, as confirmed by clean ^{19}F NMR spectra, it introduced substantial cell losses with overall recovery rates of only 2-3%. Despite this limitation, the trade-off between purity and recovery was necessary to ensure accurate downstream measurements and prevent false signals from contaminating free nanoparticles.

Comprehensive characterization of labelled CAR-T cells yielded highly encouraging results. Cell viability remained consistently high (average 95%), while flow cytometry revealed remarkably efficient uptake with 99.1% of cells showing rhodamine fluorescence and minimal variability across experiments. Quantitative ^{19}F NMR established an average cellular fluorine loading of 8.08×10^{11} ^{19}F atoms per cell—

representing a 4-8 fold improvement over previously published CAR-T labelling studies. This substantial fluorine content predicts excellent MRI detectability, enabling detection of smaller cell populations and extended tracking duration. Exploratory high-concentration experiments demonstrated that cellular loading could be increased to 2.25×10^{13} ^{19}F/cell (28-fold enhancement) while maintaining high viability, though systematic characterization was limited by cell recovery challenges.

Functional co-culture experiments provided important evidence that labelled CAR-T cells retain cytotoxic activity against U87 glioblastoma cells. Following 3 days of co-culture at a 1:1 ratio, labelled CAR-T cells achieved substantial tumor cell elimination comparable to unlabelled controls, with the T cell population expanding from an initial 50% to 73% while tumor cells were reduced to 23% of the total viable population. In comparison, unlabelled CAR-T cells achieved slightly more complete tumor cell elimination (85% T cells, 12% tumor cells), while non-transduced T cells lacking the CAR construct showed minimal cytotoxic activity (64% T cells, 23% tumor cells). These results demonstrate that nanoparticle labelling does not fundamentally impair the recognition, binding, and killing mechanisms essential for CAR-T cell therapeutic function. Importantly, the observation that labelled cells maintained high viability throughout co-culture and exhibited population expansion consistent with antigen-driven proliferation indicates that nanoparticle internalization preserves not only cytotoxic capacity but also the T cell activation pathways necessary for therapeutic cell persistence and clonal expansion.

An observation during co-culture experiments was the apparent reduction in rhodamine fluorescence intensity over time, likely reflecting CAR-T cell proliferation in response to antigen stimulation rather than nanoparticle loss. As cells divide, internalized nanoparticles would be distributed between daughter cells, progressively diluting the signal per cell. However, definitively distinguishing between signal dilution from cell division versus potential nanoparticle release requires controlled experiments comparing labelled cells cultured with and without proliferative stimuli, which were beyond the scope of this initial study.

Despite these promising results, important limitations remain. The most significant was the inability to recover sufficient cells for ^{19}F MRI validation. While the achieved fluorine loadings theoretically predict good detectability, experimental confirmation through imaging was prevented by low cell yields. Future work should prioritize improving recovery efficiency through refined Ficoll techniques, alternative purification strategies, or surface-modified nanoparticles that facilitate more efficient separation. Additionally, the observed variability in cellular fluorine uptake ($2.8–16.5 \times 10^{11}$ ^{19}F/cell) suggests opportunities for protocol standardization through tighter control of cell maturation state and nanoparticle properties. The question of long-term nanoparticle retention also requires further investigation through controlled studies comparing labelled cells with and without proliferative stimuli to definitively distinguish signal dilution from nanoparticle release.

Looking forward, the most immediate priority is addressing the cell recovery bottleneck. Systematic optimization of the Ficoll collection technique, exploration of alternative purification methods, or development of modified protocols that reduce technical variability could substantially improve experimental throughput and enable more comprehensive characterization. Once reliable cell recovery is achieved, the next critical step would be actual ^{19}F MRI imaging of labelled cell samples to experimentally validate detectability and quantify signal-to-noise ratios achievable with standard MRI hardware. These phantom imaging studies would be essential before considering any in vivo experiments.

Further investigation of the mechanisms underlying nanoparticle uptake and intracellular trafficking would also be valuable for understanding and potentially improving labelling efficiency. Similarly, longer-term studies examining nanoparticle retention in non-dividing versus proliferating cells would help clarify the fate of internalized nanoparticles and inform interpretation of imaging data. Expanding the functional characterization beyond cytotoxicity assays to include detailed phenotypic analyses and assessment of CAR-T cell persistence in more complex culture systems would strengthen confidence in the biocompatibility of the labelling approach.

In conclusion, this thesis has demonstrated the feasibility of labelling CAR-T cells with PERFECTA@PLGA-NaC nanoparticles to achieve high cellular fluorine loading while maintaining viability and basic cytotoxic functionality in vitro. The results represent an initial proof-of-concept that warrants further development, though substantial additional work remains before this approach could be considered for any translational applications. The most critical next steps involve improving cell recovery to enable systematic characterization and experimental validation of MRI detectability. If these technical challenges can be addressed and the promising initial results are confirmed through more comprehensive studies, fluorine-based MRI tracking could eventually contribute to improving our understanding of CAR-T cell behaviour in preclinical models and potentially, in the longer term, inform optimization of therapeutic strategies in cancer immunotherapy.

List of Figures

List of Tables

Bibliography

[1] H. Sung *et al.*, "Global Cancer Statistics 2020: GLOBOCAN Estimates of Incidence and Mortality Worldwide for 36 Cancers in 185 Countries," *CA. Cancer J. Clin.*, vol. 71, no. 3, pp. 209–249, May 2021, doi: 10.3322/caac.21660.

[2] P. Li, D. Wang, J. Hu, and X. Yang, "The role of imaging in targeted delivery of nanomedicine for cancer therapy," *Adv. Drug Deliv. Rev.*, vol. 189, p. 114447, Oct. 2022, doi: 10.1016/j.addr.2022.114447.

[3] F. Chapelin, C. M. Capitini, and E. T. Ahrens, "Fluorine-19 MRI for detection and quantification of immune cell therapy for cancer," *J. Immunother. Cancer*, vol. 6, no. 1, p. 105, Dec. 2018, doi: 10.1186/s40425-018-0416-9.

[4] D. T. Debela *et al.*, "New approaches and procedures for cancer treatment: Current perspectives," *SAGE Open Med.*, vol. 9, p. 20503121211034366, Jan. 2021, doi: 10.1177/20503121211034366.

[5] L. Gattinoni, D. J. Powell, S. A. Rosenberg, and N. P. Restifo, "Adoptive immunotherapy for cancer: building on success," *Nat. Rev. Immunol.*, vol. 6, no. 5, pp. 383–393, May 2006, doi: 10.1038/nri1842.

[6] L. Zhao and Y. J. Cao, "Engineered T Cell Therapy for Cancer in the Clinic," *Front. Immunol.*, vol. 10, p. 2250, Oct. 2019, doi: 10.3389/fimmu.2019.02250.

[7] M. Sadelain, R. Brentjens, and I. Rivière, "The Basic Principles of Chimeric Antigen Receptor Design," *Cancer Discov.*, vol. 3, no. 4, pp. 388–398, Apr. 2013, doi: 10.1158/2159-8290.CD-12-0548.

[8] S. J. Bagley, A. S. Desai, G. P. Linette, C. H. June, and D. M. O'Rourke, "CAR T-cell therapy for glioblastoma: recent clinical advances and future challenges," *Neuro-Oncol.*, vol. 20, no. 11, pp. 1429–1438, Oct. 2018, doi: 10.1093/neuonc/noy032.

[9] F. Chapelin, "Fluorine-19 Magnetic Resonance Imaging platform to quantify T cell therapy biodistribution, persistence and efficacy," UNIVERSITY OF CALIFORNIA SAN DIEGO, 2019.

[10] N. Elmadany, O. T. Alhalabi, M. Platten, and L. Bunse, "Site-Specific Considerations on Engineered T Cells for Malignant Gliomas," *Biomedicines*, vol. 10, no. 7, p. 1738, Jul. 2022, doi: 10.3390/biomedicines10071738.

[11] E. T. Ahrens and J. W. M. Bulte, "Tracking immune cells in vivo using magnetic resonance imaging," *Nat. Rev. Immunol.*, vol. 13, no. 10, pp. 755–763, Oct. 2013, doi: 10.1038/nri3531.

[12] I. Tirotta *et al.*, "^{19} F Magnetic Resonance Imaging (MRI): From Design of Materials to Clinical Applications," *Chem. Rev.*, vol. 115, no. 2, pp. 1106–1129, Jan. 2015, doi: 10.1021/cr500286d.

[13] E. Garbayo, S. Pascual-Gil, C. Rodríguez-Nogales, L. Saludas, A. Estella-Hermoso De Mendoza, and M. J. Blanco-Prieto, "Nanomedicine and drug delivery systems in cancer and regenerative medicine," *WIREs Nanomedicine Nanobiotechnology*, vol. 12, no. 5, p. e1637, Sep. 2020, doi: 10.1002/wnan.1637.

[14] M.-Y. Kim *et al.*, "Tumor Self-Seeding by Circulating Cancer Cells," *Cell*, vol. 139, no. 7, pp. 1315–1326, Dec. 2009, doi: 10.1016/j.cell.2009.11.025.

[15] T. L. Moore *et al.*, "Nanoparticle colloidal stability in cell culture media and impact on cellular interactions," *Chem. Soc. Rev.*, vol. 44, no. 17, pp. 6287–6305, 2015, doi: 10.1039/C4CS00487F.

[16] G. Pinto *et al.*, "Molecular fingerprint by omics-based approaches in saliva from patients affected by SARS-CoV-2 infection," *J. Mass Spectrom.*, vol. 59, no. 9, p. e5082, Sep. 2024, doi: 10.1002/jms.5082.

[17] J. Wu, X. Wang, Y. Wang, Z. Xun, and S. Li, "Application of PLGA in Tumor Immunotherapy," *Polymers*, vol. 16, no. 9, p. 1253, Apr. 2024, doi: 10.3390/polym16091253.

[18] H. Chen, W. Zhang, G. Zhu, J. Xie, and X. Chen, "Rethinking cancer nanotheranostics," *Nat. Rev. Mater.*, vol. 2, no. 7, p. 17024, May 2017, doi: 10.1038/natrevmats.2017.24.

[19] J. Wang and H. Cui, "Nanostructure-Based Theranostic Systems," *Theranostics*, vol. 6, no. 9, pp. 1274–1276, 2016, doi: 10.7150/thno.16479.

[20] J. Xie, S. Lee, and X. Chen, "Nanoparticle-based theranostic agents," *Adv. Drug Deliv. Rev.*, vol. 62, no. 11, pp. 1064–1079, Aug. 2010, doi: 10.1016/j.addr.2010.07.009.

[21] J. Wang and H. Cui, "Nanostructure-Based Theranostic Systems," *Theranostics*, vol. 6, no. 9, pp. 1274–1276, 2016, doi: 10.7150/thno.16479.

[22] M. Srinivas, A. Heerschap, E. T. Ahrens, C. G. Figdor, and I. J. M. D. Vries, "19F MRI for quantitative in vivo cell tracking," *Trends Biotechnol.*, vol. 28, no. 7, pp. 363–370, Jul. 2010, doi: 10.1016/j.tibtech.2010.04.002.

[23] F. Chapelin, S. Gao, H. Okada, T. G. Weber, K. Messer, and E. T. Ahrens, "Fluorine-19 nuclear magnetic resonance of chimeric antigen receptor T cell biodistribution in murine cancer model," *Sci. Rep.*, vol. 7, no. 1, p. 17748, Dec. 2017, doi: 10.1038/s41598-017-17669-4.

[24] D. R. Johnson and B. P. O'Neill, "Glioblastoma survival in the United States before and during the temozolomide era," *J. Neurooncol.*, vol. 107, no. 2, pp. 359–364, Apr. 2012, doi: 10.1007/s11060-011-0749-4.

[25] O. Netufo *et al.*, "Refining Glioblastoma Surgery through the Use of Intra-Operative Fluorescence Imaging Agents," *Pharmaceuticals*, vol. 15, no. 5, p. 550, Apr. 2022, doi: 10.3390/ph15050550.

[26] R. Stupp, M. E. Hegi, and W. P. Mason, "Effects of radiotherapy with concomitant and adjuvant temozolomide versus radiotherapy alone on survival in glioblastoma in a randomised phase III study: 5-year analysis of the EORTC-NCIC trial".

[27] T. A. Dolecek, J. M. Propp, N. E. Stroup, and C. Kruchko, "CBTRUS Statistical Report: Primary Brain and Central Nervous System Tumors Diagnosed in the United States in 2005-2009," *Neuro-Oncol.*, vol. 14, no. suppl 5, pp. v1–v49, Nov. 2012, doi: 10.1093/neuonc/nos218.

[28] S.-M. Razavi, K. E. Lee, B. E. Jin, P. S. Aujla, S. Gholamin, and G. Li, "Immune Evasion Strategies of Glioblastoma," *Front. Surg.*, vol. 3, Mar. 2016, doi: 10.3389/fsurg.2016.00011.

[29] S. Ostrand-Rosenberg, "Immune surveillance: a balance between protumor and antitumor immunity," *Curr. Opin. Genet. Dev.*, vol. 18, no. 1, pp. 11–18, Feb. 2008, doi: 10.1016/j.gde.2007.12.007.

[30] Y. Liu and G. Zeng, "Cancer and Innate Immune System Interactions: Translational Potentials for Cancer Immunotherapy," *J. Immunother.*, vol. 35, no. 4, pp. 299–308, May 2012, doi: 10.1097/CJI.0b013e3182518e83.

[31] S. Kiesgen, L. Chicaybam, N. K. Chintala, and P. S. Adusumilli, "Chimeric Antigen Receptor (CAR) T-Cell Therapy for Thoracic Malignancies," *J. Thorac. Oncol.*, vol. 13, no. 1, pp. 16–26, Jan. 2018, doi: 10.1016/j.jtho.2017.10.001.

[32] D. Mittal, M. M. Gubin, R. D. Schreiber, and M. J. Smyth, "New insights into cancer immunoediting and its three component phases — elimination, equilibrium and escape," *Curr. Opin. Immunol.*, vol. 27, pp. 16–25, Apr. 2014, doi: 10.1016/j.coi.2014.01.004.

[33] E. J. Lipson *et al.*, "Durable Cancer Regression Off-Treatment and Effective Reinduction Therapy with an Anti-PD-1 Antibody," *Clin. Cancer Res.*, vol. 19, no. 2, pp. 462–468, Jan. 2013, doi: 10.1158/1078-0432.CCR-12-2625.

[34] S. A. Rosenberg, N. P. Restifo, J. C. Yang, R. A. Morgan, and M. E. Dudley, "Adoptive cell transfer: a clinical path to effective cancer immunotherapy," *Nat. Rev. Cancer*, vol. 8, no. 4, pp. 299–308, Apr. 2008, doi: 10.1038/nrc2355.

[35] P. J. Spiess, J. C. Yang, and S. A. Rosenberg, "In Vivo Antitumor Activity of Tumor-Infiltrating Lymphocytes Expanded in Recombinant Interleukin-2," *JNCI J.*

Natl. Cancer Inst., vol. 79, no. 5, pp. 1067–1075, Nov. 1987, doi: 10.1093/jnci/79.5.1067.

[36] K. K. Tsai and K. V. Komanduri, "Tumor-Infiltrating Lymphocyte Therapy for the Treatment of Metastatic Melanoma," *Am. J. Clin. Dermatol.*, vol. 26, no. 5, pp. 733–745, Sep. 2025, doi: 10.1007/s40257-025-00957-5.

[37] M. Maffezzini *et al.*, "Polyclonal expansion of functional tumor-reactive lymphocytes infiltrating glioblastoma for personalized cell therapy," *Nat. Commun.*, vol. 16, no. 1, p. 7279, Aug. 2025, doi: 10.1038/s41467-025-62263-2.

[38] C. J. Turtle *et al.*, "CD19 CAR–T cells of defined CD4+:CD8+ composition in adult B cell ALL patients," *J. Clin. Invest.*, vol. 126, no. 6, pp. 2123–2138, Apr. 2016, doi: 10.1172/JCI85309.

[39] D. M. Barrett, S. A. Grupp, and C. H. June, "Chimeric Antigen Receptor– and TCR-Modified T Cells Enter Main Street and Wall Street," *J. Immunol.*, vol. 195, no. 3, pp. 755–761, Aug. 2015, doi: 10.4049/jimmunol.1500751.

[40] K. M. Cappell and J. N. Kochenderfer, "Long-term outcomes following CAR T cell therapy: what we know so far," *Nat. Rev. Clin. Oncol.*, vol. 20, no. 6, pp. 359–371, Jun. 2023, doi: 10.1038/s41571-023-00754-1.

[41] T. A. Bui, H. Mei, R. Sang, D. G. Ortega, and W. Deng, "Advancements and challenges in developing in vivo CAR T cell therapies for cancer treatment," *eBioMedicine*, vol. 106, p. 105266, Aug. 2024, doi: 10.1016/j.ebiom.2024.105266.

[42] E. Picarda, K. C. Ohaegbulam, and X. Zang, "Molecular Pathways: Targeting B7-H3 (CD276) for Human Cancer Immunotherapy," *Clin. Cancer Res.*, vol. 22, no. 14, pp. 3425–3431, Jul. 2016, doi: 10.1158/1078-0432.CCR-15-2428.

[43] D. Nehama *et al.*, "B7-H3-redirected chimeric antigen receptor T cells target glioblastoma and neurospheres," *EBioMedicine*, vol. 47, pp. 33–43, Sep. 2019, doi: 10.1016/j.ebiom.2019.08.030.

[44] M. Digregorio, N. Coppieters, A. Lombard, P. N. Lumapat, F. Scholtes, and B. Rogister, "The expression of B7-H3 isoforms in newly diagnosed glioblastoma and recurrence and their functional role," *Acta Neuropathol. Commun.*, vol. 9, no. 1, p. 59, Dec. 2021, doi: 10.1186/s40478-021-01167-w.

[45] F. Juković-Bihorac *et al.*, "B7-H3 as a Reliable Diagnostic Biomarker for the Differentiation of High-Grade Gliomas (HGGs) and Low-Grade Gliomas (LGGs)," *Brain Sci.*, vol. 15, no. 8, p. 872, Aug. 2025, doi: 10.3390/brainsci15080872.

[46] J. Hunger *et al.*, "*In vivo* nanoparticle-based T cell imaging can predict therapy response towards adoptive T cell therapy in experimental glioma," *Theranostics*, vol. 13, no. 15, pp. 5170–5182, 2023, doi: 10.7150/thno.87248.

[47] F. Galli, M. Varani, C. Lauri, G. G. Silveri, L. Onofrio, and A. Signore, "Immune cell labelling and tracking: implications for adoptive cell transfer therapies," *EJNMMI Radiopharm. Chem.*, vol. 6, no. 1, p. 7, Feb. 2021, doi: 10.1186/s41181-020-00116-7.

[48] V. P. Dubois, O. C. Sehl, P. J. Foster, and J. A. Ronald, "Visualizing CAR-T cell Immunotherapy Using 3 Tesla Fluorine-19 MRI," *Mol. Imaging Biol.*, vol. 24, no. 2, pp. 298–308, Apr. 2022, doi: 10.1007/s11307-021-01672-3.

[49] G. N. Holland, P. A. Bottomley, and W. S. Hinshaw, "19F magnetic resonance imaging," *J. Magn. Reson. 1969*, vol. 28, no. 1, pp. 133–136, Oct. 1977, doi: 10.1016/0022-2364(77)90263-3.

[50] E. T. Ahrens and J. Zhong, "*In vivo* MRI cell tracking using perfluorocarbon probes and fluorine-19 detection," *NMR Biomed.*, vol. 26, no. 7, pp. 860–871, Jul. 2013, doi: 10.1002/nbm.2948.

[51] C. Fink *et al.*, "19F-perfluorocarbon-labeled human peripheral blood mononuclear cells can be detected in vivo using clinical MRI parameters in a therapeutic cell setting," *Sci. Rep.*, vol. 8, no. 1, p. 590, Jan. 2018, doi: 10.1038/s41598-017-19031-0.

[52] B. L. Bona, O. Koshkina, C. Chirizzi, V. Dichiarante, P. Metrangolo, and F. Baldelli Bombelli, "Multibranched-Based Fluorinated Materials: Tailor-Made Design of^{19} F-MRI Probes," *Acc. Mater. Res.*, vol. 4, no. 1, pp. 71–85, Jan. 2023, doi: 10.1021/accountsmr.2c00203.

[53] I. Tirotta *et al.*, "A Superfluorinated Molecular Probe for Highly Sensitive *in Vivo*^{19} F-MRI," *J. Am. Chem. Soc.*, vol. 136, no. 24, pp. 8524–8527, Jun. 2014, doi: 10.1021/ja503270n.

[54] C. Chirizzi *et al.*, "A Bioorthogonal Probe for Multiscale Imaging by^{19} F-MRI and Raman Microscopy: From Whole Body to Single Cells," *J. Am. Chem. Soc.*, vol. 143, no. 31, pp. 12253–12260, Aug. 2021, doi: 10.1021/jacs.1c05250.

[55] C. Chirizzi *et al.*, "Optimization of superfluorinated PLGA nanoparticles for enhanced cell labelling and detection by 19F-MRI," *Colloids Surf. B Biointerfaces*, vol. 220, p. 112932, 2022, doi: https://doi.org/10.1016/j.colsurfb.2022.112932.

[56] M. P. Monopoli, C. Åberg, A. Salvati, and K. A. Dawson, "Biomolecular coronas provide the biological identity of nanosized materials," *Nat. Nanotechnol.*, vol. 7, no. 12, pp. 779–786, Dec. 2012, doi: 10.1038/nnano.2012.207.

[57] L. Gatti *et al.*, "Pivotal role of the protein corona in the cell uptake of fluorinated nanoparticles with increased sensitivity for^{19} F-MR imaging," *Nanoscale Adv.*, vol. 5, no. 14, pp. 3749–3760, 2023, doi: 10.1039/D3NA00229B.

[58] J. Stetefeld, S. A. McKenna, and T. R. Patel, “Dynamic light scattering: a practical guide and applications in biomedical sciences,” *Biophys. Rev.*, vol. 8, no. 4, pp. 409–427, Dec. 2016, doi: 10.1007/s12551-016-0218-6.

[59] D. Docter *et al.*, “Quantitative profiling of the protein coronas that form around nanoparticles,” *Nat. Protoc.*, vol. 9, no. 9, pp. 2030–2044, Sep. 2014, doi: 10.1038/nprot.2014.139.

[60] P. R. Errante, “Flow cytometry: a literature review,” 2016, *Unpublished*. doi: 10.13140/RG.2.1.2461.0969.

[61] O. D. Laerum and T. Farsund, “Clinical application of flow cytometry: A review,” *Cytometry*, vol. 2, no. 1, pp. 1–13, Jul. 1981, doi: 10.1002/cyto.990020102.

Acknowledgements

Questo lavoro rappresenta molto più di un progetto di tesi: è il risultato di un percorso lungo, intenso, fatto di crescita, cambiamenti e tante versioni di me.

Ringrazio prima di tutto i miei genitori, che mi hanno permesso di arrivare fin qui e che in tutti questi anni non hanno mai smesso di sostenermi. Con il loro supporto, i loro sacrifici e la loro fiducia mi hanno dato la possibilità di costruire questo percorso.

Ringrazio la Prof.ssa Baldelli e la Prof.ssa Pellegatta per avermi dato questa grande opportunità e per aver creduto in me. Ricordo ancora quando ho ricevuto la mail di conferma della Prof.ssa Baldelli: ero a lezione in Spagna e l'ho letta con gli occhi lucidi. Da quel momento ho creduto tantissimo in questo progetto e in questa ricerca, che hanno rappresentato per me un percorso stimolante e formativo.

Un grazie speciale a Beatrice, Cristina e Manuela: con pazienza e generosità mi avete insegnato tantissimo, accompagnandomi in un mondo completamente nuovo per me.

Ringrazio i ragazzi del Besta, che mi hanno aiutata quando avevo paura di sbagliare. Mi avete fatta sentire accolta e capace anche nei momenti di maggiore insicurezza.

Ringrazio anche i ragazzi del laboratorio e soprattutto Paolo, che mi ha sempre ascoltata e aiutata con disponibilità e attenzione.

Ringrazio i miei compagni di università, Fabio e Riccardo, che mi hanno accolta come una sorella e mi hanno tirata su quando nessuno ci riusciva. In questi anni siete diventati per me molto più di semplici compagni di corso.

Un grazie grande alle mie amiche, a chi c'è da sempre e a chi è arrivata più recentemente: Benedetta, Greta, Sara, Roberta, Cecilia, Caterina, Chiara e Teresa. Ognuna di voi ha reso questo percorso più leggero e più bello.

Ringrazio i miei colleghi-Livia, Roby, Riki, Gio, la Raffy e Samy-per la quotidianità condivisa durante questi ultimi mesi, per le risate e per il sostegno che mi avete regalato.

Ringrazio i miei amici di NoLo e questo quartiere che mi ha accolta e vista crescere insieme a lui. È stato casa, cambiamento e scoperta.

Grazie ai miei compagni di Erasmus, esperienza che porterò sempre con me, e un grazie speciale a Laura.

Ringrazio i miei zii e i miei cugini, che hanno sempre fatto il tifo per me con affetto e presenza costante.

Ringrazio il Politecnico di Milano, che mi ha insegnato a non mollare mai e a cercare sempre di migliorarmi, e la Universitat Politècnica de València, che mi ha regalato un'esperienza di crescita e scoperta che porterò sempre con me.

Grazie per essere stati parte di questo viaggio.